INVESTIGATION OF HALL EFFECT THRUSTER CHANNEL WALL EROSION MECHANISMS

A Dissertation
Presented to
The Academic Faculty

by

Aaron M. Schinder

In Partial Fulfillment
of the Requirements for the Degree
Doctor of Philosophy in the
Daniel Guggenheim School of Aerospace Engineering

Georgia Institute of Technology
December 2016

INVESTIGATION OF HALL EFFECT THRUSTER CHANNEL WALL EROSION MECHANISMS

Approved by:

Dr. Mitchell L. R. Walker, Advisor
School of Aerospace Engineering
Georgia Institute of Technology

Dr. Julian J. Rimoli, Advisor
School of Aerospace Engineering
Georgia Institute of Technology

Dr. John Yim
NASA Glenn Research Center

Dr. Sven Simon
School of Earth and Atmospheric Sciences
Georgia Institute of Technology

Dr. W. Jud Ready
Electro-Optical Systems Laboratory
Georgia Tech Research Institute

Date Approved: August 2nd, 2016

ACKNOWLEDGEMENTS

I wish to thank my advisors: Prof Mitchell Walker for introducing me to electric propulsion research and building an impressive lab with fascinating work to be involved in. I wish to thank Prof Julian Rimoli for helping with computational modeling, and for providing mentorship, humor, and amazing barbecue parties.

I would also like to thank my thesis committee, Dr. Yim, Prof Simon, and Dr. Ready for taking the time to read my thesis and listen to my proposal and defense. I would like to thank the American Society of Engineering Education, and the Air Force Office of Scientific Research for funding my research. I would like to thank Dr. Brent Wagner of GTRI for help using the GTRI Ion Assisted Deposition chamber in ways its designers never intended, at maximum power, for tens of hours at a time. Thank you for fixing the issues that arose, and coming in to help late at night.

I would like to thank Thomas Burton of the University of Alabama for help sectioning and performing SEM microscopy and XPS of the M26 samples, and for showing me around Tuscaloosa. I enjoyed working with you on the broader AFOSR project.

I would like to thank the graduate students at HPEPL and CSML for their help, support, and friendship. I would like to thank Sam Langendorf for mentoring me on the finer points of plasma physics, and for your friendship and awesome discussions about philosophy, life, and science. I would like to thank Jonathan Walker for your friendship, and for allowing me to participate in your testing and brainstorm about the interesting problems that arose. Thank you for organizing awesome 4th of July fireworks displays. Also thanks for being the 'mad scientist' of the lab, unafraid to build really interesting

projects. "Don't worry, this only looks dangerous" is one of my favorite quotes. Natalie, for an interesting new perspective on the lab that helps channel the insanity: I want to see that sitcom someday. Jason, for your encyclopedic knowledge of where everything is, what everything does, how everything works (or in some cases, doesn't). Amir, for your interest in challenging mathematics and your interesting discussions on your and my research.

Finally, I would like to thank my parents and family for being there for me and listening to me worry before quals, before the proposal, and before the defense. I'm also glad that I could celebrate with you afterwards. I would like to thank my brother for the well-timed distraction of the cyber-warfare conference. I would like to thank my sister for helping proofread my dissertation, and for visiting.

TABLE OF CONTENTS

LIST OF TABLES

LIST OF FIGURES

LIST OF SYMBOLS

a	Lattice constant (Å)
α	Ion impact angle (deg)
α	Coefficient of thermal expansion (m/m-K)
α	Average volumetric energy cost of sputtering (J/m^3)
a_h	Wave height amplitude (μm)
$A(\boldsymbol{\sigma}, \boldsymbol{n})$	Stress function (MPa)
B_r, B_{rmax}	Radial and maximum radial magnetic field (T)
B_i	Angle fitting coefficients (deg^{-i})
E	Ion impact energy (eV)
E	Young's modulus, modulus of elasticity (GPa)
E_{th}	Sputtering threshold energy (eV)
E_{bond}	Bond energy (eV/bond)
E_{SBE}	Surface binding energy (J)
e	Electron charge (1.609×10^{-19} C)
ε	Ion energy due to the Bohm velocity (mA)
ε_{ij}	Strain component (m/m)
f_{vi}	Velocity distribution function (1/(m/s)^3)
δf_j	Unbalanced variational surface force (N)
g_x, g_y	Components of local surface normal
γ	Free surface energy (J/m^2)
Γ_e, Γ_i	Flux of electrons and ions to channel wall (#/m^2-s)

H	Average erosion depth (μm)
$h(x)$	Variation to average surface height (μm)
$\hat{h}(\omega)$	Fourier transformed variation to surface (μm/wave mode)
I_{iw}	Ion current to channel wall (mA/cm^2)
$k(T)$	Spring constant as a function of temperature (N/mm)
k_0	Spring constant at room temperature (N/mm)
k_b	Boltzmann's constant (1.3806×10^{-23} J/K)
kT_e/e	Electron temperature (eV)
K_g	Nondimensional function of problem geometry
λ	Lame constant (an elastic modulus) (GPa)
M	Kinetic constant of instability (m^4/J-s or (m/s) / (J/m^3))
m_i, m_e	Ion and electron mass (kg)
μ	Shear modulus (GPa)
n_N	Number density of nitrogen (#/m^3)
$\hat{n}$	Local surface normal unit vector.
υ	Poisson's ratio (nondimensional)
ω_{cr}	Critical wavenumber (rad/m)
ω_{mg}	Wavenumber of maximum growth rate (rad/m)
P_w	Power flux to the wall (W/cm^2)
ϕ	Plasma sheath potential (V)
$\Psi(\omega)$	Amplification function (nondimensional)
σ_h	Hoop stress (MPa)

σ_r	Radial stress (MPa)
σ_i	A stress tensor component, in general (MPa)
σ_b	Standard deviation of the slope of a linear regression.
t_n , t_s	Normal and shear component of variation to stress (MPa)
T	Temperature (K)
T_r	Temperature gradient in radial direction (K/m)
T_e	Electron temperature (K)
ΔT	Change in temperature from room temperature (K, °C)
τ	Time constant of growth (1/s)
u, v	Extension, displacement, spring extension (m)
w_0	Average strain energy density (J/m^3)
Δw	Variation to strain energy density (J/m^3)
Y	Atomic sputtering yield (atoms/ion or mm^3/Coulomb)
$\Delta z(\Delta x)$	Autocorrelation function (m).

LIST OF ABBREVIATIONS

AFRL	Air Force Research Laboratory
BN	Boron Nitride
BPT	Busek Primex Thruster
CMM	Coordinate Measuring Machine
DAQ	Data Acquisition System
GTRI	Georgia Tech Research Institute
HET	Hall Effect Thruster

NASA	National Aeronautics and Space Administration
SEM	Scanning Electron Microscopy
SRH	Strain Relief Hypothesis
UM	University of Michigan
XPS	X-ray Photoelectron Spectroscopy

SUMMARY

The primary life-limiting mechanism for Hall effect thrusters (HETs) is the plasma erosion of the discharge channel wall. Over the course of tens of thousands of hours, energetic ions sputter material from the annular discharge channel wall of the HET, wearing away the material in the 1-2 cm near the exit plane of the thruster. If the channel wall is completely worn away in these areas, the magnetic circuit is exposed, and continued operation of the thruster will lead to the ejection of ferrous material into the spacecraft environment and eventual failure of the magnetic circuit. Qualifying HETs for a minimum 1.5 times desired mission life is an expensive process requiring tens of thousands of hours of chamber time. Computational modeling of thruster lifetime can make predictions about the average erosion depth, but present models cannot explain certain features that appear during testing. One such feature is the anomalous erosion ridge phenomenon in HETs. In order to improve HET life modeling, a better understanding of the formation of features during plasma erosion is needed.

In this work, an investigation into the details of the plasma erosion of materials is conducted. The way in which the material microstructure and the mechanical stress in materials modify the process of plasma erosion is studied, with experiments and computational modeling. A 3D raytracing model of the development of surfaces in a complex heterogeneous material is created. The model reproduces the development of surface features observed in SEM microscopy of the eroded AFRL/UM P5 channel wall. SEM imaging of borosil reveals a complex heterogeneous microstructure composed of boron nitride grains in a silica matrix. The role of the microstructure in the development

of observed erosion features is explored. The strain relief hypothesis, which proposes that the presence of mechanical stress in materials will lead to the existence of unstable surface modes under erosion, is investigated. The SRH predicts that surface features with wavelengths dependent on applied mechanical stress will grow during erosion.

An experiment to test the dependence of the plasma erosion process on the presence of mechanical stress in materials is designed and conducted. Two materials, amorphous fused silica and M26 borosil, are placed under varying amounts of mechanical stress up to 25 MPa and exposed to argon plasma for 12 hours. Microscopy and detailed surface statistics are collected before and after each exposure. During each exposure, a pair of samples: one under a compressive mechanical load, and the other unloaded, are exposed.

The results of these experiments reveal that different mechanisms for each material lead to the development of complex surface patterns. For fused silica, a complex cell pattern is generated from initial roughness present in the surface. The development of this cell pattern can be explained as being the result of the angle-dependence of the sputtering yield of silica. For M26 borosil, it is found that the difference in the sputtering yield between the boron nitride and silica components of the material is the dominant mechanism leading to the development of surface features. For both M26 and fused silica samples, for applied loads of up to 25 MPa, no dependence of the development of the surface features on the mechanical stress has been detected.

This work has found that the ion impact angles, the initial surface structure in the case of fused silica, and the heterogeneous nature of borosil composites all play a role in the generation of microstructural surface features during plasma erosion. However, no

evidence has been found for the sensitivity of the plasma erosion of M26 and fused silica to mechanical stresses of up to 25 MPa.

CHAPTER 1

INTRODUCTION

1.1. Electric Propulsion Overview

Most spacecraft maneuver in space by expelling propellant. There are limited exceptions to this, such as magnetic tethers and solar sails, but most spacecraft maneuver by use of the rocket principle. Tsiolkovsky's rocket Equation (1-1) relates the fraction of the mass of a spacecraft that must be expended as propellant to accomplish a given mission. It relates properties of the propulsion system of the spacecraft, propellant mass fraction, and the total maneuver delta-V requirements of a mission. In the equation below, m_f is the mass of the rocket after a maneuver, m_0 is the initial mass of the rocket, and Δv or delta-V is the change in velocity performed during the maneuver. For historical reasons, the speed of the propellant jet is usually given in terms of internal specific impulse (I_{sp}), with units of seconds times gravitational acceleration at Earth's surface g_0. The I_{sp}, and therefore the relationship between the total mission Δv and the propellant needed, is determined by the type of propulsion system.

$$\frac{m_f}{m_0} = \exp\left(\frac{-\Delta v}{Isp * g_0}\right) \tag{1-1}$$

A propulsion system must have high thrust to launch from a planet into orbit, where it must overcome gravity to ascend. The amount of time spent accelerating against a gravity field contributes to a Δv measure called the gravity loss. For inter-orbit transfers and station-keeping, a high I_{sp} is a more important propulsion system characteristic than

thrust. For a maneuver of a given Δv, I_{sp} exponentially reduces the amount of propellant a spacecraft must carry to accomplish it. It would be ideal to have both high thrust and high I_{sp}, however, it is not usually possible to have both. For a fixed power available to a thruster, there is an inverse relationship between I_{sp} and thrust.

Modern propulsion systems can be broken into several major categories. Of these, chemical thrusters are thrusters that obtain their energy from burning a propellant in a chemical reaction. Electric propulsion (EP) thrusters accelerate the propellant using externally supplied electric power. Chemical thrusters tend to have high thrust and low Isp (between 200 and 400 s). The chemical reaction determines the specific energy supplied to the exhaust gasses, and so the I_{sp} is determined by the propellant choice. EP thrusters have much lower thrust and higher I_{sp} (1000-4000 s). The EP device category can be further broken down by the method these thrusters use to accelerate the propellant: Electro-thermal systems, such as arcjets, heat a propellant and thermally expand the working gas. Electromagnetic thrusters use a current arc crossed with a magnetic field to produce a Lorenz force to accelerate plasma. Electrostatic thrusters ionize the working gas and accelerate the ions using electric fields [1].

Hall effect thrusters (HETs) are a promising electrostatic space propulsion technology for applications such as station-keeping and primary propulsion. HETs typically operate at specific impulses of 1300 - 3000 s at efficiencies of 50% or more [2]. Two main types of HETs have been developed: Stationary Plasma Thrusters (SPT) and Thruster with Anode Layer (TAL). TALs use a conducting channel wall as their anode, have very short acceleration regions, and high electron temperatures. SPTs have seen the most development and use. They use a dielectric channel wall, have longer ionization and

acceleration regions, and lower electron temperatures. This work is primarily concerned with HETs of the SPT type.

In a HET, neutral gas is injected by an anode gas distributor at the upstream end of the discharge channel. A cathode, which can be center-mounted or positioned external to the thruster, emits electrons. Some of the electrons neutralize the ion beam. Some of the electrons travel into the discharge channel where they are trapped by a crossed electric and magnetic field that induce a Hall current. The trapped electrons ionize the neutral gas, and eventually end up at the anode, completing the circuit. The ions are rapidly accelerated out of the discharge channel by an electric field, producing thrust. Figure 1.1 illustrates these simultaneous physical processes.

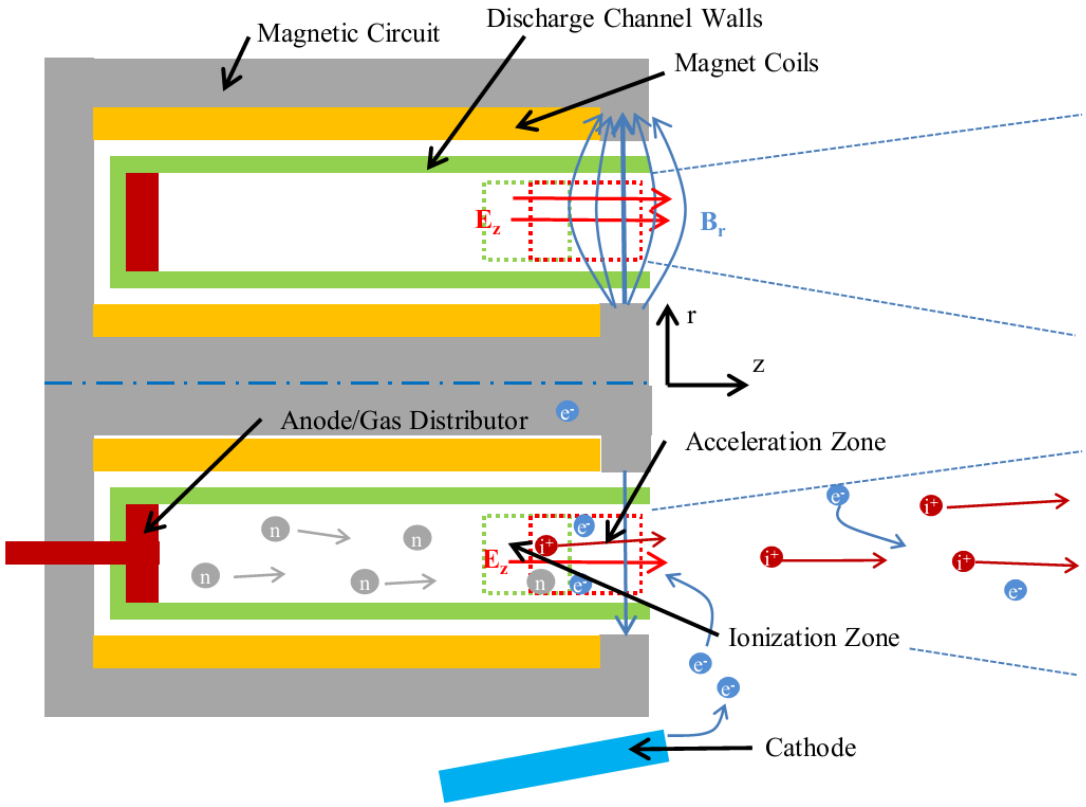

Figure 1.1: Diagram of a Hall effect thruster.

1.2. HET Erosion Background

Hall effect thrusters have limited useful lives, which constrain the total impulse an engine can produce. It is a design requirement that the life of an EP thruster is long enough to produce 1.5 times the total design impulse of the mission. The primary life-limiting mechanism in HETs is the erosion of the discharge channel wall due to ion impacts. Other mechanisms that can cause failure in HETs are cathode failures and thermal shock. Proper design can eliminate these as causes of thruster failure [3].

Ions are created in a 1-10 mm thick ionization region just upstream of an acceleration region towards the exit plane of the discharge channel. In the acceleration region, a 200-500 eV potential drop accelerates the ions. Energetic ions do not always escape the thruster: Some are accelerated into the discharge channel wall. Some portion of the ion population forms sufficiently close to the wall, or with enough lateral velocity to impact. In some cases, the electric field, which is controlled by the magnetic field geometry and electron density, accelerates the ions at an angle that intersects the channel walls. In the region behind the acceleration zone, the discharge channel walls wear away over time, eventually exposing the magnetic circuit. Exposure of the magnetic circuit is considered the end of life for a HET. Further operation of the thruster will degrade performance due to altering the magnetic field. An additional possibility is sputtered ferrous material, ejected into the spacecraft environment causing electrical failure. Figure 1.2 illustrates this process.

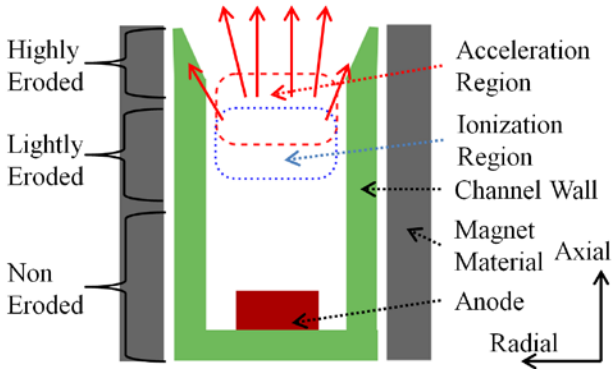

Figure 1.2: Erosion process in HET discharge channel

Before a HET is qualified to fly on a spacecraft, expensive and time-consuming qualification life testing is conducted to demonstrate the lifespan of all components of the thruster under a set of representative operating conditions. These tests typically involve years of operating time, throughputs of hundreds of kg of xenon, and millions of dollars overall. The BPT-4000, for example, was qualified from 2007 to 2009 with 10,400 total hours of operating time, expending 452 kg of xenon in total [4]. During qualification life testing, a single operating condition (thrust, I_{sp}, discharge voltage, mass flow rate) or a single history of operating conditions is explored. However, more demanding thruster applications, such as main propulsion for NASA science missions, require a wide range of throttling capabilities. They may also require a mission to depart from the operating conditions for which the thruster was qualified [5]. Physics-based modeling can help provide confidence in predicting the life of the thruster when operating outside of life-tested conditions, but present models have some limitations.

There are features of the eroded channel walls of HETs that are not reproduced by present erosion models. One significant, and presently unexplained, feature is the

anomalous erosion ridges formed during the long-duration life testing of several HETs, among them the BPT-4000, SPT-100, and PPS-1350G. Figure 1.3 shows the saw-tooth shaped grooves, 10 mm in azimuthal wavelength, which formed during the BPT-4000 qualification life-test. These anomalous ridges complicate the measurement of the average erosion profile. Figure 1.3 through 1.5 show these same features manifesting with thrusters of different sizes and power levels.

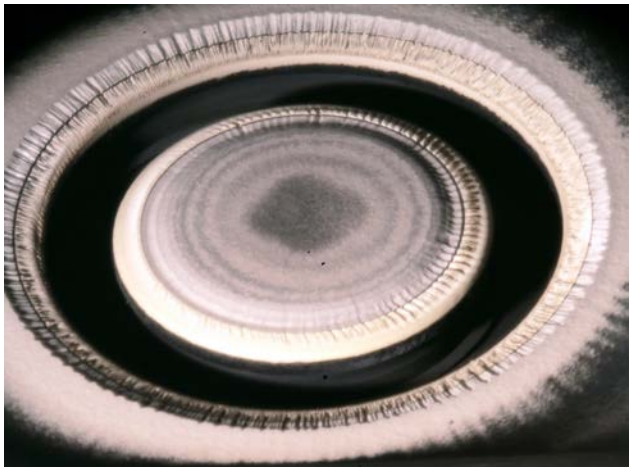

Figure 1.3: BPT-4000 anomalous erosion ridges after 10,400 hrs of exposure, from [4], reprinted with permission from Aerojet Rocketdyne.

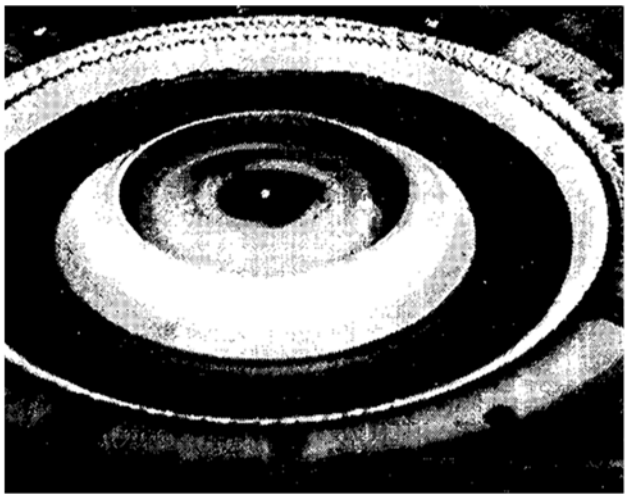

Figure 1.4: SPT-100 after 5730-hr qualification life testing, from [6], reprinted with permission from American Institute of Aeronautics and Astronautics

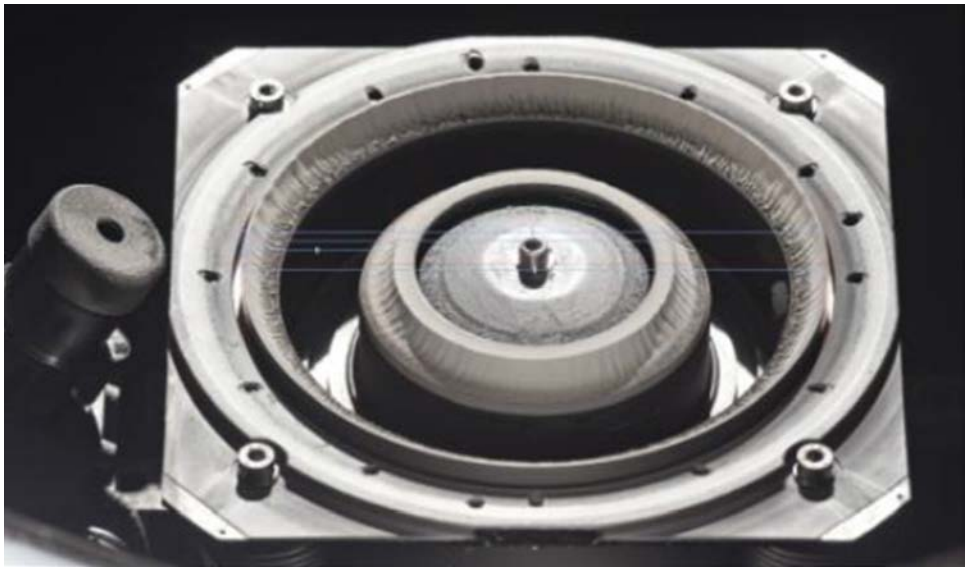

Figure 1.5: PPS-1350G after 2600-hr qualification life test, from [7], reprinted with permission.

Another feature not captured in present erosion models is the roughening of the surface of a dielectric discharge channel due to plasma erosion. Changes in the surface

roughness produce changes in secondary electron emission, which can modify the performance of a thruster by influencing the electron temperatures [8] [9].

1.3. Problem Statement

The present state of the art in predicting the erosion of HET channel walls is given in Chapter 2. Present erosion models treat the material as a homogenous isotropic solid with an ion incidence angle and energy dependent sputtering yield. These models use 2D axisymmetric plasma simulations, along with sputtering yield models, to predict the evolution of HET channel walls.

In order to explain features such as the development of microstructural roughening and composition changes, a more detailed model of the composite channel wall material is necessary. The anomalous erosion ridge phenomenon could also have its origin in the interaction of the plasma with a complex material. A better understanding of the ways in which material properties influence the process of plasma erosion could lead to the understanding of these phenomena and more accurate, high-fidelity life modeling of HETs.

1.4. Research Contributions

This work investigates the erosion of insulating materials by an incident plasma. In particular, the work looks to understand the impact of the material microstructure and mechanical stress on the erosion mechanisms. The results of this work provide five distinct contributions to the understanding of plasma-induced erosion.

The first contribution of this work is the creation of a 3D raytracing model of plasma erosion of a heterogeneous composite material. The eroded channel wall of the

AFRL/UM P5 was studied via SEM microscopy and XPS spectrometry. The details of the composition of the M26 borosil composite were explored with detailed SEM images. Borosil composites, such as M26 have a complex heterogeneous microstructure. The differences in sputtering yield between the fused silica matrix and boron nitride grains lead to the development of complex surface features. A raytracing model was created, which simulated the evolution of a surface profile exposing each material from a 3D material domain to ion bombardment. The model managed to reproduce the cliff-and-valley features observed in microscope images of the surface of the P5. The evolution of observed surface structures can be explained in terms of the model, however, observed changes in the composition of the eroded channel wall surface are not reproduced in the model. Chapter 3 discusses the details of this contribution.

The second contribution of this work is the creation of a thermo-mechanical model that predicts thermo-mechanical stresses for reasonable estimates of plasma heat-flux to the walls and experimentally measured temperature ranges for multi-kW HETs. Experiments provide temperature data and heat flux estimates for the T-140, which inform the modeling effort. Thermo-mechanical modeling provides estimates of the range of thermo-mechanical stresses it is reasonable to expect in kW-class HETs.

The third contribution of this work is the development of a hypothesis, called the Strain Relief Hypothesis (SRH), that is proposed to potentially explain the development of the anomalous erosion ridges in HETs. The theory behind the hypothesis is explained in Chapter 5, and the governing equations are derived. A range of unstable wavelengths that is the function of the stress applied to a material is predicted by the hypothesis. An attempt is made to estimate the speed at which this hypothetical mechanism will

autonomously develop surface features, but due to the disparity in energy density of mechanical strain energy and the process of plasma erosion, predicted time constants are much longer than HET life-times. Due to these, it is shown that the SRH may not be the mechanism to explain the erosion ridges.

The fourth contribution of this work, described in Chapters 6 and 7, is the design and execution of an experiment to test the effect of mechanical stress on the surface features developed during plasma erosion. The experiment is also designed specifically to test the SRH. A test fixture is constructed to apply even compressive mechanical loads to material samples as they are exposed to plasma in a vacuum chamber. Two materials are tested in the experiment: Fused silica and M26 borosil.

Samples are machined to 3x1x0.25 inches, and their surfaces are pre-roughened to produce an even surface finish. Fused silica and M26 borosil samples are exposed to argon plasma for 12 hours, producing eroded surfaces. Mechanical stresses of between 6 MPa and 25 MPa are applied to experiment samples. Before and after exposure, samples are imaged with an Olympus LEXT 3D confocal microscope to produce pre and post-exposure images. A contact profilometer provides detailed statistics derived from line-scans taken on the pre and post-exposure surfaces. Cell patterns are observed to develop on the fused silica samples. The evolution of the M26 samples shows the protrusion of low-yield boron nitride grains from the silica matrix, and the development of a roughness pattern that is independent of initial surface statistics. For both materials, no dependence of the development of the surfaces on the applied mechanical stress, for stresses of up to 25 MPa, has been observed.

The fifth contribution of this work, given in Chapter 8, is the development of two models that explain the observed development of surfaces for each material in the stressed erosion experiment. A distinctive cell pattern develops on the post-exposure fused silica surfaces. A one-dimensional model successfully reproduces the development of the cell pattern using the angle-dependence of the sputtering yield of fused silica. Qualitative and quantitative features of the cell pattern are reproduced with the model. The patterns observed to develop on the M26 borosil samples are explained in terms of the heterogeneous erosion model described in Chapter 3. The evolution of fused silica is explained by the angle-dependence of the sputtering yield of the material. The evolution of M26 is explained in terms of the difference in sputtering yield between the BN grains and silica matrix within the composite material.

1.5. Organization

Chapter 2 provides background on the present state of the art in sputtering yield models of materials and the ways in which these models are used, in conjunction with 2D plasma models, to predict the life of HETs. Some present limitations are discussed towards the end of the chapter.

Chapter 3 discusses the investigation of the eroded borosil channel wall of the AFRL/UM P5 HET. SEM microscopy and XPS spectroscopy of the channel wall material are conducted at several locations on the channel, providing a detailed picture of the material and the evolution of the surface. The evolution of certain surface features is successfully modeled with a 3D ray-tracing sputtering model, which takes into account the differences in the sputtering yield of the BN and SiO_2 components of the material.

Chapter 4 describes the modeling of the heat loading, equilibrium temperatures, and expected thermo-mechanical stresses present in HETs. HETs generate heat loads as high as 8-10 W/cm^2 during operation, and reach equilibrium temperatures of 600 - 800 K. The presence of large heat loads and high temperatures mean that thermo-mechanical stresses of up to 6 MPa may be present during HET operation. The range of stresses predicted is used, along with the hypothesis developed in Chapter 5, to predict a range of unstable surface waves that may develop in HETs.

Chapter 5 describes the development, and the theoretical and quantitative analysis of a hypothesis known as the Strain Relief Hypothesis (SRH). The SRH proposes that the development of the anomalous erosion ridges is the result of an instability driven by the release of thermo-mechanical strain energy in the channel wall.

Chapter 6 describes the design of an experiment intended to isolate and observe the effect of the mechanical stress state on the plasma erosion of a material. A test fixture is designed to hold two material samples side-by-side over a plasma source. One of the material samples (the experiment sample) is placed under a spring-loaded mechanical load. The other sample (the control sample) is held in a basket one inch to the side of the first sample. The bottom surfaces of the samples are exposed to an argon plasma for 11 hours. The plasma exposure produces erosion depths of 20 - 40 μm, and evolves a pre-roughened initial surface pattern to a final surface pattern. Pre and post-test microscopy and profilometry provide images and detailed statistics of the pre- and post-test surfaces.

Chapter 7 describes the results of the stressed erosion experiment. Amorphous fused silica samples are chosen for the first series of tests, so that the effect of mechanical loads can be isolated from the microstructure driven details present HET channel wall

materials. Grade M26 borosil is chosen for the second series of tests in order to observe the effects, if any, of mechanical stresses on a more complicated composite material.

Chapter 8 discusses the results of the stressed erosion experiment. It describes the modeling of the evolution of a surface governed by pure atomic sputtering with an angle-dependent sputtering yield. These physics are able to successfully reproduce the features that are observed to develop on the pre-roughened fused silica surfaces. It also discusses the evolution of the M26 borosil surfaces. It discusses the applicability of the results from a short-duration erosion experiment to longer duration life testing.

Chapter 9 summarizes the key findings of this investigation of plasma-material interaction. Suggestions for future work are provided with the conclusions.

CHAPTER 2

BACKGROUND

2.1. Overview

Because long life-spans for HETs are important to accomplishing large impulses, past work has been done on the topic of plasma erosion, HET life prediction, and life testing. Several levels of abstraction and detail have been studied, from direct experimental testing of thrusters and extrapolation from measured erosion, to computational modeling of single crystal sputtering. This section gives an overview of the work that has been performed with the following sections giving more detail for each effort.

The most costly and time consuming, but most conservative method of estimating thruster erosion, is to perform limited life testing of a thruster. A thruster is operated for a certain period of time, and afterwards the erosion is directly measured. Then, future erosion is extrapolated to estimate when the thruster magnets will be exposed. Section 2.2 gives examples of experimental testing with the NASA-120M thruster and the BPT-4000 thruster.

Less direct, but potentially faster and cheaper, methods of estimating thruster life involve the use of models. Theoretical sputtering yield models provide expectations for the dependence of a material yield on ion incidence energy and impact angle. These provide forms to which empirical sputtering data is fit to produce yield models for a given material. Section 2.2 describes empirical studies of sputtering yields for ceramic

compounds used in EP devices. Experimenters target material samples with ion beams at various angles and energies, and either the mass loss, or captured escaping material is measured.

Theoretical models of sputtering yield are used to interpolate between experimental results. Theoretical models for the sputtering yields of simple polycrystalline metals have been adapted to explain the behavior of more complex ceramics. Section 2.3 and the Cheng and Yim theses discuss examples of these empirical and semi-empirical models [10] [11].

In addition to empirical models of sputtering, Yim has created nano-scale computational simulations of the sputtering behavior of pure hexagonal boron nitride (h-BN). Yim's model bridges the theoretical sputtering yield at low ion impact energy with empirical measurements and yield behavior at high impact energy. Section 2.4 discusses Yim's model [11].

Finally, these sputtering models are employed as part of a HET plasma model to estimate thruster life. Models such as HP-Hall2, and Hall2De have been used to compute plasma properties in a 2D model of a discharge channel. These plasma properties are then used to derive the ion flux into the channel walls and the wall erosion rates. The wall geometry is updated, and the plasma model is solved again, to produce estimates of an azimuthally averaged erosion profile. Section 2.5 discusses these engineering models.

2.2. Empirical Thruster Testing

Peterson and Manzella of NASA Glenn conducted an empirical study of thruster erosion using the NASA-120M research thruster [12]. They inserted several channel

walls of different materials, listed in Table 2.1, and operated the thruster at constant conditions for 200 hours. Afterwards, they measured the erosion profile. Manzella tested boron nitride grades A, AX05, and HP, and borosil grades M and M26 [12].

Table 2.1: Boron nitride and borosil grade composition by mass [13].

Material	BN [%]	SiO_2 [%]	B_2O_3 [%]	Ca [%]	Other [%]
A	90	0.2	6	0.2	3.6
AX05	99	--	0.2	0.04	0.47
HP	92	0.1	0.3	3	4.6
M	40	60	--	--	--
M26	60	40	--	--	--

Grade A boron nitride is a BN material possessing a glassy boric acid binder. Grade HP has higher corrosion and moisture resistance than A or AX05 due to the addition of Calcium. AX05 is high-purity, hexagonal BN that is diffusion bonded and does not depend on binders. Grades M and M26 are borosil, boron nitride-silica composites. Grade M contains more silica, while grade M26 is 60% BN. Grade M26 BN is stated to be widely used in prior Russian SPT thrusters, while grade HP is cheaper to acquire for experimental purposes [13].

Table 2.2 shows some HETs, and the materials which are reported to be in use in their channel walls. Some laboratory SPT-type HETs not listed here also use pure boron-nitride as their channel wall materials.

Table 2.2: Some HETs and their channel wall materials.

Thruster	Material	Reference
Standard SPT-100	BN/SiO_2	[14]
Russian SPTs	70%/23% by mol. BN/SiO_2 composite	[15], [16]
Experimental Russian Thrusters	A BN, Boron-Silica ceramics	[17]
Snecma PPSX000-ML	$BN\text{-}SiO_2$ ceramic walls	[18]
TsNIIMASH D55 TAL	Stainless steel	[19]
Snecma PPS-1350	BN/SiO_2 ceramic	[20]

The profile of the channel wall was measured after each test with a laser profilometer at 0, 90, 120, and 270º. Asymmetries were observed in the erosion of profile relative to the position of the off-center thruster cathode, with greater erosion observed at 0°, the cathode position, than at 180° for all materials and thruster conditions. The most erosion was observed with grade M boron nitride. Grades M26, AX05, and HP showed similar amounts of erosion, with grade A BN showing slightly less than AX05 [12].

A test was conducted to study the effect of varying the operating condition from the 1.65 kW condition used in the material study to a 1.35-kW condition. Inner wall erosion increased, while outer wall erosion decreased under this condition, and the results were explained in terms of the magnetic field topography changing. The magnetic field lines correspond, to within a voltage of kT_e/e, to equipotential contours in the thruster [21]. The region of the acceleration zone where ions pick up enough energy to sputter the channel wall material therefore correspond to where one of the magnetic field lines intersects the wall surface. The location where the radial magnetic field rises to 80% of its value was found to be the furthest upstream location where measureable erosion was

observed for all operating conditions [12]. The accelerating region, where a significant electric field is present, has also been shown to begin where B_r/B_{rmax} rises to 80% [22].

In 2001, General Dynamics Space Propulsion Systems conducted a multi-stage 1000-hour life test of the BPT-4000 HET, that was to be used to validate numerical predictions for the planned 7000-hour qualification life test of the flight weight model. A 600-hr test at 4.5 kW, 300 V, a 200-hr test at 3.0 kW, 400 V, and a 200-hr test at 4.5 kW, 400 V were conducted. The results from coordinate measuring machine (CMM) measurements of the surface were compared with the numerical models, though at the time of the paper, only the first of the series had been completed [23].

2.3. Sputtering Yield Data and Modeling

Materials in common use in HETs of the SPT type include boron nitride and various grades of borosil, as shown in Table 2.1. Borosil combines ease of machinability with low secondary electron emission, high erosion resistance, and a high thermal shock tolerance. Low secondary electron emission is important in governing the plasma sheath physics, which is explained in Chapter 4, covering thermal modeling of HETs. Other materials in common use in other EP devices include silica and kapton.

Garnier investigated the sputtering yield of boron nitride, borosil (of a composition similar to M26), and aluminum nitride, with particular attention to borosil. Garnier measured the sputtering yield using beams of xenon ion incidence energies of 350, 500, and 1000 eV, via weight-loss measurements [15] [16]. This work includes SEM imaging of the roughened features produced by eroding a complex composite material at normal incidence, as well as some of the paradoxical, and currently unexplained changes

in elementary composition due to sputtering [15]. Yalin measured finer details of the angular dependent scattering of sputtered atoms from the surface of three materials: pure boron nitride, quartz, and kapton. These measurements were taken using xenon at 100, 250, 350, and 500 eV ion incidences, and at 0, 15, 30, and 45° ion incidence angle [18]. Yalin integrated the hemispherical scattering measurements to obtain estimates of the sputtering yield of these materials. Britton *et al.* also have data on the erosion of boron nitride investigated through profilometry [19].

These data sets can be used to fit the unknown parameters for several theoretical forms for the sputtering yield. Some forms, such as those developed by Wilhelm [24] [25] based on transition probabilities for ion-atom-atom impacts in a material with binding energy, are only valid for very low energies near the threshold yield energy.

$$Y(E) \approx A * (E - E_{th})^2 \tag{2-1}$$

Other forms, such as the Bohdansky, Zhang, and simplified Yamamura (used in [14] [9]) forms successfully model a wider range of ion energies, including the mid-range ion energies of interest in a HET [26] [27] [28]. The simplified Yamamura form used in Gamero-Castaño is shown in Equation (2-2). E is the ion impact energy. θ is the ion incidence angle. E_{th} is the sputtering threshold energy. $F(\theta)$ is the angle dependence of the sputtering yield. A is a fitting constant.

$$Y(E,\theta) = A * F(\theta)\sqrt{E}\left(1 - \sqrt{\frac{E_{th}}{E}}\right)^{2.5} \tag{2-2}$$

2.4. Nanoscale Computational Modeling of Sputtering Process

In order to improve the theoretical understanding of sputtering yields, and to investigate sputtering behavior at low (<150 eV) ion impact energies where little experimental data has been collected, Yim created a molecular dynamics simulation of heavy ion sputtering of a pure h-BN crystal. The results of this simulation were compared to sputtering yield data from experiments, and to theoretical predictions for low-energy yield models [11].

Yim's molecular dynamics simulation modeled a hexagonal BN-crystal, with a domain size of 13x13x3 nm. The atoms were bound with a Tersoff bond-order potential model, which is a type of intermolecular potential that models covalent bonds, especially the angle dependent energies of covalent bonds, and the energy required to break them [11]. A purely repulsive isotropic Moliere potential was used for the interaction of the xenon ions with the boron and nitrogen atoms.

The domain size was selected to be large enough to contain the area of effect of an ion impact as it produces momentum and energy cascades across the surface. Thermal energy was removed from the bottom of the lattice with a dissipative model. Periodic boundary conditions were used for the sides of the model.

Xenon ions were inserted into the simulation, and the time was advanced, until an amorphous layer of disrupted boron and nitrogen fragments was formed on the surface due to an accumulation of broken bonds. The yield results were gathered, and 200-300 runs were used to derive statistics at each energy level. The computational sputtering yield data was compared with data from empirical sputtering yield experiments. Sputtering yields from weight-loss experiments by Garnier and Rubin, QCM experiments

conducted by Yalin *et al*., and others were compared with simulation experiments at 45° incidence for a variety of ion incidence energies, and at a variety of ion incidence angles.

Agreement to within the error or the range of the experimental data was found between Yim's simulation and Garnier and Yalin's experimental data for BN. In addition to agreement with empirical data, the form of the simulated yield at low ion energies matched the Wilhelm theoretical model well, and transitioned to matching the Zhang form at higher energies [11].

2.5. Computational Life Modeling

Several papers describe the application of the aforementioned sputtering yield models to estimate the life of HETs. Sputtering yield models are applied in 1D and 2D plasma simulations to estimate the erosion rates and geometry evolution of the discharge channel walls.

Gamero-Castaño and Katz used HP-Hall, an axisymmetric 2D plasma code, to simulate the plasma discharge in an SPT-100 thruster [14]. For each iteration, the plasma conditions and a sputtering yield model were used to update the wall geometry. Then, the discharge model was solved again for the next iteration. Gamero-Castaño fit Garnier's yield data for M26 to Yamamura's yield function, producing the model in Equation (2-3), where Y is the sputtering yield in mm^3/C. The fitting constants are given in Table 2.3.

$$Y(E,\alpha) = (B_0 + B_1\alpha + B_2\alpha^2 + B_3\alpha^3)\sqrt{E}\left(1 - \sqrt{\frac{E_{th}}{E}}\right)^{2.5} \tag{2-3}$$

Table 2.3: Gamero-Castaño's yield curve fit [14].

Parameter	Value
B_0	0.012
B_1	-2.60×10^{-4}
B_2	1.30×10^{-5}
B_3	-1.04×10^{-7}
E_{th} (eV)	56.9

The evolution of the SPT-100 channel wall geometry was tracked and compared with experimental life testing conducted by Absalamov. The simulation over-predicts the erosion after about 600 hours at the exit plane, and slightly under-predicts erosion in the acceleration zone. The axial channel location where significant erosion begins was accurately predicted by the model.

Hofer, Mikellides, Katz, and Goebel used an improved 2D axisymmetric plasma model, HPHall-2, to reproduce the channel wall erosion seen during the qualification life test of the BPT-4000 [9]. HPHall-2 improves on HPHall by improving the model of secondary electron yield, and ionization cross section of doubly-ionized xenon. A new energy dependent function for the electron-neutral scattering cross section was also added. One aspect of HET modeling that still requires fitting to experiments is the modeling of anomalous Bohm diffusion of electrons within the channel wall. Bohm diffusion produces electron mobility that is an order of magnitude higher than that predicted by electron-neutral and electron-ion collisions. This effect takes place primarily within the HET channel. The electron mobility model implemented in HPHall-2 was updated with fitting parameters chosen to match experimental performance at 300 V discharge voltage, 1.5 A discharge current.

Hofer chose sputtering yield data from the literature that corresponded with the BPT-4000 channel wall material, and fit a Yamamura curve to it. Hofer notes that the sputtering yield has important free parameters in any current HET erosion calculations [9]. Variations to the normal incidence yield, sputtering yield threshold energy (for which there are no good empirical measurements), and angle dependence, all strongly affect the computed erosion. No data exists for energies below 80 eV, and uncertainties in yield data are significant.

Using results from the plasma model as inputs, Hofer computed the erosion of the BPT-4000 channel walls and compared it to data from the qualification life test. Simulation data for 68, 400, and 933 hrs is compared. On the inner wall, good agreement was found between the experiment and simulation. On the outer wall, erosion was under-predicted after 400 hours [9].

Mikellides *et al.* explored a concept called 'magnetic shielding', where the orientation of the magnetic field lines in a HET direct ions away from the channel walls [29]. The slow-down in the erosion of the BPT-4000 thruster after 5600 hrs of its qualification life test and JPL numerical simulations of this process, inspired the development of the concept. The plasma discharge for an H6 hall thruster, and a variant of the H6 employing a magnetic field geometry optimized for magnetic shielding called the H6-MS, were simulated using Hall-2De. Hall2De is a 2D axisymmetric plasma code using a magnetic field aligned mesh to solve the fluid conservation equations. Hall2De also imposes an empirical transport coefficient function for electron transport, guided by plasma measurements. Comparisons were made between simulations of the unshielded and shielded H6. A comparison was made between experimental data for the unshielded

H6, and the H6-MS simulation, showing a potential hundred-fold reduction in erosion rates [29].

2.6. Limitations of Current Modeling

Due to the 2D nature of the axisymmetric plasma models no azimuthal features are captured. The azimuthal anomalous erosion ridges are not predicted in such plasma codes. Another limitation is that sputtering models that depend only on ion impact energy and angle of incidence, and that treat the underlying material as a homogeneous isotropic solid, have no mechanism for building surface roughness, or surface features like the anomalous ridges. Either an azimuthal asymmetry in plasma conditions or more fundamental detail in modeling the plasma interaction with the material is required to explain these features.

An additional feature that isn't captured by present models is the change in composition of heterogeneous ceramics during plasma erosion. This phenomenon cannot be explained by modeling the material as a homogeneous isotropic solid, as in most models in current use. Garnier [15] and Schinder [30] report changes in relative composition of boron nitride ceramics. These changes are currently unexplained, although a hypothetical mechanism is outlined in [30]. In addition, sandblasting and mechanical abrasion of borosil composites have caused similar composition changes [31].

Qualification life tests to date report only average values for the channel wall erosion depth. The existence of the anomalous erosion ridges is reported, but the ridges

precise azimuthal location is not tracked during the erosion process, nor is depth reported [20] [17].

These limitations in current modeling prompt a more in depth investigation into the details of the plasma erosion process. By looking more closely at the relationship between materials and plasma erosion, it is possible that one or more of these observed features of erosion can be explained, and in the future, modeled.

CHAPTER 3

3D MODELING OF HETEROGENEOUS MATERIAL EROSION

3.1. Overview

In order to better understand the details of plasma erosion, and the plasma interaction with the material of a HET channel wall, the AFRL/UM P5 channel wall was sectioned and studied with scanning electron microscopy (SEM) and x-ray photoelectron spectroscopy (XPS). The P5 channel wall is composed of M26 borosil, a common material used in SPT-type HETs. A model was created of a heterogeneous material domain, designed to mimic the complex material cross section observed during the microscopy. This model simulates the erosion of the borosil surface, taking into account the differences in atomic sputtering yield of the boron nitride and silica components. The model uses ray-tracing to model the protrusion of lower yield material, and the shielding of softer high-yield material behind the low-yield material from incoming ions. The model successfully reproduces some of the surface features observed during the study of the P5.

3.2. P5 Channel Wall Erosion Study

The AFRL/UM P5 HET is a 5-kW HET that was operated under a variety of conditions, for more than 1500 hours, at the University of Michigan. UM operated the P5 under a variety of discharge voltages and flow conditions, as described in the thesis work of Haas, Gulczinski, and Smith. Table 3.1 presents a summary of the operating conditions [32][33][34].

Table 3.1: Summary of AFRL/UM P5 operating conditions [32][33][34]

Run Condition	Discharge Voltage (V)	Discharge Current (A)	Total Flow Rate (sccm)
Gulczinski:			
Condition 1	300	5.3	64
Condition 2	500	5.3	64
Condition 3	500	10	111
Haas:			
Condition 1	300	5.3	63
Condition 2	300	10	63
Smith:			
Condition 1	300	5.3	61
Condition 2	300	10.4	114

Haas and Gulczinski measured the plasma number density profiles and ion energy distributions under these operating conditions. At the 1.6-kW run condition analyzed by Haas, xenon ion number densities were given between 2×10^{17} and 6×10^{17} m^{-3}, and at the 3 kW condition, the ion number densities were between 6×10^{17} and 1×10^{18} m^{-3} [32]. Gulczinski also measured numerous ion energy distribution functions within and around the channel; at the 1.- kW run condition the ion energy distribution function centers around 250 eV with roughly a 50 eV full-width-at-half-maximum[33]. In order to simulate conditions relevant to the environment to which the channel wall has been exposed, this study uses the experimental data described above to define the plasma properties in the numerical model described in section 3.3.

Figure 1.2 shows several regions of an HET channel wall and the degree to which each region is eroded. About 10-20 mm upstream of the exit plane, ions attain the necessary energy to begin sputtering material from the channel wall. Upstream of the acceleration zone, ions are created, but do not yet have enough kinetic energy to sputter

material. Slight discoloration is observed in this region, but not significant erosion. Upstream of the thin ionization and acceleration zones (10-20 mm [21]), no erosion occurs, as the neutral gas does not have enough energy to damage the channel walls. These three regions are referred to as the highly eroded, lightly eroded, and non-eroded regions for the purposes of this study.

The P5 shows a sharp transition between the lightly eroded and highly eroded regions beginning 20 mm from the exit plane of the thruster. The channel wall, shown in Figure 3.1, was sectioned into samples. Figure 3.1 illustrates the regions shown in Figure 1.2. One sample is shown in Figure 3.2. Sub-samples were taken from the surface at each location, and from the interior of the material to provide material for SEM microscopy and XPS analysis.

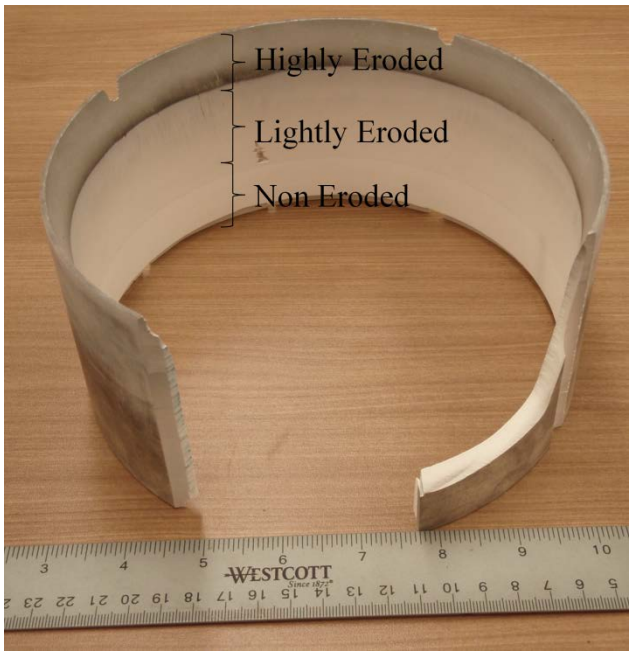

Figure 3.1: AFRL/UM P5 outer channel wall

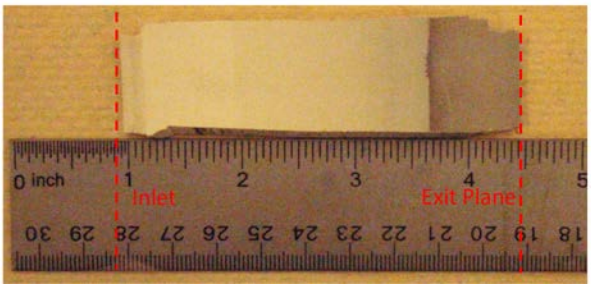

Figure 3.2: Section cut from the P5 outer channel wall

The channel wall of the P5 HET is composed of Combat M26-grade BN-SiO_2. Common materials used for HET discharge channel walls are boron nitride and silica composites (*e.g.*, Combat M and M26) because of their superior machinability and ease of forming over pure BN grades such as A and HBC. The composite is not an isotropic material: In grade M26 (60% BN and 40% silica by mass) highly irregular BN grains are on the order of tens of micrometers wide by hundreds of nanometers thick. These grains are interspersed in a silica matrix, which has large domains of relatively pure silica about 20 μm across. Such microstructures are visible in SEM images of the channel wall, as shown in Figure 3.3.

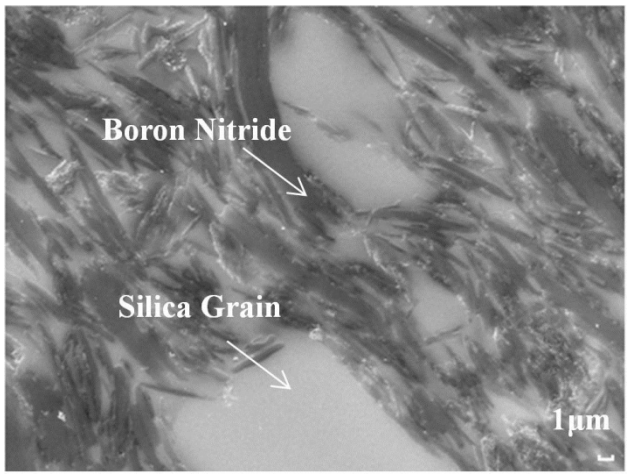

Figure 3.3: Representative cross sectional SEM of M26 BN-SiO_2 composite

Surface profile and composition data were taken and compared with the results of the model. Surface profiles of the channel wall surface were taken with an Olympus-LEXT 3D confocal microscope. XPS spectroscopy yielded information about the surface composition in the three regions. Excerpts from these data are compared with the heterogeneous numerical model in Section 3.5.

3.3. Model Overview

3.3.1. Heterogeneous Model

To simulate the erosion of the channel wall material a three-dimensional model of the sputtering of a binary material has been developed. This 3D model reproduces some important features of the surface structures that were found in measurements of the eroded P5 channel wall, and the model provides insight into how a heterogeneous material drives the formation of 3D surface roughness and geometry. Unlike prior models that generate average behavior, the model developed in this work generates surface profiles from the interaction of a plasma with the material microstructure.

A continuum model of erosion is justified, due to the scale of the atomic sputtering events and the rate at which ion impacts occur. The scale of atomic sputtering events is on the order of 1 to 10 nm, with yields of cubic nanometers or less per impact, according to the scales of atomic sputtering observed in experiments [15][35][16] and theoretical tools such as Stopping Range of Ions in Matter (SRIM) [36]. The grid spacing chosen during simulation is on the order of tenths of microns for the small-scale domain model, and 1 μm for the large scale domain model, with the impact rate on the order of 10^9 impacts/μm^2-s. The scale of atomic sputtering events is much smaller than the scale of the grains. In addition, the erosion of pure materials (Silica, HP BN) is an accumulation of atomic-scale sputtering events, so data collected from atomic sputtering of BN in HP-BN should be comparable to the erosion of BN in borosil composites. In both cases, the atomic sputtering event is concerned only with the immediate neighborhood of a few nm.

In the present approach, ray-tracing techniques are used to determine the regions of the material surface that are exposed to ion bombardment, or shadowed. Each material phase has its own component atomic sputtering model, which returns the sputtering yield as a function of impact angle and energy. Both BN, and SiO_2 exposed surfaces have a separate angle and energy dependence to their yield functions and erosion rates. The ion impact angles are calculated based on the local incidence angle of each velocity component of the plasma. Figure 3.4 shows the ray tracing approach.

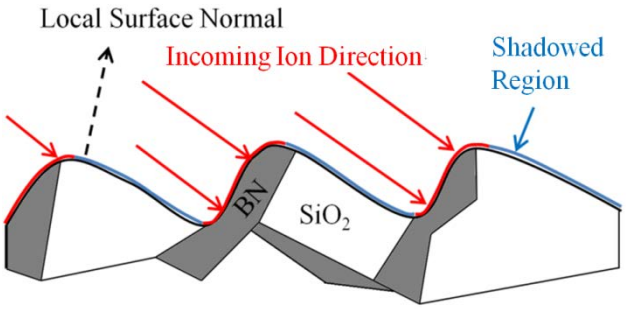

Figure 3.4: Ray-tracing approach to differential sputtering

3.3.2. Flow of Execution

The sputtering model consists of a model of the 3D material domain, a model of the plasma, and a model of the two-dimensional surface geometry. During the modeling of erosion, a volumetric region of material information is generated, and the surface mesh is initialized at the top of the simulation domain. The surface mesh is initialized with a flat smooth surface. For each timestep, the material type at each point on the surface is calculated, along with the local surface normals. Then, the shadowing is calculated to determine whether or not ions can impact each point on the surface. Next, the local erosion rate is calculated as a function of the material, the ion energy and direction, and the local surface normal. Finally, the surface mesh geometry is updated. Nodes heights (z coordinates) are adjusted according to local volumetric loss rates, the vertical cross sectional area bordering the node, and the timestep. Each node's z coordinate is adjusted at each timestep to update the surface geometry. Figure 3.5 shows the sequence of execution for the model.

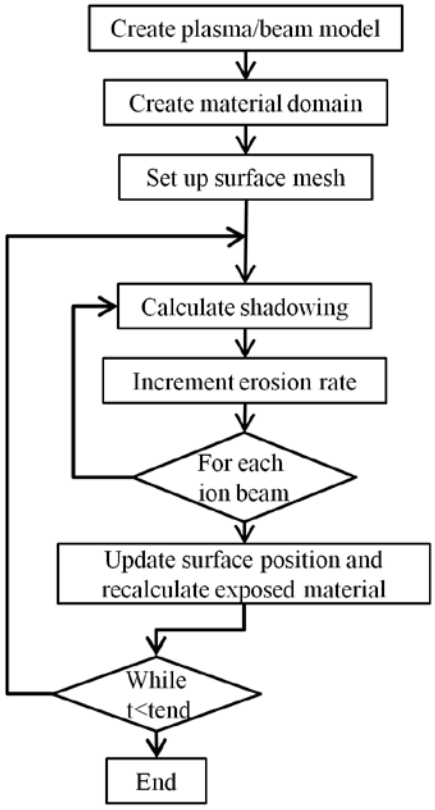

Figure 3.5: Sputtering model flow chart

3.3.3. Discretization Scheme

The surface is discretized as a two-dimensional regular grid. For each point on the surface, the local normal is calculated in terms of the height of the four adjacent nodes. The local surface area exposed for each node is the cell area divided by the cosine of the local surface normal angle with the vertical.

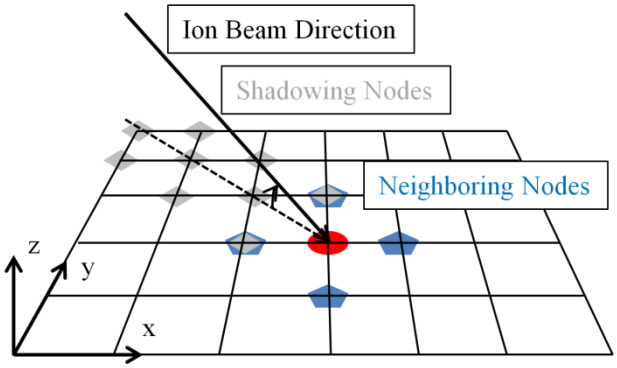

Figure 3.6: Surface mesh: Neighboring nodes are used to calculate local normal, shadowing nodes calculate whether node is obscured.

The local surface normals are calculated as shown in (3-1)-(3-3).

$$\begin{cases} g_x = \frac{1}{2}\left(\frac{z_{i+1,j} - z_{i,j}}{x_{i+1,j} - x_{i,j}}\right) + \frac{1}{2}\left(\frac{z_{i,j} - z_{i-1,j}}{x_{i,j} - x_{i-1,j}}\right) & (3\text{-}1) \\ g_y = \frac{1}{2}\left(\frac{z_{i,j+1} - z_{i,j}}{y_{i,j+1} - y_{i,j}}\right) + \frac{1}{2}\left(\frac{z_{i,j} - z_{i,j-1}}{y_{i,j} - y_{i,j-1}}\right) & (3\text{-}2) \\ \hat{n} = \frac{[-g_x - g_y \; 1]}{\sqrt{g_x^2 + g_y^2 + 1}} & (3\text{-}3) \end{cases}$$

During each timestep, for each ion beam direction, whether or not a given node is in shadow is calculated based on whether or not the ion beam vector intersects any triangle formed by a trio of the nodes along the line of sight of the ion beam vector. To reduce the required computational time, only those nodes along the line of sight are compared when calculating the shadowing.

3.3.4. Plasma Model

In a HET, ions are accelerated to a high velocity, mostly along the axial direction, but they also have a distribution of speeds based on where they were ionized within the accelerating potential drop. The simulation software is capable of modeling either single mono-energetic ion beams, or plasma with a distribution of velocities. A first-order model of the plasma is produced using a displaced Gaussian distribution of ion velocities, with a pseudo-temperature governing the spread, and an average flow velocity. The single ion beam model is used for moderate incidence angles where the 5º of spread in ion angle is not significant. The full plasma case is used to model a plasma travelling parallel to the wall, with the variation in normal velocity causing drift into the wall.

The model captures the variation in ion energies and the variation in the angle at which the ions impinge on the surface by dividing a Maxwellian velocity distribution into velocity classes. A plasma mean velocity is assumed, related to the mean velocity of the ions after passing across the acceleration potential drop in the discharge channel. An effective pseudo-temperature for the ion energy is also assumed, chosen based on the ion energy distribution measurements in the works of Gulczinski and Haas [7, 8], which produces a Gaussian distribution of velocities around the center velocity. For each dimension of velocity space, the distribution is then partitioned into velocity classes. The fraction of the total ion number density is binned for each of these velocity classes, and this fraction is normalized so that the total fraction for all bins sums to one. An ion beam structure is created for each velocity class, with the energy and direction calculated from the center velocity of the velocity class bin. Equations (3-4)-(3-5) show the expression for a Gaussian velocity distribution offset by a relative mean velocity.

$$\begin{cases} f_{vi}(v_i) = \sqrt{\dfrac{m}{2\pi k_b T}} \exp\left(-\dfrac{m}{2k_b T}\left(v_i - v_{center,i}\right)^2\right) & (3\text{-}4) \\ f_v(\vec{v}) = \prod f_{vi}(v_i) & (3\text{-}5) \end{cases}$$

Using this model, the simulation calculates shadowing and erosion rates for each ion beam. The erosion rates are summed for a total erosion rate, and the surface depths are then updated.

3.3.5. Material Domain Model

Two different material domain geometry models are used to capture features and behavior at different scales. Each model uses a different grain geometry and interprets the remaining material as a matrix. A small-scale model uses long, thin triangular BN grains that are embedded in a silica matrix. A large scale model uses approximately 20-μm silica regions embedded in BN rich regions.

A small-scale model, an example of which is shown in Figure 3.7, with mesh sizes on the order of tens of micrometers on a side, is intended to capture individual BN grains. The BN grains are modeled as triangular flakes interspersed in a silica matrix. The BN grains have a uniformly distributed randomized width and length-scale based on minimum and maximum specified lengths and thicknesses. Lengths and thicknesses are chosen to produce material cross-sections similar to those imaged experimentally in the SEM of the interior of the P5 channel wall material. The grains are placed with a random orientation within the simulation domain, until a 60% BN volume fraction is achieved.

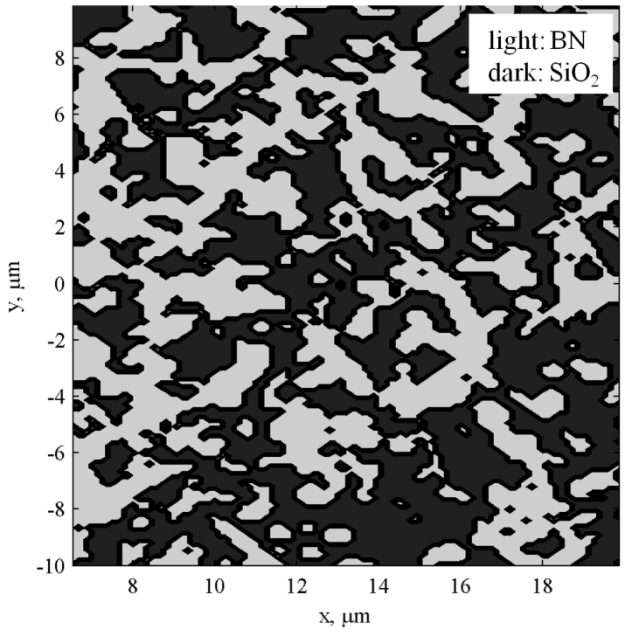

Figure 3.7: Small-scale material model cross section

The large-scale model, with mesh sizes on the order of hundreds of micrometers, is intended to capture the larger-scale surface roughness, and the large silica grains. An example is shown in Figure 3.8. These silica grains, modeled as ellipsoidal regions, are placed randomly throughout the domain until a 40% silica volume fraction is achieved. The interstitial area is assumed to be dominated by BN grains, although no attempt is made to resolve the individual grains.

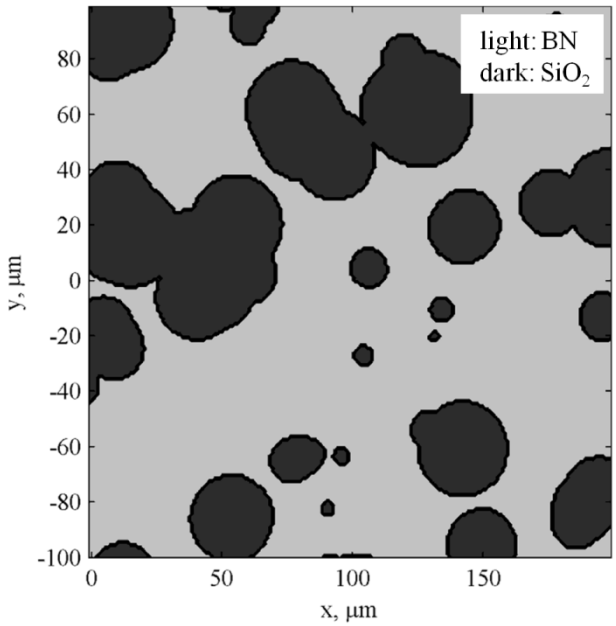

Figure 3.8: Large scale material model cross section

3.3.6. Component Atomic Sputtering Models

A homogenous isotropic sputtering model for M26 BN-SiO_2 is provided by Gamero-Castaño, who produced a curve fit to experimental data collected by Garnier [14][15][16]. Yalin produced experimental atomic sputtering yield data for HBC boron nitride, an almost pure BN material, and for quartz [35]. Curve fits to these data were made by adjusting parameters to minimize the sum of squared error of the fit to the data. The HBC and SiO_2 curve fits are used for the BN and SiO_2 components of the present model. The models are of a form given in Equation (3-6), and the coefficients are listed in Table 3.2 below. Y is the sputtering yield in mm^3/C incident ion current, E is the impact energy in eV, E_{th} is the sputtering threshold energy, and α is the incident angle in degrees. The sputtering yield is the volume of material ejected for a given incident current, assumed to be singly ionized, in Coulombs.

$$Y(E,\alpha) = Y_E(E)Y_\alpha(\alpha) = k(B_0 + B_1\alpha^1 + B_2\alpha^2 + B_3\alpha^3)\sqrt{E}\left(1 - \sqrt{\frac{E_{th}}{E}}\right)^{2.5} \quad (3\text{-}6)$$

Table 3.2: Material model coefficients

Variable	**Gamero-Castaño M26 (60% BN, 40% SiO_2)** [14]	**Yalin HBC (99% BN)** [35]	**Yalin Quartz (Silica)** [35]
E_{th} (eV)	58.6	18.3	18.3
B_0	9.90×10^{-3}	1.18	9.14×10^{-1}
B_1	0	1.94×10^{-2}	5.34×10^{-2}
B_2	6.04×10^{-6}	-1.22×10^{-4}	-6.98×10^{-4}
B_3	-4.75×10^{-8}	-2.22×10^{-6}	3.33×10^{-6}
K	1.00	2.28×10^{-3}	3.50×10^{-3}

Figure 3.9a shows the curve fits to the experimental data at 45º ion incidence. All data sets have data at this angle. Figure 3.9b shows the relative yield as a function of incidence angle. The data provides an example of the large variation in sputtering yield in the literature. Garnier measured the erosion of M26 with a mass-loss method. Yalin measured sputtering yield by collecting sputtered material on a quartz-crystal microbalance, correcting for losing mass as nitrogen gas. At ion energies of more than 250 eV, Garnier's fit for M26 has a higher modeled yield than Yalin's model for silica. This may not be physically realistic, as silica is the highest yield component of the BN-SiO_2 composite, and BN-SiO_2 is supposed to be lower-yield than pure silica. This demonstrates the variation in the data and models for material sputtering in current use.

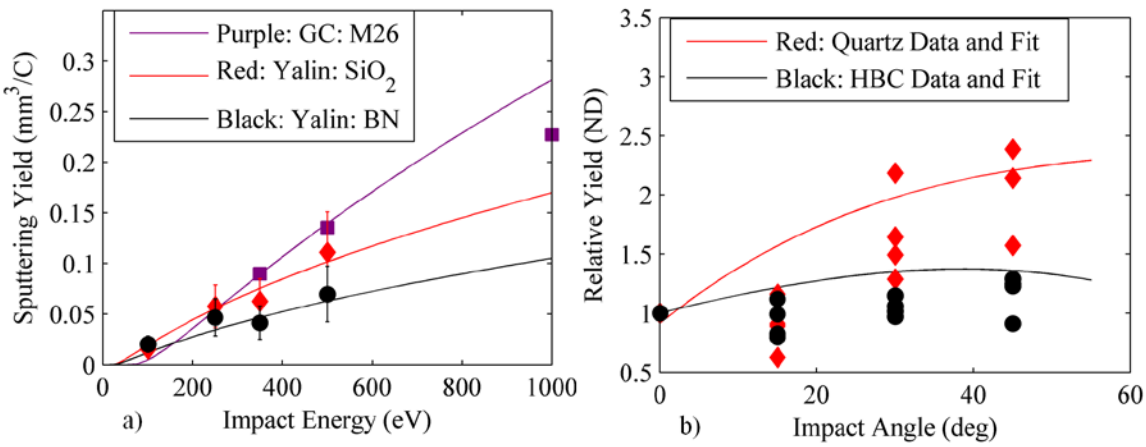

Figure 3.9: a) Sputtering yield data from [35], [16], and curve fits for *Y* as a function of ion impact energy at 45° incidence. b) Relative yield as a function of impact angle, data and curve fits.

3.3.7. Analysis of Simulation Convergence

A convergence study is conducted at both small-scale and large-scale domain sizes to confirm the numerical stability of the simulation. Numerical instability and divergence of the results were found to occur for large time steps originating in areas of large curvature. The instabilities took the form of ripples which propagate from these areas. If the ripples are large enough, they interact significantly with the shadowing, and instability results. This effect is most extreme at shallow incidence angles, so shallow incidence angles are used as the limiting case for the convergence study. Table 3.3 shows the run conditions of the convergence study.

Table 3.3: Convergence study run conditions

	Small Domain Study	**Large Domain Study**	
Domain Size	30 x 16	200x100	μm
Mesh	400x200	200x100	
Material:	BN Flakes	Ellipsoidal Silica Grains	
Min length-scale	3	0.1	μm
Max length-scale	10	10	μm
Min radius scale	0.1	5	μm
Max radius scale	0.4	20	μm
BN volume fraction	60	60	%
Ion energy	245.6	245.6	eV
Incidence Angle	1.5˚	5˚	
Number Density	$3x10^{17}$	$3x10^{17}$	m^{-3}

For the small domain study, the average erosion rate came to within 5% of the asymptotic value at a timestep of 0.5 s, and the rms roughness of the produced profiles converged. For the large domain study, the average erosion rate approached 0.5% of the asymptotic value at a timestep of 2 s. Figure 3.10 shows the convergence of the average erosion rates. These timesteps were used in subsequent simulations at these relative mesh sizes.

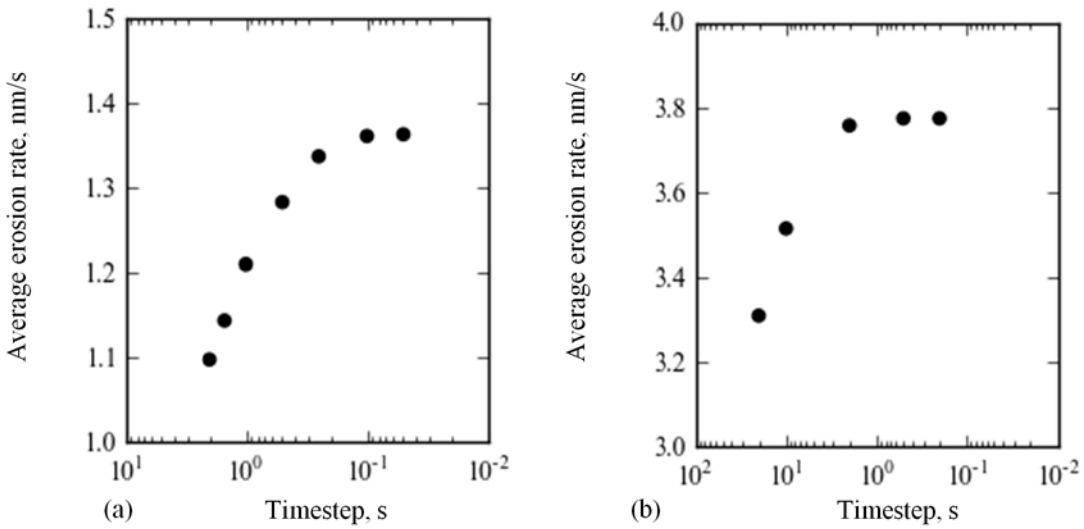

Figure 3.10: Convergence of average erosion rates a)small-scale domain model, b) large-scale domain model

3.3.8. Verification of Implementation

In order to confirm that the behavior of the model is physically reasonable, and related to the more basic component models for each phase, several large-scale domain models are generated. Each material domain model has a different silica volume fraction, ranging from 0% (no silica grains) to 100% silica. The incidence angle of the ion beam is set at 30º. It is expected that the behavior of the model is identical to that of the component models when only that material is present. No surface features should form, as the erosion rate is constant across the entire surface. In addition, the average rate of erosion should be a smooth function of the fraction of the surface composed of each material.

Figure 3.11 shows the average erosion rates produced by the models. In the limiting case where either material fraction is 100%, no surface roughness or features are

produced, *i.e.*, the simulation produces a flat surface for each timestep, and the recession rate agrees exactly with the component models.

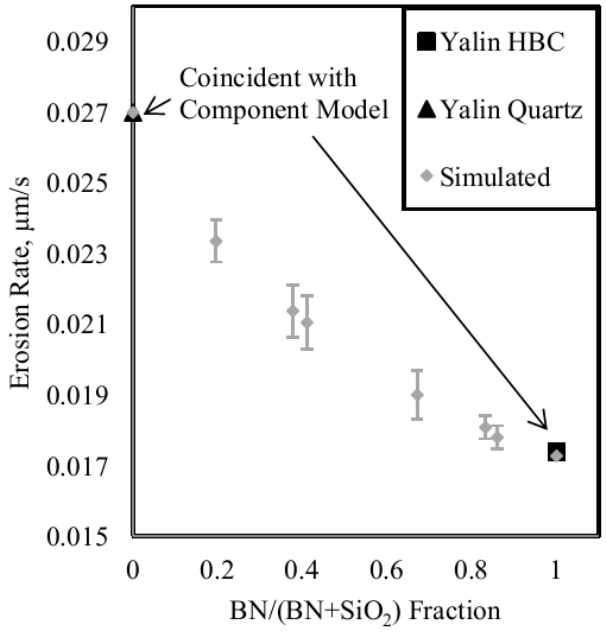

Figure 3.11: Average and one standard deviation of erosion rate: Comparison with component models.

The trend of the series of simulated average erosion rates is bracketed by the component models, and varies smoothly. The reproduction of the component model behavior in the limits of composition, and well behaved solutions in between are taken as verification of our implementation of the two-phase model.

One aspect of the behavior of the composition series is that the average erosion rate deviates from a linear relationship. A linear relationship would be expected of a simple rule of mixture for the exposed material. This extra behavior is an effect of the developing surface structures and highlights the need for models that capture heterogeneous features.

3.4. Results

Using the model presented so far, several numerical results were derived. The small-scale material domain model produced profiles similar to the tenth-micrometer erosion striations seen in close-up SEM imagery of the P5 channel wall surface, as seen in Figure 3.12. Ion flow at shallow incidence angles produces long thin streak-lines. Cases where the flow is locally parallel to the larger scale structure appear to produce these. In this section, ion incidence angles are reported as the angle that the ion flux makes with the surface plane.

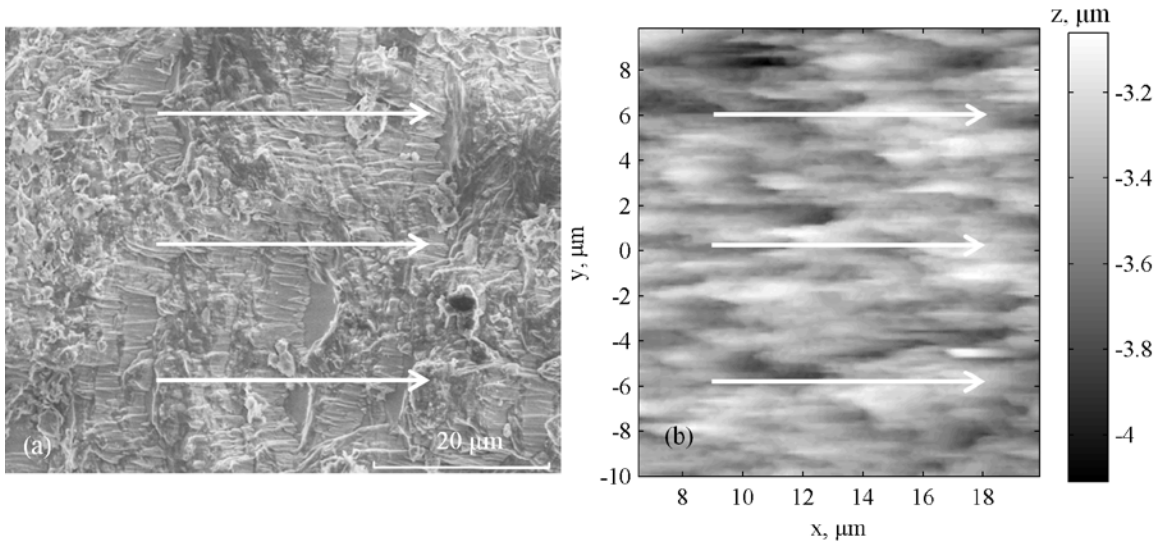

Figure 3.12: a) SEM image of P5 channel wall, b) Small scale simulation, 20° incidence, 750 s, 10^{17} m^{-3}, showing similar patterns

The large-scale material domain models provide the most features for comparison with our experimental data from the channel wall. Single ion beam models are used at several angles of attack to the simulated material domain. Table 3.4 lists the conditions for the large domain simulations.

Table 3.4: Run conditions, large scale simulations

Domain	400x200 μm
Mesh	400x200
Material	Ellipsoidal Silica Grains
Min length	0.1 μm
Max length	10 μm
Min radius	5 μm
Max radius	20 μm
BN volume	0.6
Ion Beam Properties	
Ion Energy	250 eV
Angles	[5°, 10°, 15°, 20°, 30°, 45°, 90°]
Number Density	3.00×10^{17} m^{-3}

The surface profiles of the simulated regions show the following in terms of erosion rate as a function of angle: The average erosion rate quickly approaches a steady-state value that persists through the entire evolution of the surface profile with only minor variations, as shown in Figure 3.13.

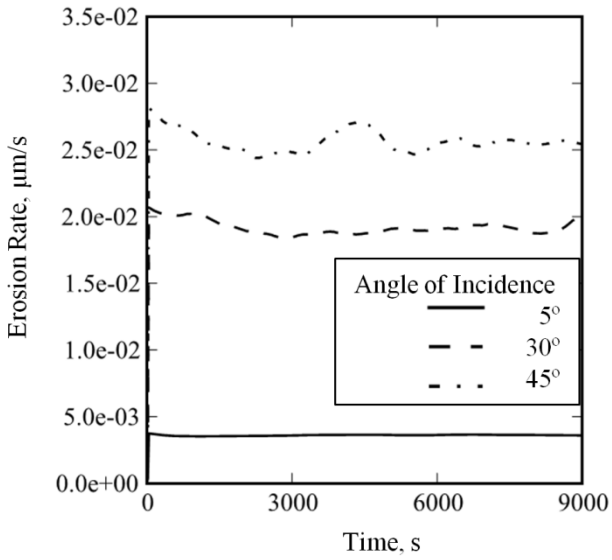

Figure 3.13: Average erosion rate as a function of time, ion incidence angles of 5, 30, and 45°.

The surface profiles of the large-scale angle series are not uniform, and develop over time. Eventually, the qualitative nature of the surface appears to remain unchanged after erosion depths of ~200 μm. Materials with lower sputtering yields protrude from the surface at various places, and erode away, but the relative magnitude of the features appears stable. The rms roughness of the surface continues to increase throughout the simulated time span, albeit with an apparent logarithmic or asymptotic slowdown as time advances, corresponding to the mature surfaces. The magnitude of the rms roughness profile that develops, along with the nature of the surface features, is a strong function of the incidence angle of the ion beams.

For example, each of the angle series simulations was run for 18000 s of simulated time. The 5° case achieved a shallower depth at the end of the simulated period. Figure 3.14 shows the rms roughness achieved at three ion beam incidence angles as a function of erosion depth.

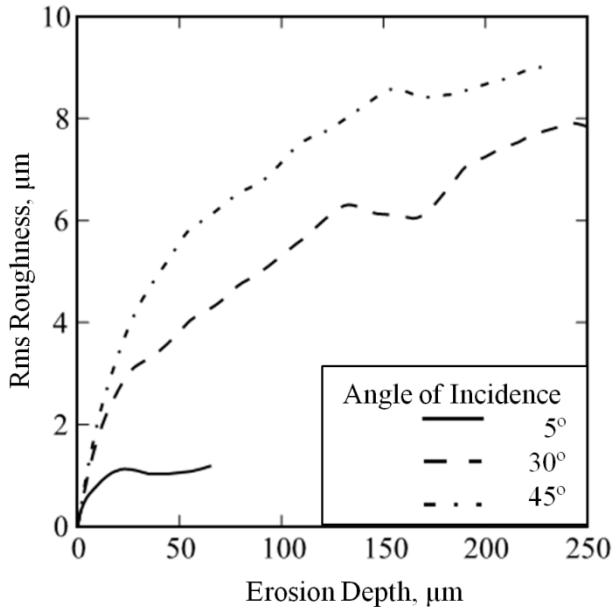

Figure 3.14: Rms roughness as a function of erosion depth, ion incidence angles of 5, 30, and 45°.

A 24,000 s simulation with a coarser grid and larger domain is run at 30° incidence to investigate the boundedness of rms roughness for long erosion times. This is shown in Figure 3.15. At 470 μm erosion depth, the rms roughness is still below 9 μm and is comparable in magnitude to the results from the finer large-scale simulation (Figure 3.14). The peak-to-valley distance has not yet reached a limit at 470 μm, pointing to the development of larger-scale structures as the simulation advances.

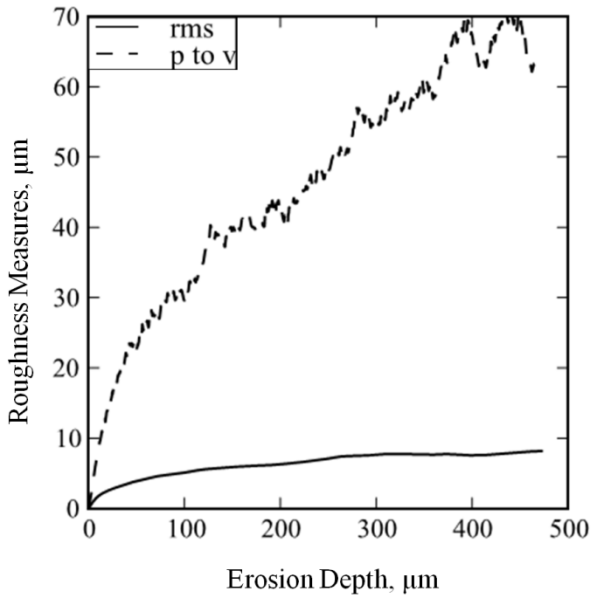

Figure 3.15: Rms and peak-to-valley roughness, 30° ion incidence, w coarse timestep, long duration.

The relative presence of BN relative to SiO_2 is quantified in terms of the proportion of upward facing surface area on the simulated domain as a function of time. The evolution of the BN/SiO_2 ratio remains within 10% of the starting value, the average volume fraction in the material, with no coherent trend up or down as the material erodes.

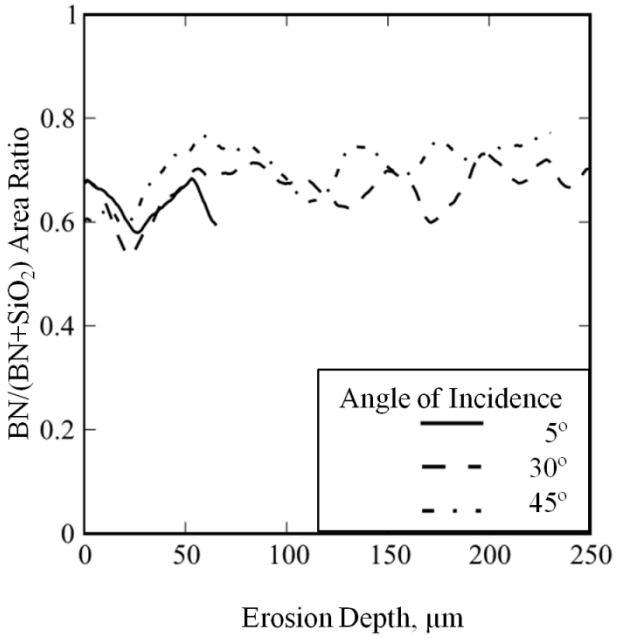

Figure 3.16: BN/(BN+SiO_2) surface area ratio as a function of erosion depth

3.5. Discussion

The fist main observation from the model behavior is about the qualitative nature of the generated surface features. Figure 3.15 shows that the model produces surfaces that are qualitatively mature after erosion depths are achieved on the order of a few times the length of the largest grain features. Local variations in mesh height and feature size appear to approach a steady state, as does the rms surface roughness. Peak-to-valley roughness, which is sensitive to the largest surface features generated continues to increase, even after long simulation times and 470-μm erosion depths. This suggests that with larger domains and longer times, larger scale surface features may result from the continued operation of the model.

Surface structures observed in SEM imaging of the eroded P5 channel wall are reproduced in the heterogeneous erosion model under certain beam and plasma

conditions. The natures of the features produced by the erosion model are highly dependent on the angle at which the ion beam impinges on the surface of the material.

SEM imaging of the highly eroded surface shows cliff-and-ridge structures (what Morozov [17] calls "pike-tongue" structures). These structures are on the order of 20-μm wide and 20-40 μm long. Contrast on the secondary electron emission shows higher BN concentrations near the front of these structures. The large-scale model runs also produce similar structures, resulting from the boron nitride shadowing the softer silica grains behind them. The BN ridges shield the silica cliffs from the bulk of the incoming ions. This is shown in Figure 3.17.

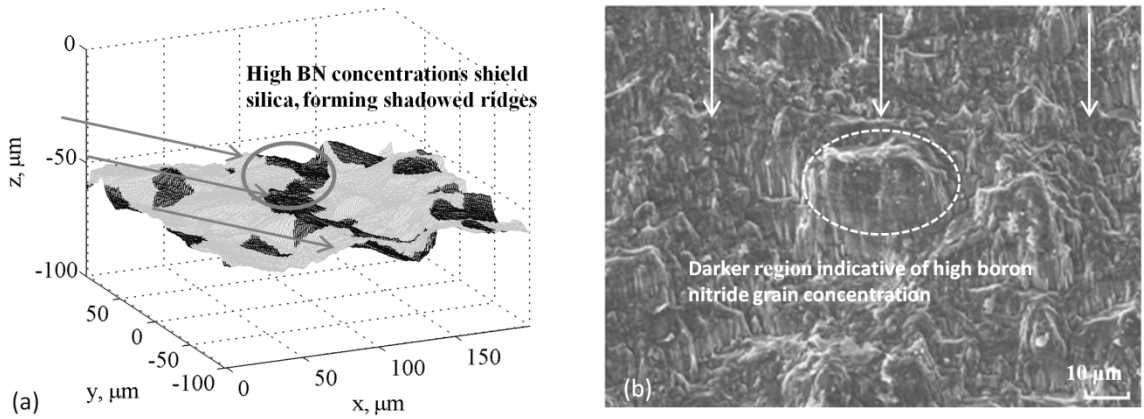

Figure 3.17: a) Simulated erosion surface, b) SEM image of highly eroded section of channel wall.

Figure 3.17 demonstrates the behavior of the two-phase material model. This is for an incidence angle of 30º, 3×10^{17} m^{-3}, 750 s simulation. These cliff-and-valley structures are also comparable in horizontal and vertical magnitude to those seen during profilometry of the eroded channel wall samples. An Olympus LEXT 3D confocal microscope is used to produce surface profiles of each of the three regions of interest on the samples. In the highly-eroded region, the scales of the eroded features in the profiles are similar to those produced by the 30º and 45º incidence angle simulations, as shown in

Figure 3.18. Figure 3.18 a) is an empirical profile of the highly eroded region of the P5 thruster channel wall, measured with the LEXT. Figure 3.18 b) demonstrates the similarity in the peak-to-valley depth and feature size developed in the simulation.

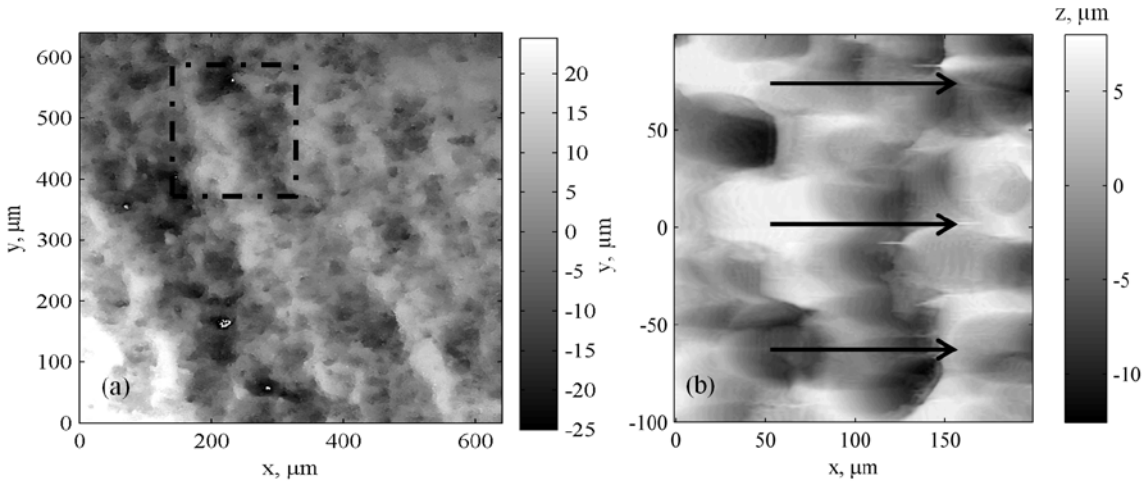

Figure 3.18: a) Optical profile of P5 channel wall, b) Simulated profile, 30º incidence, 750 s.

The second main observation is the good agreement between simulated and empirical rms roughness. The profilometry of the highly-eroded surface indicates an empirical rms roughness of around 6 ±2.5 μm. This is similar to where the rms roughness of the 30º simulated case appears to asymptote (Figure 3.15). The simulated roughness developed is a function of the largest heterogeneous surface features, in the case of the large-scale material domain model, the 20-μm silica grains govern the erosion.

Not all simulated incidence angles produce surface features and roughnesses comparable to what we see experimentally. Normal incidence angles produce vertical shapes where the harder to sputter material protrudes from the softer silica materials. At parallel incidence angles, the simulated surface is only very slowly eroded, and the aspect ratios of the structures produced tend towards being semi-infinite. This produces a smooth polished surface.

Haas's plasma potential contour measurements in the P5 discharge channel suggest that the ions should experience acceleration largely along the axial direction, with little acceleration in the radial direction, as expected of contemporary HET designs [32]. However, note that Haas's measurements were taken at some distance from the wall, and do not account for the radial acceleration of ions due to the plasma sheath at the boundary between the channel wall and the plasma.

Cross sections of the P5 channel wall have a sharp boundary between the highly eroded and non-eroded region, shown in Figure 1.2, corresponding to the location of the acceleration zone of the plasma. The highly-eroded region is inclined to the axis of the channel wall by about 17º, suggesting that the plasma is initially impacting the surface at a moderate incidence angle. In the long-duration life testing of the BPT-4000, it was found that the majority of the erosion occurred during the first 6,700 hrs of operation, after which no measurable erosion occurred: A limiting shape for the discharge channel was obtained [4]. In summary, we expect to see the observed surface features only when ions impact at a given angle.

The third main observation from the model behavior is that surface structures are only generated due to atomic sputtering, starting from a flat surface, when there is heterogeneity to the material. In Figure 3.11 the pure BN and pure silica models produce flat surfaces, which erode at a rate exactly mirroring that of the pure component sputtering models. In simulated cases where the erosion is allowed to proceed past the defined material domain, into a region of pure material, any surface structure which is produced begins to decay back into a flat surface.

The average erosion rate of the surface is between that of the two component atomic sputtering models, as shown in Figure 3.11 and Figure 3.19. However, the variation of the average sputtering rate with the mixture fraction is not the linear law-of-mixtures that is expected from a flat featureless surface. This demonstrates the effect of surface structures in perturbing the average erosion rate. Due to the shadowing effect, the average erosion rate is closer to that of the slower sputtering material than would be expected from a linear law of mixtures.

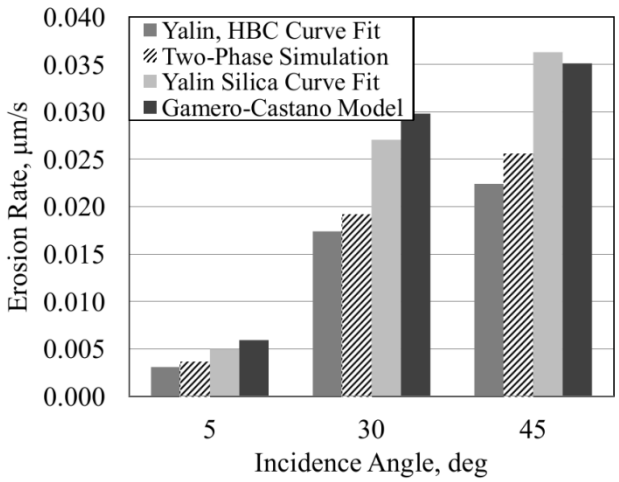

Figure 3.19: Average erosion rate of simulation and component models as a function of incidence angle.

The fourth main observation concerns the composition of the eroded surface. XPS measurements are taken of the relative concentration of elements on the surface of the P5 samples. These measurements indicate that BN is depleted relative to silica in the highly eroded region of the thruster. This surprising result mirrors that obtained by Garnier in his erosion experiments on BN-SiO_2 target discs [15]. However, Zidar took energy dispersive spectroscopy (EDS) data from an eroded channel wall that instead indicated increased BN presence near the eroded end of the channel wall, differing from our results

and those of Garnier [15]. Further investigation of the difference between our measurement results would be of interest. This result contrasts with the predictions of the model shown in Figure 3.16, which shows that after a brief ~10% increase in the surface concentration of BN relative to silica, the relative composition is predicted to remain constant as erosion proceeds.

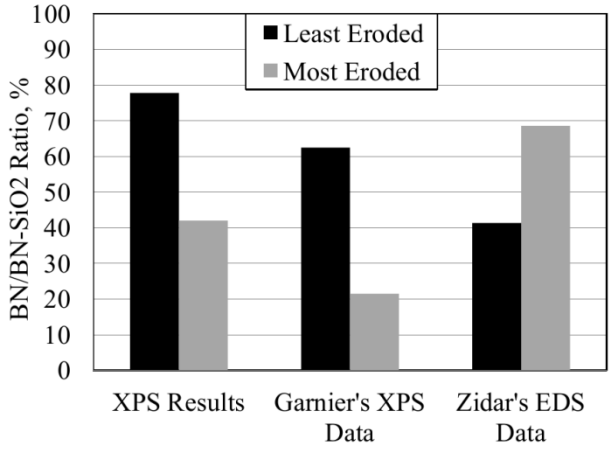

Figure 3.20: BN/(BN-SiO_2) ratio, %, [15][37]

In Figure 3.20, XPS Results refers to measurements conducted on the P5 channel wall in the highly eroded and non-eroded region. Garnier's XPS data refers to measurements taken pre and post-exposure on BN-SiO_2 targets. Zidar's EDS data refers to EDS taken at 45 mm and 5 mm from the exit plane of an eroded HET channel wall.

The atomic sputtering model for pure BN and SiO_2 as components does not account for the observed changes in surface composition. Atomic sputtering alone would predict that BN would protrude from the silica matrix, and persist relative to the softer to sputter silica material. The model behavior is such that the relative amount of exposed BN increases slightly but remains within 10% of the average material in the matrix, as shown in Figure 3.16.

In order to illustrate the difficulty with a pure sputtering approach capturing the change in surface composition, a simple model is presented. In the model, a flat surface plane propagates through a regular domain, shown in Figure 3.21. As the surface plane is moved into the domain, the intersection of the surface with the grains produces a similar, but translated, image to the initial intersection image. According to this model, the exposed area proportion of the BN grains and silica matrix should remain the same. In the sputtering model, this may be modified due to exposure of the lower-yield grains, but significant variation is not observed in the present model.

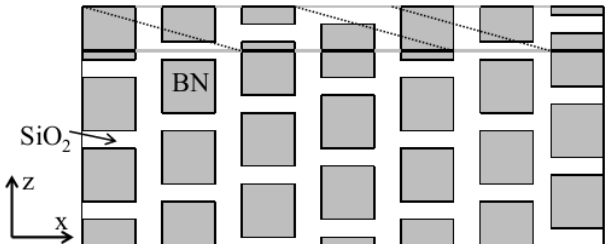

Figure 3.21: Simple regular domain model

If the analytical model is modified so that when BN grains which lose a critical amount of support in the surrounding matrix are removed, it could account for the changes in the silica. In this model, depicted blow in Figure 3.22, the BN grains protrude from the matrix as it is sputtered. When the BN has a small enough supporting surface area in the silica, the grain is removed, leaving a shallow depression behind. In this case, the upward facing area due to silica increases after the BN grains are removed.

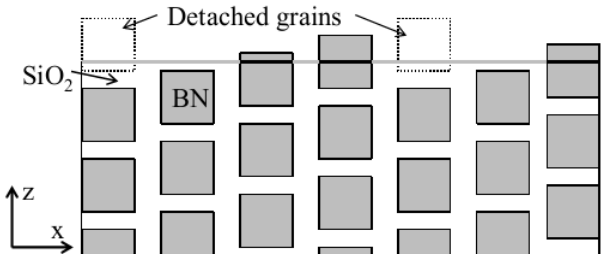

Figure 3.22: Composition changes due to ejection of grains with small support

In order to explain the variation in surface composition, another mechanism, such as the grain-ejection mechanism proposed, is needed. Atomic sputtering does not predict the decrease in BN in the HE region. Grain ejection provides a plausible mechanism that could explain this surprising observation.

3.6. Summary

This portion of the effort contributes to the understanding of plasma-material erosion processes by providing details how the complex heterogeneous nature of the borosil material used in the P5 channel wall effects the development of surface structures. The AFRL/UM P5 channel wall was investigated with XPS, SEM, and optical microscopy. A model of atomic sputtering of a heterogeneous material is capable of reproducing some features observed experimentally in the eroded section of the P5 channel wall. The ridge and cliff structure to the surface can be explained by BN, which has a lower sputtering rate, shielding the softer silica material behind it. The surface features produced by the model are a strong function of the angle of incidence of the ions. The observed ridge and cliff structures are similar to those produced by ions which impact at an angle of 30º. Experimental rms roughness in the eroded channel wall are similar to those produced by the model for incidence angles of 30º. This suggests that the

plasma was impacting the P5 channel wall at a moderate angle of incidence. Variation in the modeled material composition produces variation in the average erosion rate, as expected. However, the average erosion rate deviates from what is expected from a simple law of mixtures, which demonstrates the significance of the surface structure and shadowing. Average erosion rates are biased towards erosion rates of the component with the lowest sputtering rate in the mixture.

CHAPTER 4

THERMAL MODELING OF HET CHANNEL WALLS

4.1 Overview

Understanding the thermo-mechanical stresses that are present in HET channel walls is of interest on its own for the purposes of designing HETs for thermal shock resistance. The heat loads in HETs, the temperatures and temperature gradients produced, and the effect of material choices on thermo-mechanical stress are important to know for design purposes. Thermo-mechanical stresses are also of interest, because they were thought to play a role in potentially modifying the plasma erosion process. The SRH developed in the next chapter predicts ranges of unstable surface waves with a wavelength dependent on the presence of mechanical stress.

This chapter gives an overview of average temperatures observed in thermography studies of kW-class HETs. It gives a section on dimensional analysis of thermo-mechanical problems, and how material properties scale the stresses that are present with a given geometry. A 2D thermo-mechanical model of the T-140 channel wall is created, and used to reproduce the observed temperature profile of the T-140. The model provides predictions for stresses present with an M26 and HP channel wall, for a variety of operating conditions and boundary assumptions. These predictions help bound the stresses that can reasonably be expected for the T-140, which is assumed to be representative of HETs in the same power class.

4.2 Observed Temperatures in HETs

During operation, HETs experience significant thermal loads, leading to thermo-mechanical stresses. During the operation of a HET, the energetic plasma in the thruster interacts with the walls of the channel. Mediated by the plasma sheath, fluxes of ions and electrons provide a heat flux to the wall [38] [39]. This heat flux into the wall is balanced by thermal radiation from the inner surfaces of the channel wall, which cool the thruster, and by (limited, by design) conduction to the thruster body.

Modeling is conducted to obtain estimates for representative thermo-mechanical stresses that are present in HET channel walls during operation. This modeling is informed by prior experimental measurements of HET channel wall temperatures. Mazouffre investigated the SPT-100-ML and the PPSX000 using a MWIR (8-9 μm spectral domain) thermal infrared camera [18]. The average temperatures of the BN-SiO_2 channel walls were well characterized by a power-law relationship, given in Equations (4-1) and (4-2). The discharge power, in W, is given by P. The thruster channel wall temperature is given by T. The range for these relationships is 500 – 3000 W for the SPT-100, 1500-5000 W for the PPSX000 [40]. Temperatures as high as 900 K are attained during 5-kW operation of the PPSX000.

$$T_{SPT100} = 447\ K + (11.1\ K/W^{0.5})P^{0.5} \tag{4-1}$$

$$T_{PPSX000} = 429\ K + (6.8\ K/W^{0.5})P^{0.5} \tag{4-2}$$

Data and infrared images were presented for a 3.2-kW operating condition, showing approximately a 6-10 K difference between the top and bottom of the outside channel wall, and a 60 K difference between the inside and outside channel wall.

Martinez investigated the T-140 HET thermal behavior by placing thermocouples within holes drilled into the channel wall, 1 mm from the plasma facing surface, and in certain other locations within the thruster [41]. The T-140 has an approximately 140 m outer diameter channel, which is composed of grade M26 borosil. Temperature measurements were made at several discharge powers, and a similar power law relationship between maximum channel wall temperature and discharge power was derived. This relationship is shown in Equation (4-3).

$$T_{T140} = 302\ K + (24\ K/W^{0.38})P^{0.38} \tag{4-3}$$

In Martinez's paper, temperature distributions over the channel were presented for the 840 W, 5.1 mg/s run condition. Temperatures were approximately 610 K at the exit plane of the channel, and 574 K near the inlet of the channel. A good model of the thermal physics should be able to reproduce the rough temperature distribution within the channel.

4.3 Dimensional Analysis

Dimensional analysis of thermo-mechanical problems, and analysis of a 1D analytical model, can provide some important generally applicable scaling relationships. For a 1D axisymmetric analytical model, the thermo-mechanical stress present in a hollow cylinder of inner radius r_1, and outer radius r_2 can be given by Equation (4-4), where σ_h is hoop stress, σ_r is radial stress, T_0 is the average temperature of the cylinder, T_r is the temperature gradient across the cylinder in the radial direction, and Q_i, a and b are constants which are complicated functions of the material Young's modulus, Poisson's ratio, and cylinder geometry.

$$\sigma_h(r) = 2Q_1T_r + Q_2a - \frac{Q_3b}{r^2} - cT_0$$
$$\sigma_r(r) = Q_1T_r + Q_2a + \frac{Q_3b}{r^2} - cT_0 \quad (4\text{-}4)$$

In a HET, the largest temperature gradients are along (*z*-direction) the cylinder wall, not across (*r*-direction) the cylinder wall. However, dimensional analysis of thermo-mechanical problems do provide the general scaling relationship given in Equation (4-5). In this expression, the stress at a given point, σ, scales with a nondimensional constant K_g, the material properties, and the temperature difference across the geometry, or a length-scale and temperature gradient. This dimensional analysis assumes linear elasticity of the object in question, and a constant coefficient of thermal expansion (CTE). K_g is a function of the nondimensional problem geometry and Poisson's ratio. The relevant material properties are the Young's modulus E and CTE α. Equation (4-5) tells us that, because of material property differences, we should expect to see a greater thermal stress, by a factor of 10, in channel walls composed of borosil (M and M26) when compared to HP boron nitride.

$$\sigma = K_g E\alpha\nabla(\Delta T)L = K_g E\alpha(T_2 - T_1) \quad (4\text{-}5)$$

4.4 2D Thermo-mechanical Model of T-140 Channel Wall

A 2D axisymmetric thermo-mechanical model is created for the T-140 channel wall. The T-140 channel wall is surrounded by a titanium radiation shield on the inside of the inner face. The channel wall is surrounded by a titanium radiation shield bucket on the outside that loosely supports the inner shield. The channel wall is held to the bucket by pins along the bottom of the channel, and by tension from the stem holding the bottom

of the anode-gas distributor to the bottom of the channel. Thermally insulated boundary conditions are justifiable for the titanium radiations shield, that is in loose mechanical, and thermal contact with the channel, but not very thermally emissive. Thermal emissivity of unfinished titanium is given as 0.31 in. [42]. A value of 0.241 is given by [43]. A thermal insulating gap is present between the upper channel wall and the surrounding magnet material on the inside of the inner wall and outside of the outer wall. Radiative boundary conditions are applied to the inside faces of the channel. The pin support between the channel wall and the thruster implies loose mechanical boundary conditions.

Heat flux to the channel wall is a function of the local plasma density, and the electron temperature. This can be derived from the physics of the plasma sheath for a dielectric discharge channel wall. Positive and negative charge fluxes to a dielectric wall must balance, and so a region of negative potential forms near the wall to repel the lighter and more mobile electrons. The power density to the channel wall can be expressed in terms of the fluxes of electrons and ions to the channel wall times the energy that each carries, given in Equation (4-6). Secondary electrons ejected from the channel walls usually have only 1-2 eV of energy, so they are not directly a large component of the heat-flux to the wall [38]. SEE are more significant to power loading due to their effect on the sheath potential.

$$P_w = \Gamma_e E_e + \Gamma_i E_{total.i} \tag{4-6}$$

Equation (4-6) can be re-expressed (eq. 4-7) in terms of the ion current to the wall, in a form given in Goebel and Katz's analysis in chapter 7 [38]. In the following equations, P_w refers to the heat flux to the channel wall, I_{iw} to the ion current density to

the wall (unit charge times Bohm velocity times plasma density), ε refers to the ion energy (in this case due to the Bohm velocity), ϕ refers to the plasma sheath potential, m_i to the ion mass, m_e to the electron mass, and T_e to the electron temperature.

$$P_w = I_{iw}\left[e^{\frac{e\phi}{kT_e}}\sqrt{\frac{2m_i}{\pi m_e}}\left(\frac{kT_e}{e}\right) + (\varepsilon - \phi)\right] \tag{4-7}$$

Secondary electron emission (SEE) is the emission of electrons from a material stimulated by electron bombardment of the material at a given energy. SEE tends to reduce the magnitude of the plasma sheath potential drop (weaken the plasma sheath), which leads to greater heat fluxes to the channel walls [38]. Hobbs and Wesson state that for a SEE space-charge limited sheath (one with the maximum amount of SEE possible from the wall), the sheath potential is limited to -1.02 kT_e/e, where kT_e/e is the energy due to electron temperature divided by the charge in Volts [39]. For a standard Child-Langmuir sheath, the sheath potential is -5.96 kT_e/e for xenon. For a borosil wall, assuming the SEE model for borosil given in Goebel and Katz, sufficient SEE for the space-charge limited case is present for electron temperatures greater than 30 eV [38]. For 25 eV, the sheath potential is roughly -54 V. For several values of the electron temperature, equation (4-7) reduces to equations (4-8)-(4-10), with the first term in square brackets being the energy flux to the wall due to electrons, and the second being due to ions.

$$\begin{cases} P_w = I_{iw}\left(\frac{kT_e}{e}\right)[1 + 6.47], & T_e < 10\ eV, Xe, BNSiO_2 \quad (4\text{-}8) \\ P_w = I_{iw}\left(\frac{kT_e}{e}\right)[45.02 + 2.61], & T_e = 25\ eV, Xe, BNSiO_2 \quad (4\text{-}9) \\ P_w = I_{iw}\left(\frac{kT_e}{e}\right)[140.76 + 1.52], & T_e > 30eV, Xe, BNSiO_2 \quad (4\text{-}10) \end{cases}$$

These equations show that the most significant heat flux to the wall will occur in the ionization and acceleration regions of the HET, where the plasma density and electron temperatures are high. For typical ion densities of 1×10^{17} particles/m^3, at electron temperatures of approximately 25 eV, heat fluxes on the order of 8 W/cm^2 are expected. Conditions similar to these are present in multi-kW HETs. Martinez calculates a peak heat flux of 10 W/cm^2 for a 2.7 kW operating condition for the T-140 thruster, based on experimental temperature measurements [41]. Katz *et al.* calculate that for a baseline unshielded configuration of a 12.5-kW HET, peak heat-fluxes of 10-15 W/cm^2 are expected [44].

Under varying operating conditions, the heat flux lost to the wall as a percentage of the total discharge power has been found to remain relatively constant in experiments. [40] [41]. For the T-140, average and peak temperatures similar to those reported by Martinez are found if ~25-27% of the discharge power is applied as a heat flux to the ionization/acceleration region of the T-140 thruster channel wall. This proportion of the discharge power reproduces Martinez's temperature curve in both the 2D modeling, and a simple bulk radiative heat balance model [41]. Figure 4.2 shows this comparison. In the thermo-mechanical model, 25% of the discharge power is applied evenly to the 1.5 cm of the channel wall near the exit plane as a heat load.

Figure 4.1 shows the T-140 channel, the surrounding structures, and the boundary conditions used in modeling the channel wall. COMSOL Multiphysics is used to solve the equations for linear thermo-elastic deformation and heat transfer. The solver supplies several default subdivision levels for a base mesh, of which the finest level is used. The resulting mesh has 4799 interior elements and 519 boundary elements. The maximum temperature difference between the solution for the finest mesh refinement at 4799 elements and the next coarsest mesh at 453 elements is 0.12 K.

Material properties used in the simulation are taken from the St. Gobain boron nitride solids material data sheet [45]. An emissivity of 0.9 was used for the ceramic, similar to the value used in [41]. In order to make a conservative estimate for stresses, the maximum Young's modulus, and minimum thermal conductivity were used. A Young's modulus of 94 GPa, a CTE of 1.5 μm/m-K and a thermal conductivity of 11 W/m-K were used for borosil. A Young's modulus of 40 GPa, a CTE of 0.6 μm/m-K , and a thermal conductivity of 27 W/m-K were used for grade HP boron nitride.

Figure 4.3 shows the temperature and hoop stresses for the 840 W operating condition of the T-140 that can be compared to Figure 5 from the T-140 thermography study [41]. In the 840 W condition, for which a distribution is displayed in Figure 5, the maximum (610 K) and minimum (570 K) temperatures are higher, and the temperature gradients are lower than in thermo-mechanical modeling. A combination of more distributed power loading to the wall, power loading to the anode, and higher thermal conductivity can explain these discrepancies. The percentage power loss to the wall is chosen to match the maximum temperatures for operating conditions from 840 to 3400 W, and tends to under-predict temperatures for the 840 W condition, and over-predict

temperatures for the 3400 W condition. The thermo-mechanical model makes conservative estimates of the temperature gradients and therefore hoop stresses for the channel wall.

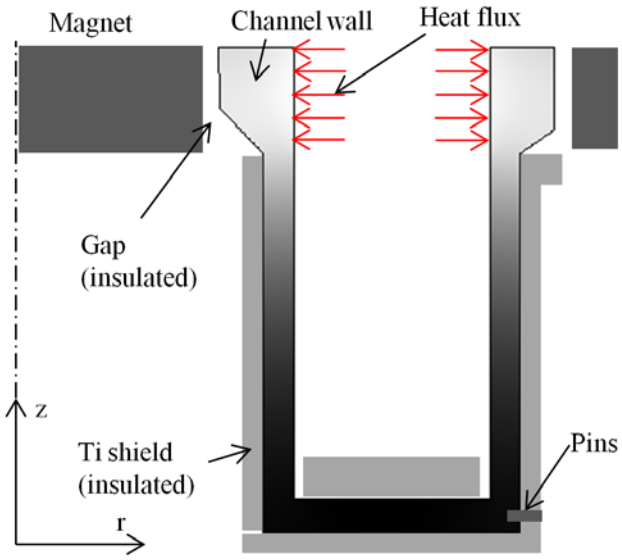

Figure 4.1: Model and boundary conditions for T-140 channel wall.

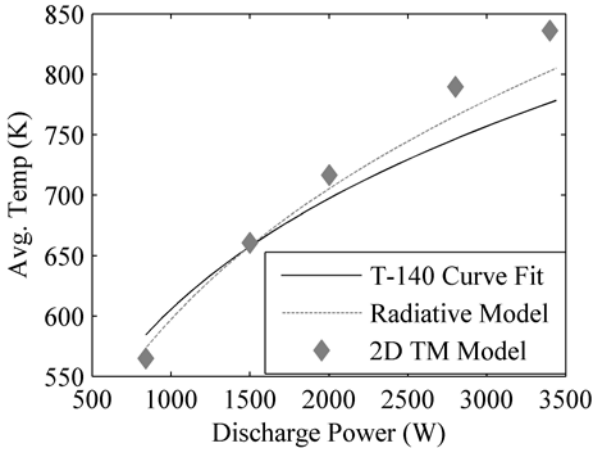

Figure 4.2: Max temperature as a function of discharge power for Martinez's curve fit to experimental temperature data [41], a simple radiative heat-balance model, and the 2D thermo-mechanical modeling.

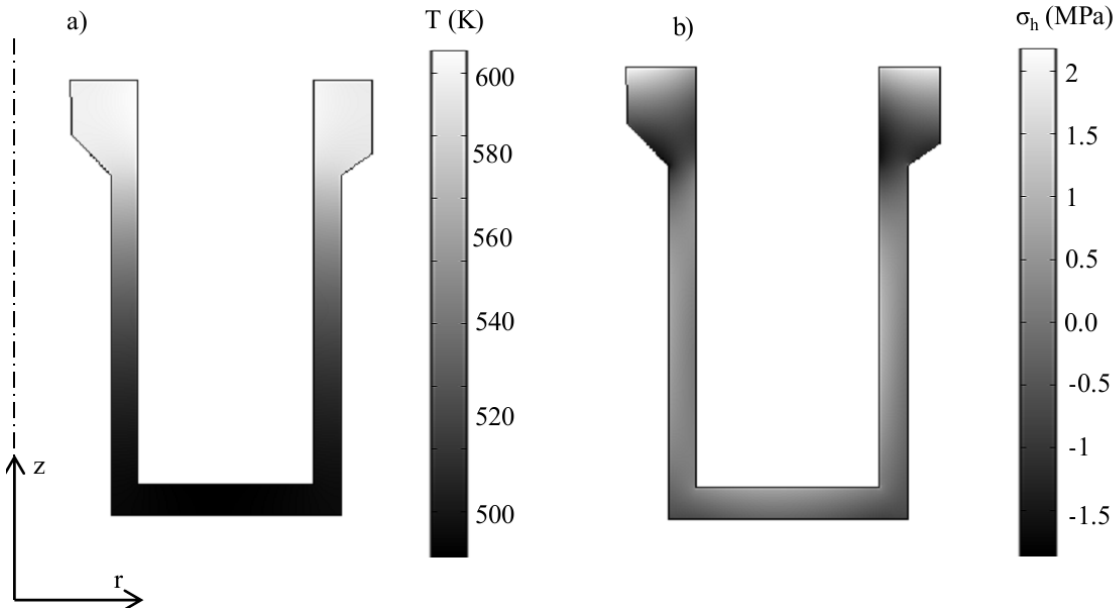

Figure 4.3: Temperature and hoop stress distribution in T-140 channel wall at the 840-W discharge power condition.

Table 4.1 presents the different operating conditions and variations on the material and boundary conditions. The expected ten-fold reduction in stress for using grade HP as a wall material is present. Representative thermo-mechanical stresses for multi-kW HETs are in the 100 kPa to 6 MPa range, according to this modeling. The maximum stress which M26, M, and HP grade BN can withstand is in the range of 20-30 MPa. This is the flexural strength of the material [46]. Any stresses greater than this would lead to cracking of the channel wall.

Table 4.1: Thermal modeling boundary conditions, max temperatures and stresses

Wall Material (grade)	Discharge Power (W)	Outer Thermal BC	Max Temperature (K)	Max Compressive Hoop Stress (MPa)
M26	840	Insulated	605	-1.89
M26	2000	Insulated	779	-3.82
M26	2800	Insulated	862	-4.93
M26	3400	Insulated	913	-5.69
HP	840	Insulated	576	-0.15
HP	3400	Insulated	808	-0.44
M26	840	Radiating	564	-2.06
M26	840	Radiating	873	-6.14
HP	840	Insulated	576	-0.15
HP	1500	Insulated	674	-0.26
HP	2000	Insulated	732	-0.33
HP	2400	Insulated	807	-0.44
HP	3400	Insulated	855	-0.52

4.5 Summary

The work given in this chapter discusses the physics of heat deposition in dielectric HET channel walls. It discusses dimensional analysis from analytical thermo-mechanical models, and the scaling relations between temperature gradients, material

properties, and thermo-mechanical stresses. Two-dimensional modeling of the T-140 was conducted using boundary conditions suggested by the construction of the device, general HET plasma conditions, and experimental temperature measurements collected in work by Martinez. The model leads to expectations of thermal stresses on the order of 100 kPa to 6 MPa. For physical reasons, stresses greater than 30 MPa are not expected during normal operation of a well-designed HET. If stresses greater than 30 MPa are present, failure of the channel wall should result for boron nitride and borosil materials. One hypothesis, discussed extensively in the next chapter, proposes that the plasma erosion process should be sensitive to the local strain energy density, and therefore the average thermo-mechanical hoop stress, present in HETs.

CHAPTER 5

ANALYSIS OF STRAIN RELIEF HYPOTHESIS

5.1. Overview of Strain Relief Hypothesis

A hypothesis is proposed that had the potential to explain the formation of the anomalous erosion ridges. The hypothesis is explained in the section below. The analytical content of the hypothesis is derived in section 5.2. Material property inputs are derived in section 5.3. Quantitative estimates for the hypothesis based on reasonable ranges of material property values and thermo-mechanical stress are given in section 5.4 and 5.5. Chapter 5.5 also discusses some of the quantitative problems with the hypothesis, as it relates to plasma erosion. An experiment, proposed in part to test this hypothesis, and to detect any other dependence of plasma erosion processes on material stress is described in Chapter 6 and the following chapters.

The proposed hypothesis, called the Strain Relief Hypothesis (SRH), proposes that the ridges are the result of an instability, driven by the release of mechanical strain energy in the channel wall material and damped by the free surface energy of the material. This hypothesis is inspired by an analytical model provided by Kim, Hurtado, and Tan. Kim studied the surface geometry of thin aluminum samples under mechanical loads sufficient to cause plastic deformation, while the surfaces evolved during an acid etching process [47].

Kim presents an analytical model, based on the concentration of strain energy due to a two-dimensional variational stress field on the surface. These stress variations are

produced by small variations in the surface height. Kim assumed that the rate of evolution of the surface was proportional to the interface energy, and derived that the variation about the average surface profile would evolve according to Equation (5-1). In this equation h represents the small variation to the average surface height profile. M is a kinetic constant for the reaction. Δw is a variation in the surface energy at a given position, resulting from the variation in the surface height. γ is the free surface energy.

$$\frac{\partial h}{\partial t} = M\{\gamma \nabla^2 h + \Delta w\} \tag{5-1}$$

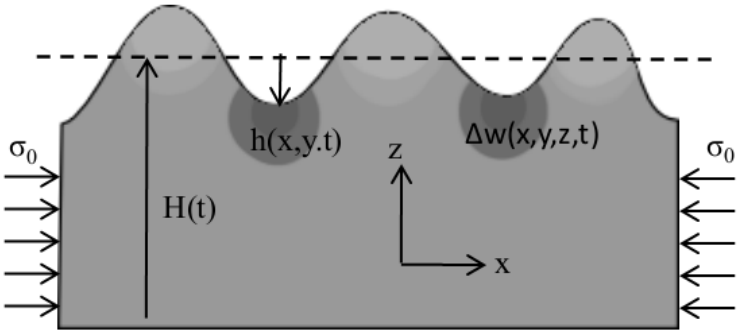

Figure 5.1: Cross section of problem domain.

Kim took the Fourier transform of a Green's function expression for the surface strain energy variation, and produced Equation (5-2) for the evolution of a given wave-mode as a function of the stress state and wavelength. This function, referred to throughout the proposal as the amplification function gives a nondimensional measure of the growth or damping of a given wave-number. The amplification function, denoted Ψ, is a difference between the logarithmic power spectra of the variational surface height profiles at two different times. M is again the kinetic constant of the reaction. $\hat{h}$ is the

fourier transformed height profile. $A(\boldsymbol{\sigma}, \boldsymbol{n})$ is a quadratic function of the surface stress and the normal vector to the component wave. ω is the absolute wavenumber.

$$\Psi(\omega; \boldsymbol{\sigma}; t) = \mathrm{k} * \log_{10}\left(\frac{\hat{h}(\omega, t)}{\hat{h}(\omega, 0)}\right) = -M(t) * (\gamma\omega^2 - A(\boldsymbol{\sigma}, \boldsymbol{n})\omega) \tag{5-2}$$

$$A(\sigma, n) = \frac{\left((1-\upsilon) * t_n^2 + t_s^2\right)}{\mu} \tag{5-3}$$

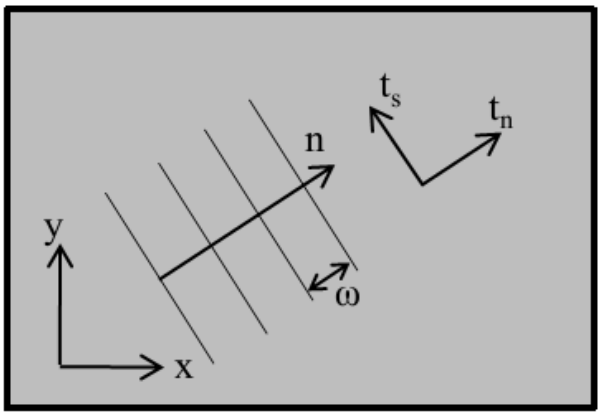

Figure 5.2: X-Z diagram showing surface wave-mode variables

Equations (5-2) and (5-3) for Ψ predict an unstable range of wavenumbers between the zero angular frequency origin, and a critical wavenumber above which features are damped over time. Above the critical wavenumber, the free surface energy cost of creating new features is higher than the relieved strain energy. In the case of uniaxial stress, the critical wavenumber is given in Equation (5-4).

$$\omega_{cr} = \frac{(1-\upsilon)\sigma_p^2}{\mu\gamma} \tag{5-4}$$

Kim's work considers acid etching of aluminum samples under loads of 200 - 230 MPa in several configurations, and found critical wavenumbers on the order of 10 rad/μm. While Kim's work focuses on acid etching of aluminum, there is no dependence in this theory tying the physical process of erosion to acid etching. It was proposed that a similar process may be driving the formation of the periodic anomalous erosion ridges in HETs. In the proposed process, ions bombard the surface of a material and do the work of sputtering atoms off the surface. The presence of strain energy due to thermal stresses present in the thruster could drive increased sputtering from local regions of high strain energy on the surface. The free surface energy imposes a cost to this process, leading to generalized forces that cause the features below a critical wavenumber to grow, and other features above this wavenumber to damp out.

In order to use Equation (5-4) to predict the range of unstable wavelengths, certain material properties, as well as the thermo-mechanical stress state in the material needs to be known. Estimations for the thermo-mechanical stress present in HETs can be derived from the thermo-mechanical modeling in Chapter 4. Elastic moduli can be found from material property sheets, or through compression testing of samples. Estimates for the free surface energy are made in section 5.3.

In order to estimate how fast this process occurs, the energy required to sputter material must be compared with the strain energy densities that will be present in the material. An estimate of the kinetic constant for this process, and the implications for this hypothesis, are discussed in section 5.5.

5.2. Independent Analytical Derivation of Strain-Wavelength Relationship

The Kim paper provides only an overview of the derivation of the Δw strain energy variation function. In order to confirm and make explicit the derivation of the analytical theory behind the strain relief hypothesis, Δw, and the critical wavelength expression, are independently derived in this section. If an infinite half-space material domain is assumed, under a constant zeroth-order stress state, the result of a small sinusoidal variation to the surface height can be modeled as the imposition of a body force of a certain form. This body force is notionally the result of unbalanced forces resulting from the varying surface height and the constant zero-order stress field. This gives rise to first order variational displacement, strain, stress, and strain energy fields. Figure 5.3 shows the problem domain.

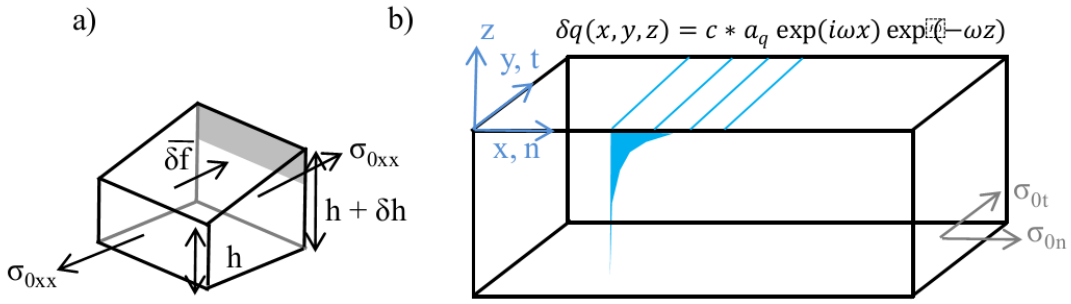

Figure 5.3: a) Origin of unbalanced force, b) Problem domain diagram.

Infinitesimal sinusoidal variations in surface height give rise to a two-dimensional force density which is not balanced by the zero-order stress. The two dimensional force density is given by Equation (5-5).

$$\overline{\delta f_j} = \sigma_{0xj} * \frac{dh(x)}{dx} = \sigma_{0xj}\left(\frac{d}{dx}\left(a_h exp(i\omega x)\right)\right) \tag{5-5}$$

The two dimensional force density is manifested in the 3D problem domain as a body force density that has some dependence on *z*. Over some length-scale below the surface, all variational quantities must decay to zero, yielding the unperturbed solution. Because the only natural length-scale in the problem is the wavelength of the surface wave, the decay length-scale is assumed to be proportional to this, differing by at most some small proportion *c*. The assumed forms of these variations are given in Equation (5-6). δq is the variation quantity, a_q is an amplitude that will eventually be related back to a_h, σ_0, material properties, and ω.

$$\delta q(x, y, z) = a_q \exp(i\omega x) \exp(-c\omega z) \tag{5-6}$$

The stress field is related to the applied body forces within the domain by the conditions for static equilibrium in Equations (5-7) and (5-8). In a homogenous isotropic material, the stress is related to strain by the constitutive equations given in Equations (5-9)-(5-11). The displacements are related to strain by the Equations (5-12)-(5-14). Substituting Equations (5-12)-(5-14) into Equations (5-9)-(5-11), and then that into Equations (5-7) and (5-8) produces a system of equations that give displacement amplitudes in terms of the applied force: Equations (5-15) and (5-16). These can be solved for the displacement amplitude in terms of the stress, wavelength, and height.

$$\begin{cases} \dfrac{\partial \delta\sigma_{xx}}{\partial x} + \dfrac{\partial \delta\sigma_{xy}}{\partial y} = \delta f_x = \sigma_{0_{xx}} a_h * ic\omega^2 exp(i\omega x)\exp(\omega z) & (5\text{-}7) \\ \dfrac{\partial \delta\sigma_{xy}}{\partial x} + \dfrac{\partial \delta\sigma_{yy}}{\partial y} = \delta f_y = \sigma_{0_{xy}} a_h * ic\omega^2 * exp(i\omega x)\exp(\omega z) & (5\text{-}8) \end{cases}$$

$$\begin{cases} \delta\sigma_{xx} = (\lambda + 2\mu)\delta\varepsilon_{xx} & (5\text{-}9) \\ \delta\sigma_{xy} = 2\mu\delta\varepsilon_{xy} & (5\text{-}10) \\ \delta\sigma_{yy} = 2\mu\delta\varepsilon_{xy} & (5\text{-}11) \end{cases}$$

$$\begin{cases} \delta\varepsilon_{xx} = \dfrac{\partial u}{\partial x} = ia_u \omega exp(i\omega x)\exp(-c\omega z) & (5\text{-}12) \\ \delta\varepsilon_{xy} = \dfrac{1}{2}\left(\dfrac{\partial u}{\partial y} + \dfrac{\partial v}{\partial x}\right) = \dfrac{1}{2} ia_v \omega exp(i\omega x)\exp(-c\omega z) & (5\text{-}13) \\ \delta\varepsilon_{yy} = 0 & (5\text{-}14) \end{cases}$$

$$\begin{cases} (\lambda + 2\mu)a_u(-\omega^2)\exp(\dots) = \delta f_x = \sigma_{0_{xx}}\omega^2 a_h ci * \exp(\dots) & (5\text{-}15) \\ (\mu)a_v(-\omega^2)\exp(\dots) = \delta f_y = \sigma_{0_{xy}}\omega^2 a_h ci * \exp(\dots) & (5\text{-}16) \end{cases}$$

Using the definition of the strain energy density for linearly elastic materials, given in Equation (5-1) and (5-18), and identifying $\sigma_{0_{xx}}$ and $\sigma_{0_{xy}}$ with t_n and t_s in Kim's expression for $A(\sigma, n)$, an expression very similar to the one derived in Equation (5-3) can be found.

$$\Delta w = \frac{1}{2}\sigma_{ij}\varepsilon_{ij} = \sigma_{0ij}\delta\varepsilon_{ij} \quad (5\text{-}17)$$

$$\Delta w = \left(\frac{\omega t_n^2 c a_h}{(\lambda + 2\mu)} + \frac{2 * \omega t_s^2 c a_h}{(2\mu)} \right) = \frac{\omega c a_h}{\mu} (t_n^2 (1 - 2\upsilon) + t_s^2) \tag{5-18}$$

This expression for the strain energy variation yields, along with Equation (5-2), the following expression for the critical wavenumber for the case of uniaxial compression. Equation (5-19), with the exception of a minor scale factor, matches Equation (5-4) almost exactly.

$$\omega_{cr} = \frac{c(1 - 2\upsilon)\sigma_p^2}{\mu\gamma} \tag{5-19}$$

The analytical content of Kim's paper is derived as shown above, to explicitly show the origin and assumptions of the analytical strain relief theory and critical wavenumber prediction. Now that the theory has been derived, the constants and inputs to the problem must be defined.

5.3. Estimation of Boron Nitride Free Surface Energy

In order to make use of Equation (5-4) to make predictions about the relationship between stress and the range of unstable wavenumbers, it is necessary to know several material properties, among them the free surface energy of the material being eroded. Data for the free surface energy of boron nitride has not been found in a literature search, though values for similar materials have been. The free surface energy is estimated using

several methods given below. These estimates are intended to give the rough order of magnitude, and are used in numerical predictions throughout the dissertation.

The free surface energy of glass has been measured to be between 3.5 and 5.3 J/m^2 [48]. Boron nitride ceramics, being solid materials, will at room temperature have free surface energies greater than the known free surface energies of liquids such as water. Liquid free surface energy is related to surface tension. This provides a lower bound for reasonable estimates. Water has a free surface energy given as 0.07 J/m^2 at 0 ºC. Silicon nitride/boron nitride composite, another solid ceramic material, though not one used in HETs, has a fracture energy of around 40 J/m^2 [49].

The literature does not appear to contain data on boron nitride or borosil fracture or free surface energies. Two means of estimating the free surface energy of boron nitride are used.

The first method uses information about the covalent bond energy of B-N bonds. B-N bonds have an energy of 90.43 kcal/mol (6.28×10^{-19} J/bond, or 3.9 eV/bond) [50]. The number density of boron and nitrogen atoms in boron nitride is 9.70×10^{28} $\#/m^3$, based on the reported density (2 g/cm^3) [45]. Assuming that the crystalline phase of BN is a hexagonal crystal (h-BN), an arbitrary plane will break at least one bond for every nitrogen atom within a length-scale of $\frac{\sqrt{3}}{2}a$, where a is the BN bond length of 1.5 Å. Other plane orientations will break more of these bonds. The number of bonds broken is within 1 to 4 times the quantity given in Equation (5-20). In this Equation, C is a small integer constant between 1 and 4, n_N is the number density of nitrogen, E_{bond} is the

covalent bond energy, and γ is the free surface energy. Estimates between 5.6 J/m^2 and 22.4 J/m^2 for the free surface energy are given by this method.

$$\gamma = Cn_N * E_{bond} \frac{\sqrt{3}}{2} a \tag{5-20}$$

The second method for producing an estimate of the free surface energy of BN is to use the surface binding energies used in sputtering yield simulations for BN ceramics. In the Cheng thesis, Stopping Range of Ions in Matter (SRIM) was used to simulate the sputtering yield of boron nitride composites as a function of the ion incidence energy. The values entered into the SRIM/TRIM code were chosen to fit the resulting yield curve to experimental sputtering yield data at higher energies. Values between 3 eV and 8.1 eV were used for the surface binding energy of B and N [10]. These surface binding energies can be converted to an energy cost to remove atoms from the surface, which should be related to the free surface energy. The energies produced by this method are between 10 and 28 J/m^2. In Equation (5-21), n is the number density of atoms, E_{SBE} is the surface binding energy.

$$\gamma = n^{2/3} E_{SBE} \tag{5-21}$$

Kim used a value of 0.1 J/m^2 for the free surface energy of the nitric acid/aluminum interface when he performed the modeling work that the instability calculation is based on [47].

In summary, reasonable values for the free surface energy of BN are found to be between 6 and 28 J/m^2, which are within an order of magnitude of the free surface energies for other comparable materials, such as glass and SiN composites. The chemical

etching interface energy used in Kim's work is an order of magnitude smaller. All of these values are tabulated in Table 5.1.

Table 5.1: Free surface energy estimates and empirical data for several material-medium interfaces

Physical Situation	Material	Surface Energy (J/m^2)
Free Surface Energies of Solids	SiN-BN Composites	40
	Silica	3.5 - 5.3
	BN, estimated, method 1	6 - 22
	BN, estimated, method 2	10 - 28
Chemical Etching Interface	Al - HNO_3 interface	0.1
Surface Tension of Liquids	Water, 0 °C	0.075

With ranges for free surface energy and likely thermo-mechanical stresses for HET channel walls, Kim's analytical model can now be used to make predictions for the range of wavelengths which should grow during erosion.

5.4. Quantitative Estimates of Max-Growth Wavelength as a Function of Stress

In chapter 4, reasonable ranges of values for thermo-mechanical compressive hoop stresses present in HETs are between 100 kPa and 6 MPa. The hoop stress component is the important stress component for generating azimuthal ridges via the hypothesized mechanism. It does not make sense for stresses to be greater than about 30 MPa, the flexural strength limit of boron nitride and borosil materials in a properly designed HET, as that would lead to immediate and random fracture of the channel wall during heating. In the previous sections, values between 6 and 28 J/m^2 are estimated for boron nitride, with values of 3.5 to 5.3 J/m^2 reported for silica. In Chapter 6, material testing of fused silica and borosil materials reveals values of 58.7 ± 2.4 GPa for the elastic modulus of silica, and 22.8 ± 3.1 GPa for M26 grade borosil.

Borosil materials are formed by hot-pressing component BN and SiO_2 powders. Grade M borosil has a Young's modulus that is 12% higher, and a flexural strength that is 26% lower in the direction of pressing, as opposed to the plane normal to pressing [45].

Using the Young's modulus for borosil, the range of values for BN and glass free surface energy, and a 12% variability due to material anisotropy of the elastic modulus, a range of fastest growing wavelengths can be computed This is shown below in Figure 5.4.

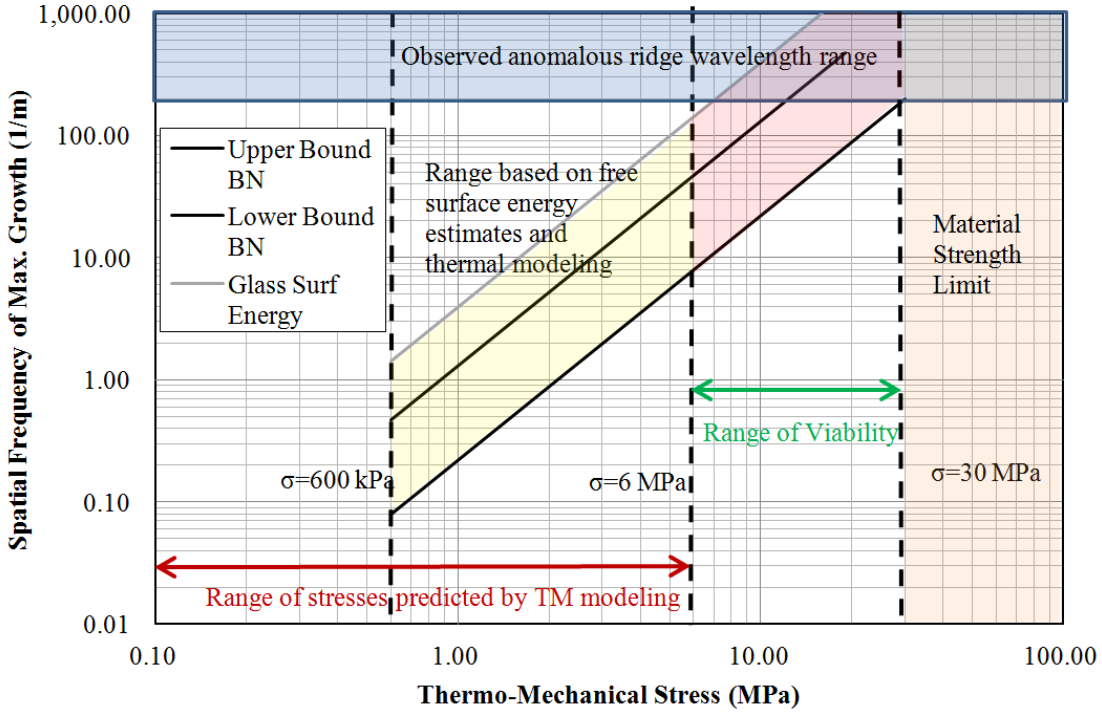

Figure 5.4: Predicted spatial frequency of maximum growth as a function of material stress for borosil material.

Given the published, measured, and estimated mechanical properties of BN and borosil materials, it appears that a relatively large, but not impossible amount of stress would be necessary to match the dominant unstable surface wavelength to the wavelength of the observed erosion ridges. 1 - 5 mm can be achieved, but only for stresses exceeding

10 MPa. However, these values are dependent on the assumptions made for the thermo-mechanical stresses present in the material, and the effective free surface energy of the material under a plasma erosion process (this is thought to be the free surface energy of the bare material in a vacuum).

5.5. Estimate of the Kinetic Constant of the SRH Mechanism

The rate, both in time, and relative to average erosion depth, at which variational surface features grow according to the SRH mechanism is governed by the kinetic constant of the erosion process. This constant, denoted M in Equation (5-1) and (5-2) is tied to the physics of the erosion process. The "generalized forces" derived from the gradients in variational strain and surface energy govern the direction of the process, but the kinetic constant is needed to translate that into a rate of growth.

In Kim's analysis of the acid etching of aluminum, the kinetics of the etching process were assumed to be proportional to the energy at the interface, including the average strain energy present in the material. In the scenario of plasma erosion of a solid ceramic in a vacuum, the material is not undergoing a spontaneous decomposition into a solution. However, the energy present in the material should modify the ease of sputtering atoms from the surface. An estimate of the kinetic constant of the growth process is derived, using physical details relative to the process of ion sputtering.

If it is assumed that variations to the strain energy and free surface energy at each point on the surface modify the energy cost of sputtering atoms from the surface, a similar amplification process to Kim's proportional amplification is obtained. The kinetic constant of the process can be related to the material sputtering yield. This analysis

assumes the sputtering is driven by work done by incoming ions, with a rate proportional to the amount of energy needed to remove each atom. This is dependent on the surface binding energy, closely related to the unmodified sputtering yield; the amount of energy needed to create new surface area (the free surface energy), and the amount of strain energy relieved. An expression for the global change in surface height is given in Equation (5-22).

$$\frac{\partial}{\partial t}\big(H(x,t)\big) = \frac{\partial}{\partial t}(\bar{H}(t) + h(x,t)) = \frac{-E_{ion}I_{ion}}{\big(\alpha + \gamma\nabla^2 h(x,t) - w_0 - \Delta w(x,t)\big)} \quad (5\text{-}22)$$

In this expression, E_{ion} is the average incident energy of the incoming ions. I_{ion} is the flux (#/m^2-s) of incoming ions. α is an energy cost in J/m^3, to remove a given amount of volume from the surface of the material. $\gamma\nabla^2 h(x,t)$ is the amount of free surface energy in the limit of small surface height variations for a given surface configuration. w_0 is the average strain energy present in the material. $\Delta w(x,t)$ is an expression for the variation in the strain energy due to variations in the surface height profile h.

The quantity $E_{ion}I_{ion}/\alpha$ can be related to the unmodified experimental sputtering yield for the underlying material. α can be related to this data for a given yield model, or from the surface binding energies given in the Cheng thesis in the case of boron nitride [10]. Equation (5-23) relates the sputtering yield function Y usually given in units of mm^3/C to the energy cost α.

$$Y(E_{ion},\theta)I_{ion}q = \frac{E_{ion}I_{ion}}{\alpha} \quad (5\text{-}23)$$

The average strain energy w_0 as a function of the Young's modulus *E*, and applied load in the material is given in Equation (5-24).

$$w_0 = \varepsilon_{0_{ij}} * \sigma_{0_{ij}} = \frac{{\sigma_0}_{xx}^2}{E} \tag{5-24}$$

Estimates of the relative sizes of the strain energy w_0 and the sputtering cost α for boron nitride and silica using both Cheng's values for surface binding energy [10], and yield models curve fit to Yalin's directional sputtering data [35] are given below. The stress state assumed is 9 MPa, similar to stresses planned for the proposed experiment in Chapter 6. The assumed ion incidence energy of 120 eV used in the yield models is also taken from values similar to the proposed experiment:

Table 5.2: Relative energy magnitudes for costs of sputtering and strain energy densities.

Property	Method/Situation	Unit	Values
w_0 in HP BN	Uniaxial Stress State: 9 MPa	(J/m^3)	1373 - 1800
w_0 in Silica	Uniaxial Stress State: 9 MPa	(J/m^3)	1380
α, HP BN	Surface Binding Energy	(J/m^3)	4.7×10^{10} - 1.3×10^{11}
α, HP BN	Yield Model, 120 eV	(J/m^3)	7.60×10^{12}
α, Silica	Yield model, 120 eV	(J/m^3)	4.30×10^{12}

Because the magnitudes of the other energy terms are small relative to the sputtering cost, the evolution equation can be approximated by Taylor expansion in these other energy terms. Equation (5-25) shows the linearized evolution equation. The equation can then be split into an equation for the evolution of the average surface height $\bar{H}(t)$ and the variational surface height $h(x,t)$. This is shown in Equations (5-26)-(5-27). Finally, the term $(E_{ion}I_{ion})/\alpha^2$ can be identified with the kinetic constant of the reaction

M in the rate equations. This kinetic constant should govern the rate at which variations to a surface profile will grow in time.

$$\frac{\partial}{\partial t}\left(\bar{H}(t)+h(x,t)\right)=\frac{-E_{ion}I_{ion}}{\alpha^2}\left(\alpha-\gamma\nabla^2h(x,t)+w_0+\Delta w(x,t)\right) \tag{5-25}$$

$$\begin{cases}\dfrac{\partial}{\partial t}\bar{H}(t)=\dfrac{-E_{ion}I_{ion}}{\alpha^2}(\alpha+w_0)=-M(\alpha+w_0) & (5\text{-}26)\\ \dfrac{\partial}{\partial t}h(x,t)=\dfrac{E_{ion}I_{ion}}{\alpha^2}\left(\gamma\nabla^2h(x,t)-\Delta w(x,t)\right)=M(\gamma\nabla^2h(x,t)-\Delta w(x,t)) & (5\text{-}27)\end{cases}$$

For the experiment designed in Chapter 6, an argon plasma source is able to produce ion current densities on the order of 4 mA/cm^2. Using the same values for stress states in the material, incident ion energies, and surface binding energies, values for the kinetic constant M can be estimated. These are tabulated in Table 5.3.

Table 5.3: Estimates for the kinetic constant of growth.

Property	Method	Unit	Values
M, HP BN	Surface Binding Energy	(m/s)/(J/m^3)	2.2×10^{-18} - 2.8×10^{-19}
M, HP BN	Yield Model, 120 eV	(m/s)/(J/m^3)	9.26×10^{-23}
M, Silica	Yield model, 120 eV	(m/s)/(J/m^3)	2.60×10^{-22}

These estimates for the kinetic constant can then be employed to estimate the time constant for the growth of an unstable surface wave. The wavenumber ω_{mg} of the fastest growing surface wave, given in Equation (5-28), is half of the critical wavenumber given by Kim in Equation (5-4). Substituting Equation (5-28) into Equation (5-2) for the amplification function Ψ, a relationship between an exponential time constant for growth

and the kinetic constant is given. Equation (5-29) shows the growth equation for the wave of maximum growth, and Equation (5-30) gives the time constant for this growth process.

$$\omega_{mg} = \frac{(1-\nu)\sigma^2}{2\mu\gamma} \tag{5-28}$$

$$\ln\left(\frac{a_{h\omega}(t)}{a_{h\omega_0}}\right) = \frac{Mt\omega_{mg}(1-\nu)\sigma^2}{2\mu} = \frac{t * M(1-\nu)^2\sigma^4}{4\mu^2\gamma} \tag{5-29}$$

$$\tau = \frac{4\mu^2\gamma}{M(1-\nu)^2\sigma^4} \tag{5-30}$$

Given the assumptions made about the erosion process, and the associated kinetic constants derived from these assumptions, this analysis finds time-constants for wave-growth on the order of 7×10^8 hrs at the smallest to 6×10^{12} hrs. These time constants are very large. They are larger than the timescales achievable in an experiment using available facilities (24 hours). In addition, these time constants are larger than long-duration life testing, or expected operating lives of HETs.

In order for the SRH to explain the observed anomalous erosion ridges, surface waves must grow from seed amplitudes in the roughness of the channel all material to mm in depth. They must grow from the order of 5 μm to mm, roughly 2 to 3 orders of magnitude. Five to seven time constants must pass for this growth to be achieved. Because of this, the time constants for the erosion process cannot be larger than thousands of hours if this hypothesis is to explain the anomalous erosion ridges.

The long time constants produced by this analysis can be explained another way: The amount of energy in the sputtering process can be compared to the energy densities

of mechanical strain energy, thermal energy, and bond energies on a per-atom basis. For pure atomic sputtering, yields are on the order of a few atoms/impacting ion in the ion energy ranges of interest in a HET. Each ion impacts with an energy on the order of 200-400 eV, with a sputtering threshold below which no measurable erosion takes place on the order of 10 eV. Figure 5.5 shows example sputtering yield data in terms of atoms sputtered per ion.

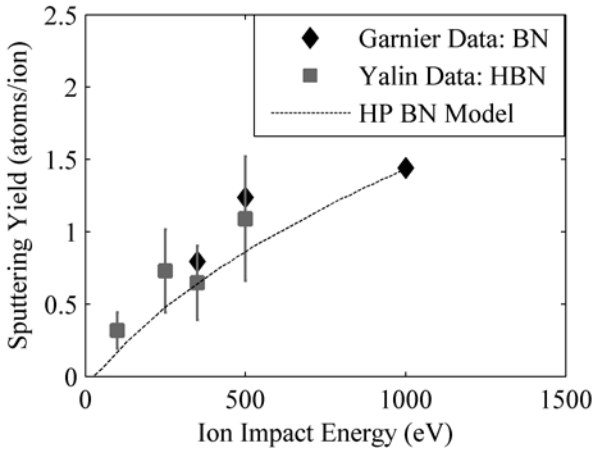

Figure 5.5: Sputtering yield as a function of ion impact energy, in terms of atoms/ion 45º incidence

Boron-nitrogen bond energies are on the order of 3.9 eV. For the material to maintain solid phase, thermal and strain energies must necessarily be much less than this. For grade HP boron nitride, the number density of B and N atoms together is 9.7×10^{28} #/m^3. Given stated values for specific heat capacity [45], at 1000 K, thermal energies of 0.1 eV/atom would be present. There is prior research showing that the atomic sputtering yield of several polycrystalline materials is insensitive to the temperature of the target for that reason [51] [52]. At 45 MPa, the limit of flexural strength for the material, at the elastic modulus stated in the manufacturer's datasheet,

grade M26 BN has an averaged elastic energy of 1.6×10^{-6} eV/atom. This is a brittle bulk material, so fracture is controlled by concentrations of stress at grain boundaries. These relative magnitudes are summarized in Table 5.4. Note that the threshold estimate is based on curve-fitting Garnier's data to Yamamura's model [16]. Yim estimates 13.0 eV [11].

Table 5.4: Relative energies of atomic sputtering and thermo-mechanical energies on a per-atom basis.

Property	Value	Unit
B-N Covalent Bond Energy	3.9	eV/bond
Thermal Energy of HP BN at 1000K	0.1	eV/atom
Average elastic strain energy of HP BN at 45 MPa average load.	1.6×10^{-6}	eV/atom
Threshold energy below which no appreciable atomic sputtering is detectable.	18	eV/ion
Ion energies in HETs	200-400	eV/ion

In summary, using the strain relief hypothesis to explain the observed anomalous erosion ridges has some problems. The time constant for the growth process estimated in this section is much longer than the timescales of long duration life testing, or the operating life of HETs. There are previous experiments varying target temperature that fail to modify the sputtering yield of materials [51] [52]. In addition, average energy density for thermal energy is higher than strain energy density. The range of unstable wavelengths predicted can be made to match the wavelengths of the observed anomalous ridges for stresses from 10 to 30 MPa, which are higher than predicted from thermo-mechanical modeling, but still perhaps physically possible. However, this instability may take a length of time to manifest that does not correspond well to the physics of the

problem, which would be a manifestation of atomic sputtering insensitivity to mechanical strain energy.

Many assumptions went into deriving the range of instability, and the kinetic constant of the SRH process for borosil composites, silica, and boron nitride. Because this is only one possible stress-driven mechanism, and because other features may appear, it is believed that experimentally exploring what, if any, sensitivity the evolution of a surface under plasma erosion has to mechanical stress is still valuable.

The next chapter describes the design of an experiment to test the SRH, and to detect variations to the plasma erosion of stressed materials, compared with unstressed control samples. Pairs of samples are exposed to plasma: One sample of the pair is placed under a uniaxial compressive load and the other is unstressed. The SRH predicts that certain modes in a rough surface will tend to grow under mechanical stress. The SRH does not predict the growth of any surface features in the absence of mechanical stress.

CHAPTER 6

DESIGN OF THE STRESSED EROSION EXPERIMENT

6.1. Overview of Stressed Erosion Experiment

This chapter describes the design of the stressed erosion experiment and the characterization of the chamber, test fixture, and materials. Chapter 7 describes the results of the experiment.

In the previous chapter, the SRH predicts that in the presence of uniaxial mechanical stress, surface features with a range of wavelengths dependent on that stress will grow over time under plasma erosion. The hypothesis predicts instability, but the time-constant of the growth is predicted to be extremely large.

An experiment is designed to detect and characterize features amplified by a plasma erosion process. The experiment is specifically designed to look for changes to plasma erosion due to the presence of mechanical stress and elastic strain energy. It is also designed to make an experimental test of the strain relief hypothesis. The stress range for the experiment (6.0 - 25.0 MPa for silica, 20-24 MPa for borosil) is chosen to be at least as large as the largest anticipated stresses in HET channel walls (6 MPa), up to the maximum load that can be reliably applied to the tested materials without cracking. It is proposed that any modification to the erosion of a material due to thermo-mechanical stress will be more pronounced with greater stress, and that the largest possible stress present in any engineering scenario is necessarily less than that which causes fracture at room temperature.

The experiment is divided into three phases: a pre-exposure phase, exposure phase, and a post-exposure phase. In the pre-exposure phase of the experiment, material samples are profiled using a Tencor P-15 contact profilometer, and imaged using an Olympus LEXT confocal microscope (LEXT). In the exposure phase, material samples are placed under a mechanical load, and eroded with a plasma source. In the post-exposure phase, the samples are profiled again, and imaged with the LEXT. The pre and post-exposure profiles are compared to derive the amplification function Ψ, that provides information about which features (as a function of wavelength/wavenumber) are growing, and which are being damped. In order to claim that a difference is detected between loaded and unloaded samples, statistics derived from pre and post-test line scans (such as Ψ) will have to differ more than the variability in the statistics ($\pm 1\ \sigma$).

Section 6.2 describes the characterization of the plasma produced by the Ion assisted deposition chamber plasma source. Section 6.3 discusses the effects of ion mass and temperature on erosion rates. Section 6.4 discusses the rationale for selecting the materials tested in the stressed erosion experiment. Section 6.5 discusses MTS testing of the elastic modulus of the two test materials. Section 6.6 discusses the design and construction of a test fixture, designed to maintain a compressive load on the stressed samples. Section 6.7 discusses characterization of the spring stack and clamp materials to provide a means of calculating the relaxation of the applied load when the test fixture is heated by plasma exposure. Section 6.8 discusses the test procedure, and analysis of collected data.

6.2. Chamber Characterization

All work for the erosion phase is performed in the Georgia Tech Research Institute (GTRI) Ion Assisted Deposition (IAD) chamber. The IAD chamber is a Leybold APS 1104 deposition chamber. The IAD chamber contains a plasma source capable of operating at a discharge voltage of up to 120 V. The ion current density and ion energy distribution function (IEDF) of the plasma was characterized with Faraday probe and retarding potential analyzer (RPA) measurements. The Faraday probes used for the characterization were 0.865 in. OD circular planar probes surrounded by a 0.938 in. ID cylindrical shield, similar to the JPL Faraday probes in [53]. The RPA is a four-grid RPA with a floating, e-repulsion, ion-repulsion, and e-suppression grid in front of a circular collector [54]. These measurements were conducted at heights of 40 and 60 cm from the floor of the chamber, and at several different axial locations. Table 6.1 presents the plasma source operating conditions for which the source was characterized. Figure 6.1 shows the test fixture positioned over the source in the IAD chamber. Figure 6.2 shows the ion current densities as a function of distance from the source axis for three 40 cm characterizations. For Figure 6.2, several Faraday probe sweeps were taken, and the results were averaged. The standard deviation of the sweeps is roughly 0.04 mA/cm^2, which are too small to be seen in the figure.

RPA measurements of the IEDF for a 140 V bias voltage condition show a distribution of primary ions with a center energy of 130 eV, and a standard deviation of 20 eV. Figure 6.2(b) shows the IEDF. A large population of secondary ions exists. The high energy ions, with energies greater than the ~50 eV threshold energy are responsible for atomic sputtering. Integrating the IEDF/ICDF (ion current distribution function) for

ions with energies of 80 V or more, the fast moving ions account for 68% of the ion current. During the stressed erosion experiment exposures, a bias voltage of 120 V is used to ensure stable long-term operation of the plasma source. This corresponds to condition B. The ion current density profile for condition B shows an axial ion current density of 2.5 mA/cm^2, and a falloff of 2/3 at a radius of 4 cm from the plasma source axis.

The base pressure of the chamber is measured at 2.3x10^{-4} Pa (1.73x10^{-6} Torr) by an integrated Leybold Ionivac, which has an accuracy of 15% and a repeatability of 5% in a pressure range from 10^{-6} to 1 Pa [55]. During operation at 10 sccm gas flow, the chamber reaches a pressure of 1.36 ± 0.077×10^{-2} Pa (1.02x10^{-4} Torr).

Table 6.1: Plasma source operating conditions for faraday probe characterization.

	Cond. A	**Cond. B**	**Cond. C**
Coil Current (A)	2.03	2.03	2.08
Argon Flow (sccm)	10	10	12
Discharge Current (A)	49	50	49.5
Bias Voltage (V)	140	120	140
Discharge Voltage (V)	119	--	120
Discharge Power (kW)	5.86	--	5.79

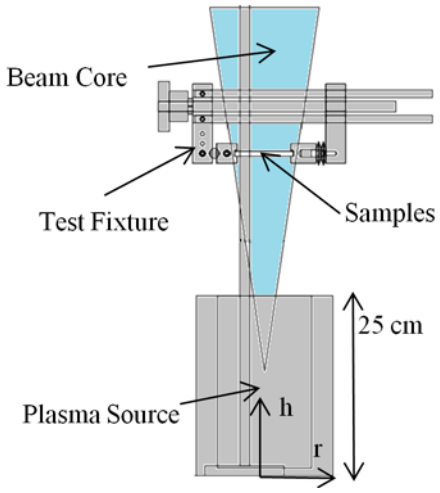

Figure 6.1: Diagram of IAD chamber.

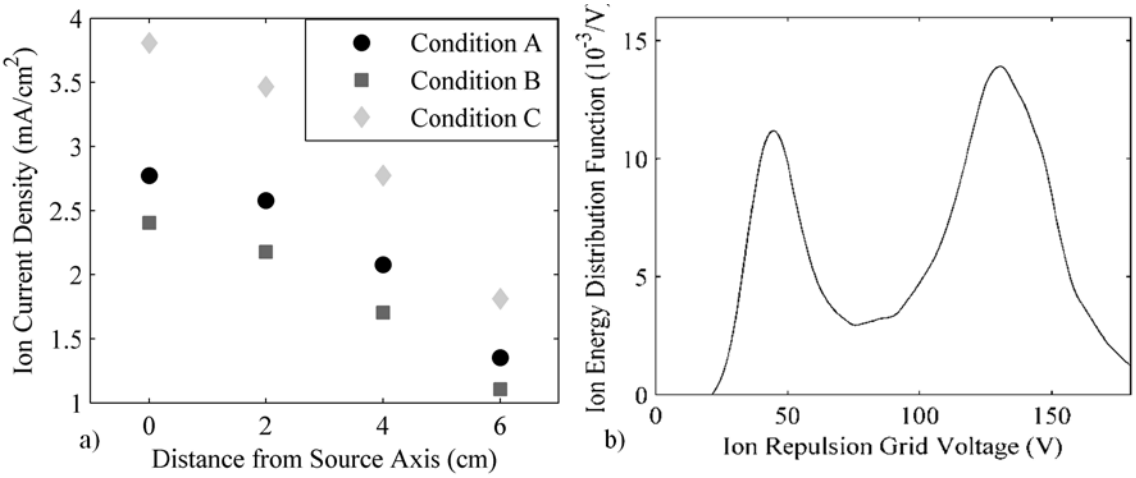

Figure 6.2: a) IAD chamber argon ion current density as a function of axial location, b) IEDF at 140 V bias voltage, 10 sccm operating condition.

6.3. Effects of Ion Mass and Target Material Temperature

In the stressed erosion experiment, the equilibrium temperature that the clamp and samples attain is important primarily in how much relaxation is produced due to the thermal expansion of the clamp screw. Prior research on atomic sputtering by Sigmund

[52] and Rosenberg and Wehner [56], states that the sputtering yield of a target material is insensitive to the material temperature. The stressed erosion experiment uses argon gas instead of xenon, which is commonly used in HETs. However, the sputtering yield for the energies of interest in HET physics (10's-100's of eV) is insensitive to ion mass with the exception of the lightest ions like helium [52] [56]. Experimental data analyzed by Sigmund shows that for energies below 1 keV, there is not a lot of difference between argon, krypton, and xenon sputtering yields of polycrystalline metals such as silver and copper. At high energies of approximately 50 keV, xenon has a factor of two greater sputtering yield (atoms/ion) than argon. Rosenberg and Wehner investigate helium, krypton, and xenon sputtering of a wide variety of target materials at 100, 200, 300, and 600-eV ion energies. The yields for krypton and xenon are similar. This research suggests that using argon, or krypton, in place of xenon should not result in differences in sputtering yield at the energies important to HET physics and erosion. Target atoms are lighter than argon. At most, there should be a factor of two difference between xenon and argon yields for extremely high energies. Table 6.2 shows atomic masses and mass ratios for target neutrals compared with argon and xenon ions.

Table 6.2: Atomic masses and ion/target mass ratios for BN and silica.

Target Atom	Atomic Mass (amu)	Argon/Target	Xenon/Target
Boron	10.8	3.7	12.2
Nitrogen	14.0	2.9	9.4
Silicon	28.0	1.4	4.7
Oxygen	16.0	2.5	8.2
Argon	39.9		
Xenon	131.3		

6.4. Material Selection

Two sets of exposures are conducted for the stressed erosion experiment. For the first set of exposures, fused silica is chosen as the sample material. Technical Glass Products supplies the fused silica samples. Fused silica is chosen to isolate dependence of the sputtering process on the material stress from any microstructural or polycrystalline details inherent in the material itself. Fused silica is micro-structurally isotropic and amorphous. The choice of material is constrained by the small erosion depths attainable in the stable operating time of the plasma source in the chamber. Under the ion current densities and ion energies supplied, within an 11-12 hour exposure, only 10 - 40 μm of erosion depth is expected. Because of this, a material with an amorphous microstructure is needed so that differences in sputtering yield between different materials or crystalline grains do not produce an effect that overwhelms the effects of a stress dependent amplification process.

The second material chosen for the second set of exposures is M26 borosil, a ceramic widely used in HETs, as shown in Table 2.1. M26 borosil is a more complicated material than HP or AX06 boron nitride, in which boron nitride is fused with a boric acid binder, without any other matrix material. It is also more micro-structurally complicated than fused silica. In previous investigations of eroded M26 grade BN-SiO_2, described in Chapter 3, a complicated microstructure was found in cross-sectional SEM images. 0.1x100 μm h-BN flakes are suspended in a silica matrix, with pure silica regions as large as 100 μm on a side [30]. This is depicted in Figure 3.3. M26, and other BN ceramics, are formed by hot-pressing a powder, and the others also have significant heterogeneities and anisotropies in their microstructure. It is known from the work of Garnier [15] [16], as

well as from the work described in Chapter 3, that plasma erosion of these materials forms surface features driven by the heterogeneities in the material. Differences in the sputtering yield of each component lead to the protrusion of the lower sputtering yield BN, which shields the silica behind it, leading to structures that Morozov calls "pike-tongue" structures [17]. In Chapter 3, they are referred to as "cliff and valley" structures. These structures are oriented normal to the ion flow direction in HETs, as opposed to along it, and do not seem to correspond to or develop into the anomalous erosion ridges. For the M26 exposures, the goal is to see if, in a composite material used in HETs, any more complicated mechanisms lead to sensitivity to mechanical stress.

The sample geometry is chosen to be 3x1x0.25 inches. 3-in rectangular samples provide a 60-mm span where > 95% uniaxial loading is expected during sample compression, even for the most conservative assumption of built-in mechanical boundary conditions on the ends. The SRH predicts that simple one-dimensional waves grow when a uniaxial stress state is present in the material. In order to produce a simple situation similar to the azimuthal hoop stress in a HET, such that the SRH will predict the formation of waves, a uniaxial load is applied to the samples. The uniformity of the stress state across the sample is important for the regularity of any stress dependent process that might be detected. Three in samples fit within the 8-cm diameter beam-core of the plume generated by the IAD chamber source. A measure of the degree to which a stress state is a simple uniaxial load, denoted *U*, is defined in Equation (6-31):

$$U = \frac{|\sigma_{11}| - \sqrt{\sigma_{ij\neq 11}^2}}{|\sigma_{11}|} \tag{6-31}$$

ABAQUS finite element analysis simulations yield the stress state in a 3x1x0.25 in. sample. The uniaxiality measure as a function of position along the top center of each sample is plotted in Figure 6.3. A large active region is desirable because long line-scans capture longer wavelength features and provide higher spatial frequency resolution at longer wavelengths. Millimeter to approximately 1 cm scale features are resolvable with the 3-in. samples.

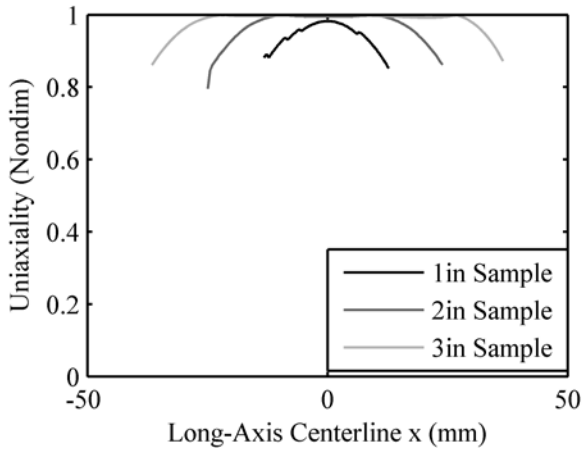

Figure 6.3. Uniaxiality of stress state as a function of top centerline position on 1 in. long, 2 in. long, and 3-in. long samples, with a 0.25 x 1 in. cross section. Percent axial stress.

6.5. Instron Testing of Material Elastic Modulus

The elastic moduli of the materials in question are used to make predictions for the range of unstable wavelengths, as in Figure 5.4. They are also used to measure the load being applied to samples in the test fixture described in the next section. In order to measure the Young's moduli of the fused silica and M26 samples, compression tests are conducted with an Instron 5900 material testing device. An aluminum compression frame is placed in the device. Samples, instrumented with WK-02-062AP/W strain gages from Vishay Micro Measurements, are placed between pads of Teflon tape, centered in the

compression frame. The strain gages have an accuracy of ± 0.1 $\mu\varepsilon$. The strain gages were used to measure axial strain from the center of the sample face. The Instron measured the applied load during a linear compression ramp.

The fused silica samples were 1x1x0.25 in. samples. Technical Glass Products lists a Young's modulus for their material of 72 GPa [57]. From four compression ramps from 0 to 500 lb_f, an experimental value of 58.7 ± 2.4 GPa was obtained for the material. Figure 6.4 shows the four stress versus strain curves for the load ramps.

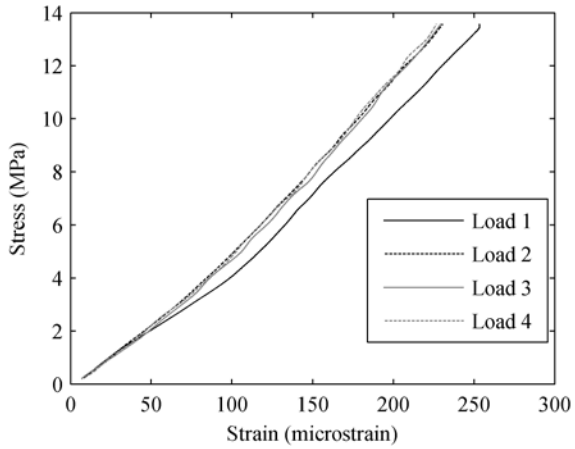

Figure 6.4: Fused silica compression stress as a function of strain.

Two M26 boron nitride samples were tested in a similar manner to the fused silica. Two samples, measuring approximately 1.2x1.2x0.4 inches (exact dimensions measured with calipers) were loaded to 1000 or 2000 lb_f. Borosil is an anisotropic material formed by hot-pressing component powders, with properties varying according to whether they are measured in the plane normal to pressing, or along the pressing direction. The pressing direction of the samples is normal to the large-dimension plane (1.2 x 1.2 in. planes, or 3 x 1 in. planes) for each sample. This is the active surface plane for the experiment. After being loaded several times, the samples were loaded to

destruction to obtain information about when the material would fracture. Sample SD1 failed at 35 MPa. Sample SD2 failed at 37.8 MPa. The failure stresses compare well with the listed perpendicular flexural strengths of grades M and M26 listed in the material data-sheet [45].

By averaging the stress to strain ratio, a Young's modulus for the material of 22.8 ± 3.1 GPa was obtained. In Equation (6-1), $\bar{E}$ is the average Young's modulus. Ranges are one standard deviation of the statistics. σ_i is the stress. ε_i is the strain. Figure 6.5 shows the stress versus strain curves for M26 borosil.

$$\bar{E} = \frac{\sum \frac{\sigma_i}{\varepsilon_i}}{N} \tag{6-1}$$

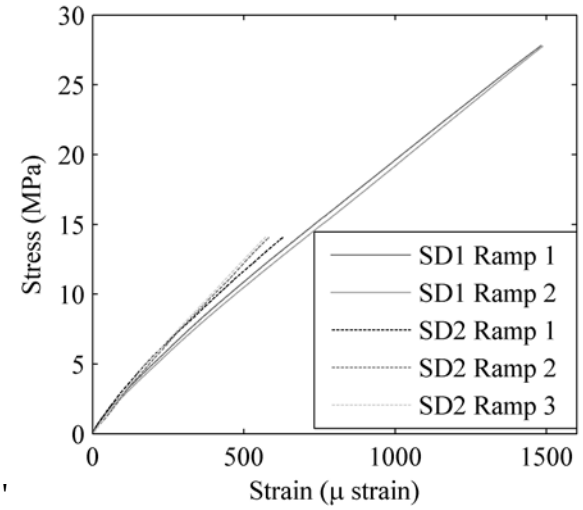

Figure 6.5: Stress as a function of strain for M26 borosil samples.

6.6. Test Fixture Design

A test fixture is designed to apply, in a moment free manner, an even (95% uniaxial) compressive load to the material samples. The test fixture is designed to meet

several requirements: It must maintain an even compressive load on a rigid and brittle material, in a vacuum chamber. It must apply the compressive load without bending moments. It must maintain the load while being heated by exposure to the plasma, with the fixture reaching temperatures as high as 250 ºC.

The test fixture grips are made of 304 stainless steel. A medium carbon steel 1/2"-20 threaded rod tightens the grips, while medium carbon steel guide rods keep the grips aligned. A ball bearing joint on the left grip ensures that compression will be applied to the sample in a moment free manner. Cushions of PTFE tape are applied to the left and right grips to provide a conforming layer between the grips and sample for even loading. The right grip is a plunger that sits on a stack of Belleville springs, or conical disc springs. The springs are intended to maintain the applied mechanical load as the sample and test fixture heat up and thermally expand. The springs apply a load over a much longer travel distance than the thermal expansion (they have less effective rigidity than all other members of the system), and so minor changes in length due to thermal expansion only lead to small reductions in the load applied by the springs. The relaxation is characterized and quantified by experiments described in the next section.

The test fixture is designed to hold two samples beside each other over the plasma source. The grips hold the loaded experiment sample. A sheet metal basket holds an unloaded control sample next to the experiment sample. A thermocouple is attached to the top of the plunger, allowing temperature measurements to be made of the test fixture. A preheater circuit made of two nichrome wire grilles, insulated by Aremco Ceramabond 571-P, is attached to the top and sides of each grip. The preheater circuit is available to warm up the clamp and sample to equilibrium temperatures prior to exposing the sample

to the plasma. Figure 6.6 shows a diagram of the test fixture. Figure 6.7 shows the test fixture and peripheral attachments set up in the IAD chamber.

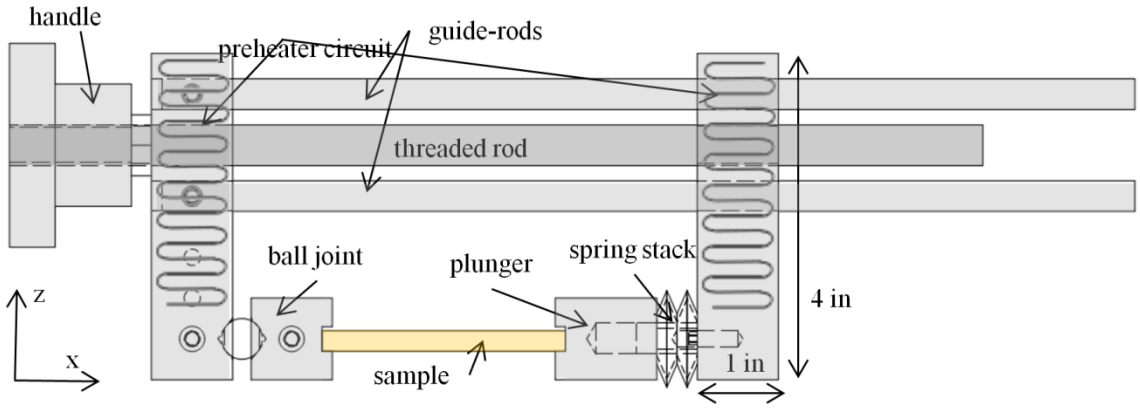

Figure 6.6: Diagram of the test fixture clamp.

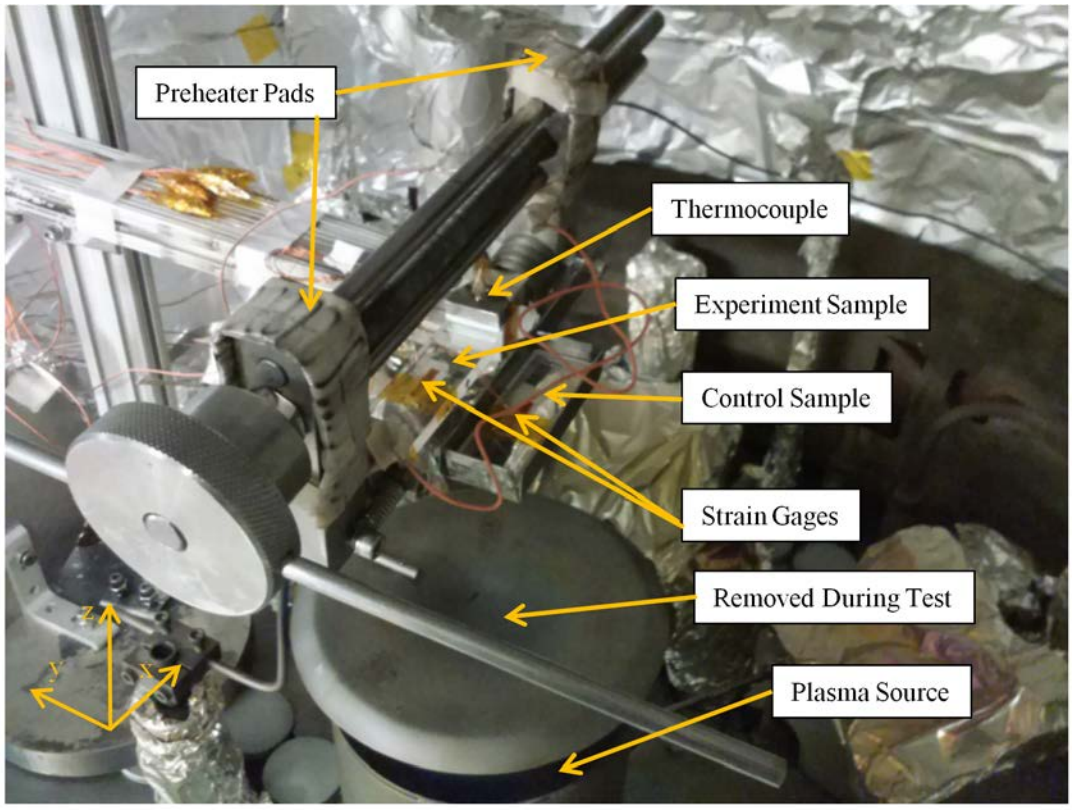

Figure 6.7: Test fixture and instrumentation positioned inside the IAD chamber.

6.7. Characterization of Thermal Relaxation of Applied Load

An initial load is applied to each loaded sample by the test fixture prior to closing the chamber and exposing the sample pair. This load relaxes as the test fixture heats up to an equilibrium temperature of approximately 220 -250 ºC. The screw and metal parts of the clamp thermally expand more than the sample, leading to a net extension of the spring stack. The spring constant of the spring stack is designed to be compliant enough that thermal relaxation is acceptable, while still stiff enough to have a linear range that spans the loads of interest for the experiment.

Direct measurement of the relaxation of the test fixture during preheating and exposure to the plasma was attempted using the strain gages attached to the samples. Even when the strain gages were successfully insulated from the plasma with silicone RTV, the temperature sensitivity of the gages (as high as 6 $\mu\varepsilon$/ºC) was difficult to correct for. In addition, the internal junctions in the stain gages melted at 220 ºC, placing an upper bound at fixture temperature at which the fixture relaxation could be measured. Extrapolation was needed to extend measurements to the equilibrium fixture temperatures obtained during testing.

Direct and indirect measurement of the clamp relaxation are made ex-situ using a Sun Systems EC1A environment chamber, and an Aramis 5M digital image correlation (DIC) system. The DIC system consists of two cameras at a fixed angle on a moveable mount. Only one camera is used for this experiment. The camera observes the deflection and deformation of motion targets which are painted with a high-temperature paint speckle pattern. Four measurements are made with the DIC/oven system shown in Figure 6.8.

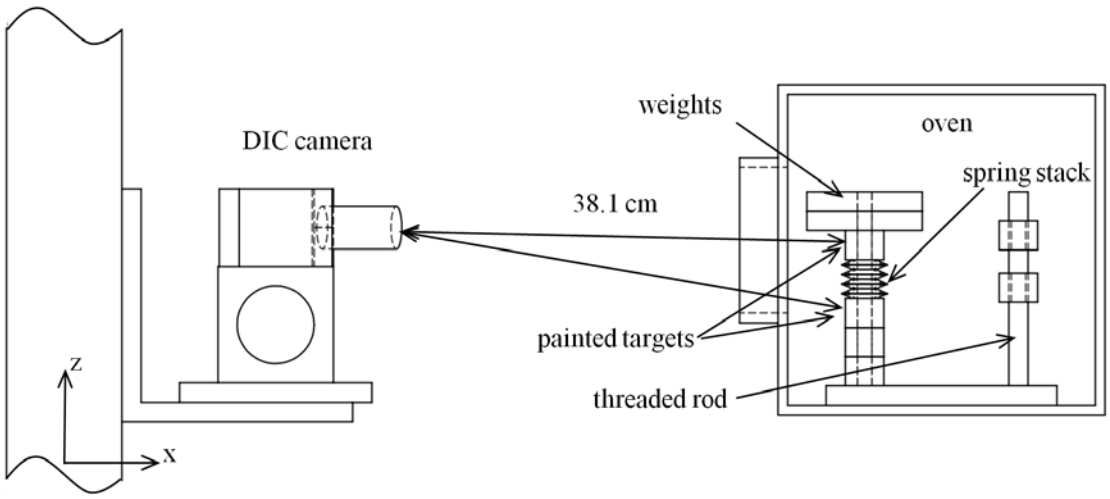

Figure 6.8: Schematic of the DIC test setup.

The first test measures the thermal expansion of the threaded rod used in the clamp. Two painted targets are placed with a distance of 15.0 mm from the bottom edge of the upper target to the top edge of the lower target. The camera is placed at a horizontal distance of 38 cm from the target rod, and both motion targets are in the field of view. The deflection statistics of an approximately 2-mm wide region of the top and bottom motion targets are collected. The difference between the vertical deflections is taken to be the extension of the 15.0-mm region of the threaded rod. The extension as a function of temperature is plotted in Figure 6.9. Deflections at eight temperature set-points are measured. Temperatures in the oven are allowed to equilibrate upon reaching each set-point for 20 minutes. The temperature proportional variability is due to convection cells and density fluctuations in the oven.

The uncertainty bound for the thermal expansion coefficient is found using the expression for the uncertainty of the slope given in Equation (6-2). This uncertainty corresponds to one standard deviation. The thermal expansion of the threaded rod is

measured to be 8.24 ± 0.35 μm/m-ºC. In Equation (6-2), σ_b is the uncertainty of the slope, $\hat{y}_i$ is the linear regression to the data at each x_i, and N is the number of data-points.

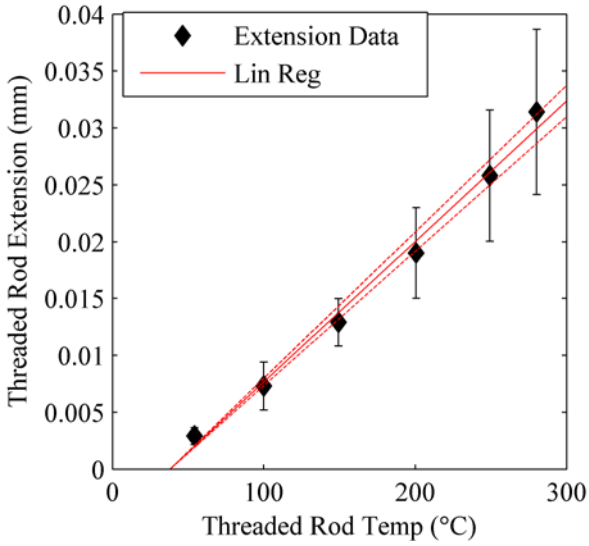

Figure 6.9: Measured threaded rod extension as a function of temperature.

$$\sigma_b = \sqrt{\frac{\sum(y_i - \hat{y}_i)^2}{(N-2)\sum(x_i - \bar{x})^2}} \tag{6-2}$$

The purpose of the second set of measurements is to measure the relative change in stiffness of the spring stack as a function of temperature. For these measurements, a series of light disc springs made of the same material by the same manufacturer, as the springs used in the test fixture, are loaded with weights. Temperature ramps are conducted to measure the extension versus temperature of the light spring stack, $u(T)$. The light spring stack allows the DIC system to resolve larger displacements and provides reasonable uncertainty bounds for the relative stiffness $k(T)/k_0$. Because the springs used in the test fixture are very stiff (1540 - 1600 N/mm), weights are insufficient to provide resolvable differences in extension.

A one-dimensional version of the elastic deformation equations with thermal expansion is given in Equation (6-3).

$$(u - \alpha L \Delta T) = \frac{F}{k(T)} \tag{6-3}$$

The net displacement of the spring is given by u. The load provided by the weight stack is given by F. The coefficient of thermal expansion (CTE) is α. $k(T)$ is the spring constant as a function of temperature. Subtracting the extension values at two different load levels removes the change in extension due to thermal expansion (assuming small deflections relative to the initial height). This leaves only a change in relative extension due to the change in spring constant at each temperature. This is shown in Equation (6-4).

$$k(T) = \frac{F_2 - F_1}{u_2(T) - u_1(T)} \tag{6-4}$$

Figure 6.10 shows an example of the spring displacement as a function of temperature measurement for two different weights.

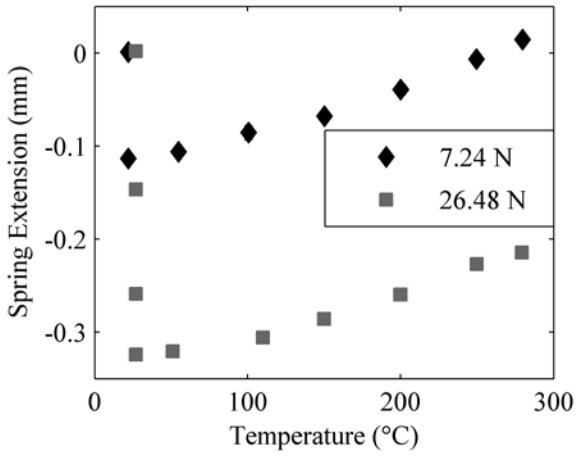

Figure 6.10: Measured spring displacement as a function of temperature

The relative change in stiffness is plotted for two temperature ramp pairs in Figure 6.11. There is good (within 5%) agreement between the measured change in the

spring constant, and the change in tensile modulus for austenitic stainless steels provided by AISI [58]. The springs should lose less than 8% of their stiffness at a temperature of 250 ºC.

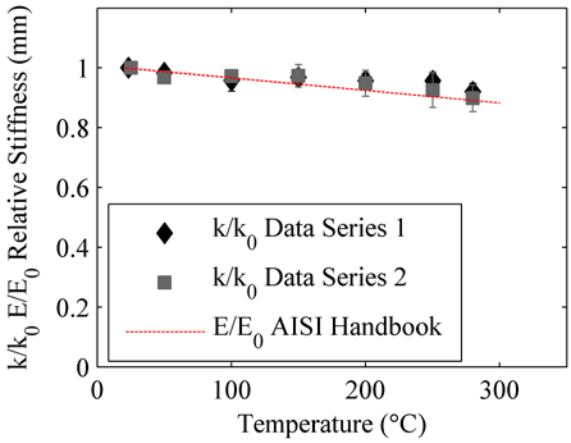

Figure 6.11: Relative spring stiffness as a function of temperature

The relative spring constant stiffness, as a function of temperature, is given by Equation (6-5). A linear model is appropriate over the temperature range of interest. k_0 is the stiffness at room temperature.

$$k(T) = k_0\left(1 - \left(2.714 \pm 0.382 * 10^{-4}\frac{1}{C}\right)\Delta T\right) \tag{6-5}$$

Third, to confirm that the heavy spring stacks used in the test fixture behave in the same way as the light spring stacks, temperature ramps were conducted with the heavy springs at two different load levels. No significant displacement was observable between the two runs. Both temperature ramps provided evidence of the same thermal expansion behavior.

$$u \quad - u_0 = \propto_{rod} L_{rod}\Delta T - \propto_{304SS} * L_{plunger}\Delta T \tag{6-6}$$

Finally, the values for the thermal expansion are used to model the extension of the spring stack on smaller version of the test fixture, which could fit in the oven. A 1"

sample was placed in the grips, and the clamp was tightened three half-turns, corresponding to a 1.9-mm displacement of the spring stack from its neutral position. Three temperature ramps were conducted, and the extension of the spring stack from the tightened position was measured. Figure 6.12 shows the measured displacement and the prediction made with Equation (6-7) given below. A variability of ± 0.07 mm was observed in the clamp behavior and is factored into the uncertainty bounds of the relaxed load calculations.

$$u \quad - u_0 = \propto_{rod} L_{rod} \Delta T - \propto_{304SS*} L_{plunger} \Delta T \tag{6-7}$$

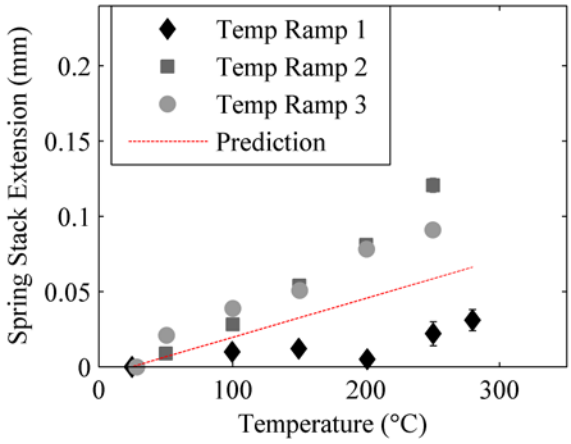

Figure 6.12: Measured spring stack extension and predicted spring stack extension as a function of temperature.

Direct measurements of the room temperature spring constant of the test-fixture spring stack are made using an Instron 5982 material testing system. Two 8x Belleville-disc-spring stacks are placed between 1 in. x 1 in. aluminum beams. The aluminum beams are pressed by the Instron compression grips. Figure 6.13 shows the compression frame for this test.

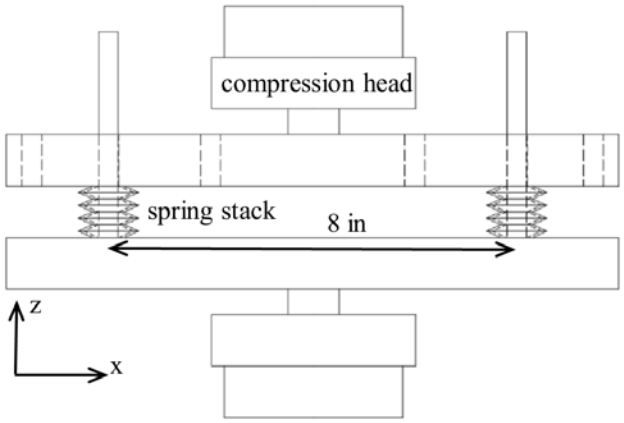

Figure 6.13: Compression frame for RT spring constant measurement

Extension is measured for loads from 0 to 9677 N. The springs behave linearly, after about 1 mm (2413 N per spring stack) of compression. Three load ramps are conducted, measuring an average spring constant of 1597 ± 2 N/mm for each stack. This corresponds well with an earlier measurement made using the test fixture screw to measure spring displacement, and the strain gage on the sample to measure load made *in situ* on the test fixture (1540 ± 63 N/mm).

Using these *ex-situ* measurements, the relaxed load of the test fixture can be calculated as a function of the initial load, and the temperature measured on the test fixture. This calculation takes into account thermal expansion, changes in spring constant, and variability in the clamp behavior. Equation (6-8) shows the calculation for the relaxed load. The force applied by the test fixture is given by F. Temperature is T, and change in temperature from room temperature is ΔT. The initial spring compression is u_0. The length and CTE of the threaded rod is L_{rod}, and α_{rod}. Observed variability in clamp behavior is u_{var}. Table 6.2 presents the values for the constants. Table 7.1 and Table 7.2 present the values calculated for the relaxed load.

$$F(T, u_0) = (k_0)(1 - k_s \Delta T)(u_0 - \alpha_{rod} L_{rod} \Delta T \pm u_{var}) \quad (6\text{-}8)$$

Table 6.3: Variables and ranges for fixture relaxation calculation.

Variable	Value	Unit
k_0	1597 ± 2	N/mm
k_s	2.714 ± 0.382 × 10^{-4}	1/°C
α_{rod}	8.24 ± 0.35	μm/m-°C
L_{rod}	165.1	mm
u_{var}	0.07	mm

6.8. Test Procedure and Analysis

The stressed erosion experiment is conducted in three phases: a pre-exposure phase, an exposure phase, and a post-exposure phase. In the pre-exposure phase, samples are prepared. Baseline profilometry and pre-test microscopy is conducted. In the exposure phase, samples are placed in the test fixture in the IAD chamber, and exposed to the plasma for 11-12 hours. In the post-exposure phase, post-exposure microscopy is conducted on the eroded sample surface. Post-exposure line-scans are made and the resulting statistics are compared with those of the pre-exposure line-scans.

6.8.1. Pre-Exposure Phase

In the pre-exposure phase, samples are prepared and pre-roughened. Each sample is instrumented with a Wk-062AP/W strain gage, manufactured by Vishay Micro Measurements. The strain gages have a resistance of 350 Ω, with a gage factor of 2.01. Each strain gage is placed, centered, on the top surface of each sample, oriented to measure strain along the long axis of the sample.

Each 3x1x0.25 in. sample is prepared by pre-roughening/regularizing the surface. Samples are placed on a stand, and polishing grits of varying fineness are applied to the surface of the sample. A cover-glass plate is passed back and forth over the sample in the direction of the short-axis, until a uniform homogeneous, isotropic surface roughness is obtained. Silicon-carbide (SiC) roughening grit is used to prepare the sample surfaces, to ensure the presence of initial seed roughness and the uniformity of the surfaces. For the fused silica samples, 500 grit, then 320 grit SiC powder is applied in sequence. For the M26 samples, 320 grit, then 500 grit SiC powder is applied to the milled surface of the samples, producing a surface with an initial rms roughness of 1.55±0.10 μm. Two fused silica samples are left smooth to explore the behavior of initially flat (to within ±0.05 μm) samples.

Each sample is placed in the Tencor P-15 contact profilometer, and a series of line-scans is taken at 50 different locations. The locations are measured against the lower-left corner of the exposed side of the sample using the motion stage position indicators. This is done to ensure the same area is profiled in the pre and post-test line-scans. Fifty line-scans are taken starting the center vertically (12700 μm from lower left-hand corner). Each line-scan encompasses the center 50 mm of the sample, of which the center 36.6 mm will be used to compute the amplification function Ψ. The center 36.6 mm is a region in which a 95% uniaxial stress state is expected, given the conservative estimate of built-in boundary conditions. Each line-scan is displaced 20 μm from the previous line-scan vertically, providing representative statistics from a band 1 mm in width. Figure 6.14 depicts the geometry of the scans. Table 6.3 shows the capabilities and settings of the Tencor profilometer.

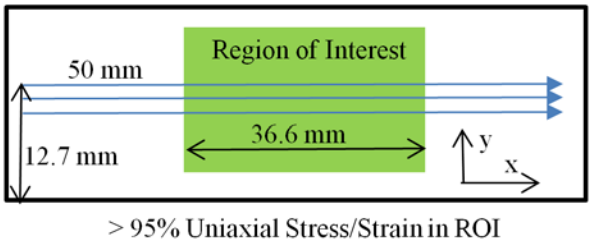

Figure 6.14: Location of line-scans on sample surface.

Table 6.4: Tencor P-15 settings and resolution.

Scan Properties	
X Scan Size (μm)	50000
Scan Speed (μm/s)	200
Sampling Rate (Hz)	500
Applied Stylus Force (mg)	2
Range/Resolution	327 μm / 0.1953 A
Observed Vertical Resolution (range)	0.05 μm

Each sample, prior to being exposed, is imaged with the Olympus LEXT confocal microscope. Visual and laser images, and surface height profiles are taken to compare with the surfaces post-exposure.

Several images are taken, and their location relative to the lower-left reference corner is noted using the motion stage reference of the microscope. The same areas are revisited post-exposure, using the motion stage and the lower left reference corner.

6.8.2. Exposure Phase

In the exposure phase, samples are placed in the test fixture, positioned in the IAD chamber above the plasma source. Two samples are placed side by side in the chamber. One sample, called the loaded sample, or the experiment sample, is placed in the grips of the clamp. PTFE tape is used to cushion the sample in the grips, to allow even application of the load. The second sample is placed 1 in. to the side of the experiment sample in a

sheet metal basket, and is free to thermally expand. The second sample is referred to the control sample, and has no average mechanical stress applied.

Leads to the strain gages are connected to the inner chamber leads via soldered crimp-connectors. The strain gage connectivity is tested, and the degree to which the strain signal wanders is observed over the course of 5-10 minutes. The test fixture is positioned 32-35 cm above the chamber floor, or 8 cm above the plasma source can. The horizontal center of mass of the two samples is centered (to within a few mm) over the plasma source axis with a plumb bob.

Prior attempts at exposure have emphasized the importance of maintaining the cleanliness of the plasma source. In an attempt to minimize unsteady operation of the source, the plasma source is cleaned, and the copper anode tube is bead-blasted prior to each week of testing. The target operating conditions of the plasma source are given below in Table 6.0.

Table 6.0: Plasma source operating conditions.

Parameter	Target operating conditions
Gas 1 Flow (Argon) (sccm)	10
Discharge Current (A)	30
Bias Voltage (V)	120
Discharge Voltage (V)	95
Discharge Power (kW)	2.9

Once the plasma source is prepared, the data acquisition system is started. The Vishay 7000 strain gage DAQ is zeroed and calibrated. A lever bar is inserted into the

clamp screw. The clamp is tightened in ¼-turn or ½-turn increments until the strain gages indicate strain values corresponding to the desired load on the sample.

Once the strain gage reads the target strain, all tools are removed from the chamber, and the chamber is closed and pumped down. Once the chamber has been evacuated to 1×10^{-4} torr-N_2, the plasma source heater, and then the plasma source is turned on. Temperature stabilizes at an equilibrium, indicated in Table 7.1 and Table 7.2 after about half an hour. The samples are exposed for 11-12 hours.

The ion current density in the IAD chamber is measured to be 2.5 mA/cm^2 (at a height of 40 cm above the plasma source, and is expected to be roughly twice this at a height of 32 cm above the plasma source). The center ion energy of the primary ions is 110-120 eV. For argon, this implies an ion density of around $6x10^{15}$ #/m^3. Kilowatt-class HETs, such as the AFRL/UM P5, operate with plasma densities of $1\text{-}4x10^{17}$ #/m^3 [32]. Bohm velocity drift at electron temperatures of 25 eV carries ions into the plasma sheath, and into the channel walls at rates of 6-10 mA/cm^2. Ions are accelerated by the discharge voltage, from 10s of eV, up to 200-300 eV axial kinetic energy at the end of the acceleration zone near the exit plane. Using the Yamamura curve fit to Garnier's yield data for M26 data given in Table 3.2, sputtering yields of 0.0053 mm^3/C (for 120 eV, normal incidence), and 0.043 mm^3/C (for 200 eV and 95 deg. incidence) are found. This leads to estimates of 0.48 μm/hr erosion rates for the IAD chamber, and as high as 10 μm/hr in an operating HET. This implies that in HETs, erosion proceeds roughly 20 times faster than in the IAD chamber due to the denser plasma.

After the exposure is complete, the plasma source is shut off and the chamber is vented. Once the chamber is open, the loaded sample is inspected for any cracks that may

have developed during the exposure. The lever bar is inserted into the clamp, and the load is slowly and evenly released from the sample in ½-turn increments. The samples are retrieved with nitrile-gloved hands, and touching the exposed surface is avoided. Data is collected from the thermocouple DAQ, the Vishay computer, and the IAD chamber APS control computer.

6.8.3. Post Exposure Phase

Post exposure profilometry is taken with the Tencor P-15 profilometer. Profiles are measured from the same lower-left reference corner using the motion stage of the profilometer, in an attempt to acquire profiles from the same region of the sample. Fifty line scans are collected, in the same locations on each sample as during the pre-exposure line-scans. Additional line-scans are collected near the shadowed left and right 1/16 in. of the experiment and control sample. The transition from the shadowed lip of the sample to the region exposed to the plasma provides a sensitive measurement of the total erosion depth produced during the exposure.

Using the lower left corner as a reference, each area imaged pre-exposure is also imaged post-exposure with the Olympus LEXT. In addition, any new features of interest are also imaged for each sample.

6.8.4. Analysis of Mechanical Strain Sensitivity

One of the primary purposes of the stressed erosion experiment is to experimentally test whether or not applied average mechanical stress or mechanical strain energy in a material will produce any variation to the atomic sputtering process. In order

to do this, the pre and post-test tatistics from the surface will be analyzed and compared for both loaded and control samples.

The profilometry data is analyzed in order to derive the amplification function Ψ. Ψ is a nondimensional measure of which Fourier wave-modes are being amplified by the erosion process, and which are being damped (smoothed) out. Ψ is defined experimentally in Equation (6-9), and contains information related to the theoretical expectation given in Equation (5-2).

$$\Psi = \log_{10}\left(\frac{|\widehat{h_t}(\omega)|}{|\widehat{h_0}(\omega)|}\right) \tag{6-9}$$

Each line-scan of a sample provides an independent measurement of $h(x)$. Using software, $h(x)$ is windowed to the middle 36.6 mm region of uniaxial stress. In this region the stress state is expected to be uniform and unchanging to within 5%. In addition, any linear displacement or slope taken during measurement is removed using linear-regression. The FFT of the remaining data is taken or each line-scan. Equation (6-10) shows the discrete Fourier transform (If interpolation between series with different length-scales is desired, this can be turned into a pseudo-CFT by scaling by L/N).

$$\hat{h}(\omega_j) = \sum_{x=x_0}^{x_f} h(x_i)\exp(ix_i\omega_j) \tag{6-10}$$

This yields real and imaginary ($\pi/2$ out of phase) Fourier components for frequencies between $\omega_1 = 2\pi/L$ and $\omega_{N/2} = N\pi/L$. Due to correcting for linear displacements and slopes, ω_0 and ω_1 information is discarded.

The absolute value of each $\hat{h}(\omega_j)$ preserves the magnitude of the Fourier components while discarding the phase information (which is not relevant to the analysis). A series of $\{\{|\hat{h}_t|\}$s and $\{|\hat{h}_o|\}$s are calculated for each of 50 line scans. The average and standard deviation of these sets is calculated for each ω_i and is converted into a mean and error bars for the amplification function Ψ for each sample.

Uncertainty in the amplification function can be estimated from uncertainty in the amplitude of each wave-mode by differentiating. Equation (6-11) shows this relationship. Because the amplification function is a relative process, the uncertainty is proportional to the spread in the height measurements divided by the initial and final wave amplitudes. In practice, the Tencor P-15 has produced a noise floor of about 0.05 μm. Initial and final surface amplitudes have been of about the same order: 0.01 to 0.001 μm for all but the smallest wave-modes, with standard deviations of about half the magnitude. The standard deviation of the mean is the deviation of $\hat{h}$ divided by the square root of the number of line scans. Because of this, uncertainties as high as ± 0.15 for Ψ are present in the measurements. This can be reduced by a further factor of $\sqrt{7}$ for 7-point spatial frequency averaging, for an uncertainty of ± 0.05 (nondimensional).

$$\Psi(\omega;t) \pm \Delta\Psi = \log_{10}\left(\left|\frac{\widehat{h_t}(\omega)}{\widehat{h_0}(\omega)}\right|\right) \pm \left(\left|\frac{\Delta h_t}{h_t}\right| + \left|\frac{\Delta h_0}{h_0}\right|\right) \qquad (6\text{-}11)$$

In order to claim that a difference between the evolution of the surface exists between the loaded and unloaded samples of a given exposure, a difference, greater than the variability/uncertainty in the line-scan data must be apparent. This difference in Ψ must be greater than ± 0.05 at some spatial frequency to claim that a dependence of erosion on mechanical stress has been detected.

CHAPTER 7

STRESSED EROSION EXPERIMENT RESULTS

7.1 Overview

The previous chapter described the design of the stressed erosion experiment. This chapter presents the results of exposure series with fused silica and M26 samples. Two series of samples are exposed and eroded in the IAD chamber. The first series, described in section 7.2, are exposures of the fused silica samples. The fused silica samples have a simple amorphous microstructure, and the final surface produced after erosion is found to be a function of the initial surface roughness. The M26 samples have a complicated composite microstructure described in Chapter 3. The evolution of the M26 samples is found to be governed by the differences in sputtering yield between the different grains within the material. This chapter shows the results of the exposures. Chapter 8 provides discussion of the results.

7.2 Fused Silica Exposures

Four fused silica exposures are conducted. Three of the exposures use pre-roughened samples, with a series of increasing loads applied to the loaded sample. One exposure is conducted with smooth (as manufactured) samples, with surface variations of less than ± 0.05 μm, as measured by the Tencor profilometer. The purpose of the smooth samples is to test the importance of initial surface roughness to the resulting final patterns that develop. Table 7.1 shows a summary of the fused silica exposure loads and operating conditions. The loaded and control sample numbers are given so that data may be

compared with the conditions of each exposure. The equilibrium temperature is the fixture temperature at which the majority of the exposure (after approximately 30 minutes of warm-up time) takes place, measured by the type-K thermocouple on the fixture. The relaxed stress state is the stress in the sample, calculated by Equation (6-8) for the given equilibrium temperature and the initial measured strain. The duration of each exposure, and the z-position of the fixture above the chamber floor (altitude in the table below) is given.

Table 7.1: Exposure overview for fused silica exposures.

Exposure	**Exp. 1**	**Exp. 2**	**Exp. 3**	**Exp. 4**
Loaded Sample	SA7	SA1	SA8	SA6
Control Sample	SA4	SA5	SA9	SA10
Initial Stress State (MPa)	9.6	17.5	18.1	29.1
Equilibrium Temp (C)	288 ± 12	225 ± 8	224 ± 5	243 ± 5
Relaxed Stress State (MPa)	6.00 ± 1.01	14.36 ± 1.01	14.94 ± 0.97	24.99 ± 1.10
Relaxed Stress State (% orig.)	62.5 ± 10.5	82.05 ± 5.79	82.57 ± 5.36	85.87 ±3.79
Duration (hrs)	11	11	11	11
Pre-Roughened	Yes	Yes	No	Yes
Altitude (cm)	31	32	32	32

7.1.1 Amplification Functions

Exposures 1, 2, and 4 yield consistent results for the amplification functions. Pre-roughening of the sample surface ensures that enough initial surface structure is present to avoid problems with source dirt and uneven operation encountered in previous iterations of the experiment. Exposure 1 produced erosion depths of 30-50 μm into the sample surface. Exposure 2 produced erosion depths of 20-40 μm. Exposure 4 produced 30-40 μm erosion depths.

Figure 7.1 shows the amplification functions derived from the line-scans for exposures 1, 2, and 4. Each amplification function is a comparison between averages of 50 initial and final Fourier transformed line-scans. The standard deviation of the mean is approximately the width of the noise in the data. The amplification functions show a range of growth in the surface features, for wavelengths greater than approximately 0.1 mm (wavenumbers less than 10 mm^{-1}). The pattern is consistent between the sample pairs. Between each exposure there is a difference in Ψ of 0.05 (nondimensional) or less, probably linked to the differences in erosion depth and the development of the surface. No difference is apparent in the evolution of the control sample compared with the corresponding loaded sample for any of the three exposures.

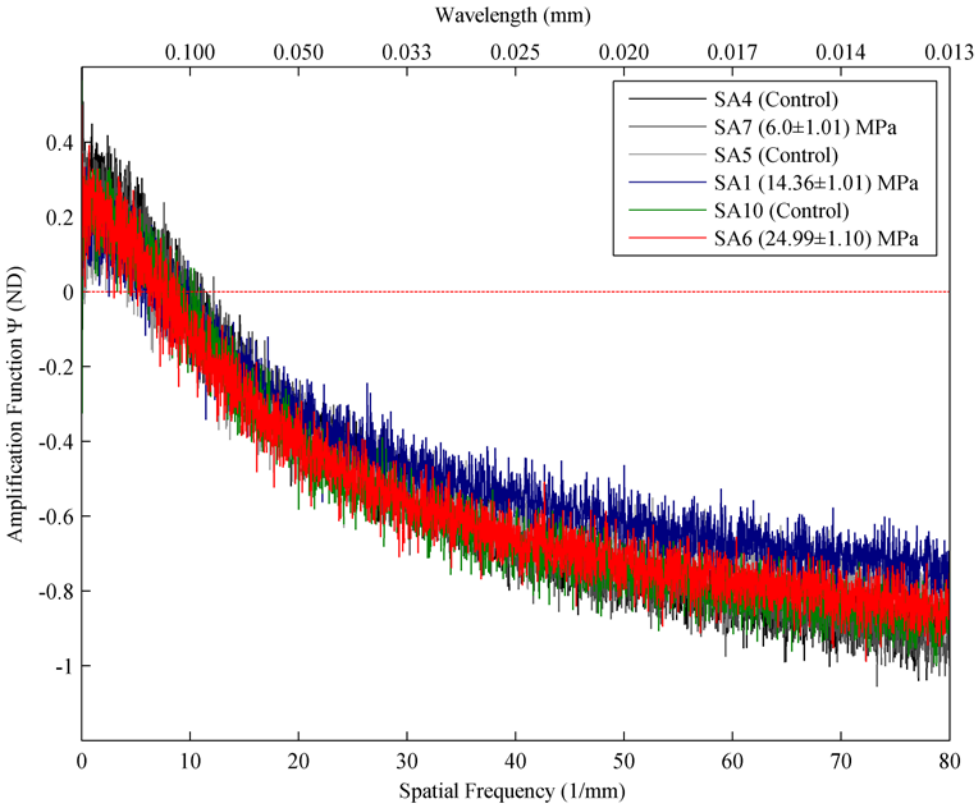

Figure 7.1: Amplification function Ψ as a function of spatial frequency for exposures 1, 2, and 4. Ψ compares post-exposure to pre-exposure surface statistics. Ψ>0 implies features are growing at that spatial frequency.

In order to better show the closeness of the match between amplification functions, Figure 7.2 shows 7-point spatial frequency averages of the data to reduce the noise. Each pair of curves corresponding to a sample pair (SA10, and SA6 for example) lie almost exactly on top of each other (less than the variability of 0.025). Between the sample pairs, there is a variation of between 0.1 and 0.05 in the value of Ψ.

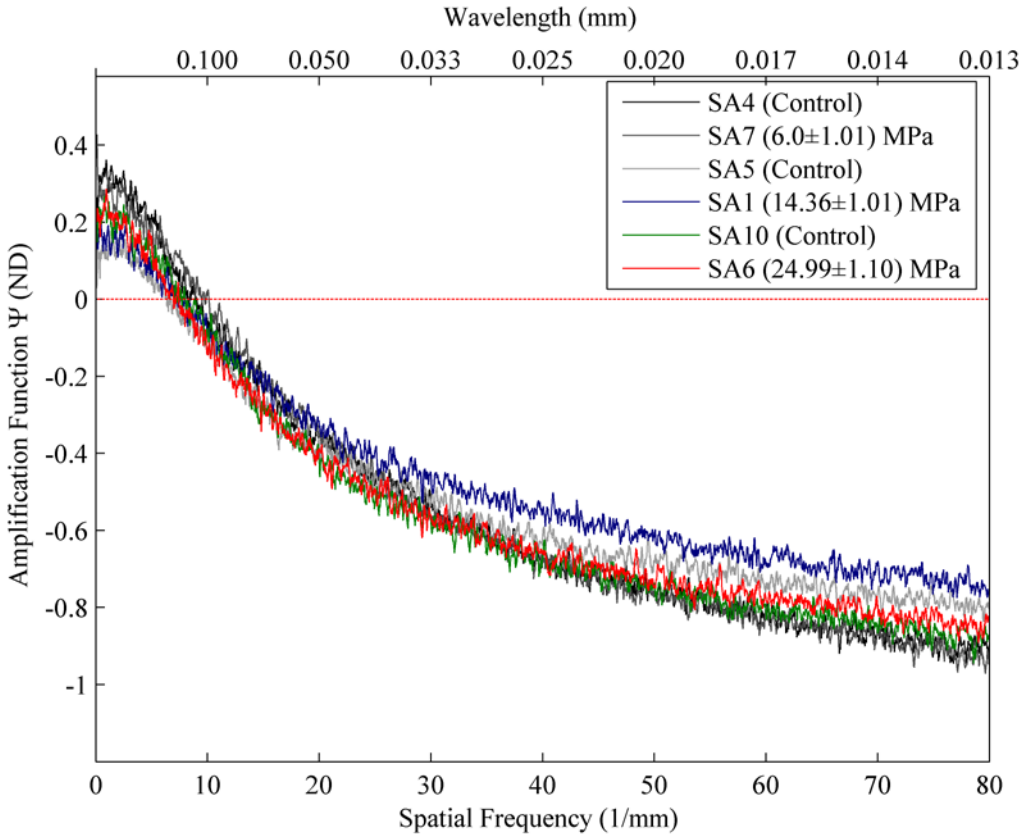

Figure 7.2: Amplification function (with 7-point spatial frequency average) as a function of spatial frequency. *Ψ* compares post-exposure to pre-exposure surface statistics. *Ψ*>0 implies features are growing at that spatial frequency.

For the first sample pair, there were slight differences in the pre-test roughening of SA4, compared to the rest of the samples. The initial surface roughness statistics were greater at higher frequencies for SA4 (due to differences in polishing grit sequence). However, the way in which the plasma erosion process amplified the initial surface features is the same (the difference between the logarithm of the power spectra is the same) for SA4 and SA7 (and the rest of the pre versus post-test statistics). This is shown in Figure 7.3. This demonstrates that the development of surface features is a growth, or amplification, process that develops final surface features from initial surface features.

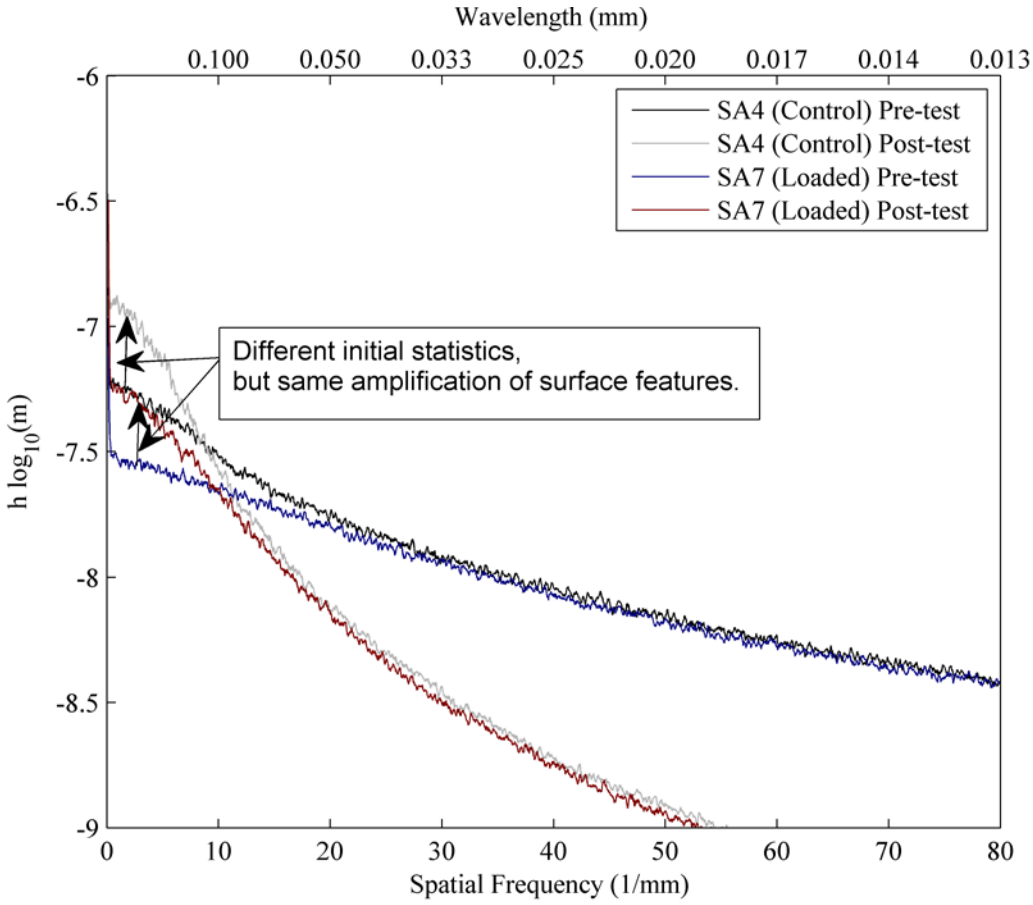

Figure 7.3: Pre versus post-test surface statistics for Exposure 1. Averaged Fourier-transformed line-scan amplitudes (log scale). 7-pt spatial frequency average reduces variability.

These results show that a growth process is operating on the initial pre-roughened amorphous fused silica samples. The final surface roughness Fourier components are an amplified linear function of the initial surface roughness Fourier components. The observed process of erosion does not appear to be a function of the applied mechanical loading in these amplification function diagrams, for loads of up to 25.0 MPa.

7.1.2 Auto-correlation Analysis

Another way to view the line-scan data, which is potentially more sensitive than Ψ to changes in the length-scale and depth-scale of the cell-patterns and pre-test

roughness is to use an auto-correlation function. Auto-correlation functions have been used in the past to analyze cracks in materials [59]. A crack develops by random-walking within a certain envelope. The slope of the autocorrelation function contains information about the dimensions of this envelope. For example, a slope of 0.5 would correspond to cracks contained in a square-root envelope as a function of distance from the starting point. Equation (7-1) shows the auto-correlation function used.

$$\Delta z(\Delta x) = \langle \big(z(x+\Delta x) - z(x)\big)^2 \rangle_r^{1/2} = \sqrt{\int_x \big(z(x+\Delta x) - z(x)\big)^2 dx} \qquad (7\text{-}1)$$

Microscope images of the cell-pattern that has been developed on each surface is given in the next section. In the case of the plasma eroded sample surfaces, there is short range order to the surface (within each cell), but no long range order (heights are within some constant value envelope over long distances). The variation of surface height is confined to a certain RMS roughness. The features which can be derived from the auto-correlation function are a sloped line to a cutoff, then a horizontal line. The height of the horizontal line is related to the roughness of the surface. The position of the cutoff provides information about the largest length-scale at which coherent surface features exist (vertically and horizontally), and is related to the cell-size, or to the size of the initial roughness pattern pre-test. As Δx increases, eventually the envelope of surface features stops growing because features further away than the length-scale of the largest coherent feature are uncorrelated with the height of the starting point. Figure 7.4 shows examples of pre and post-test autocorrelation functions of line-scans.

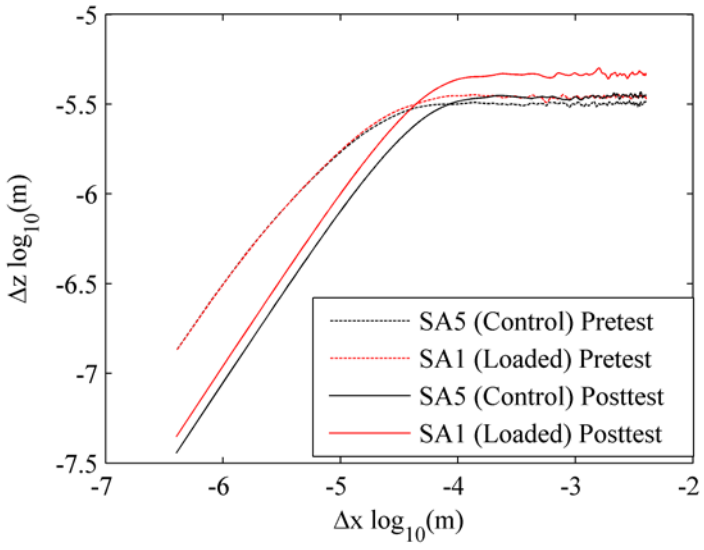

Figure 7.4: Autocorrelation functions for samples SA5 and SA1, pre and post-test.

Figure 7.5 shows the cutoff length-scales for pre and post-test line-scan series for each sample. The autocorrelation function is applied to each line-scan in a series, and the location of the cutoff is chosen to be where the curve has a 0.01 slope. The statistics for the cutoff location are collected, with the error bars showing standard deviation of the x and z cutoff location. Figure 7.6 shows the difference between pre and post-exposure autocorrelation cutoffs. This shows the changes in length and height scales between initial and final surface patterns.

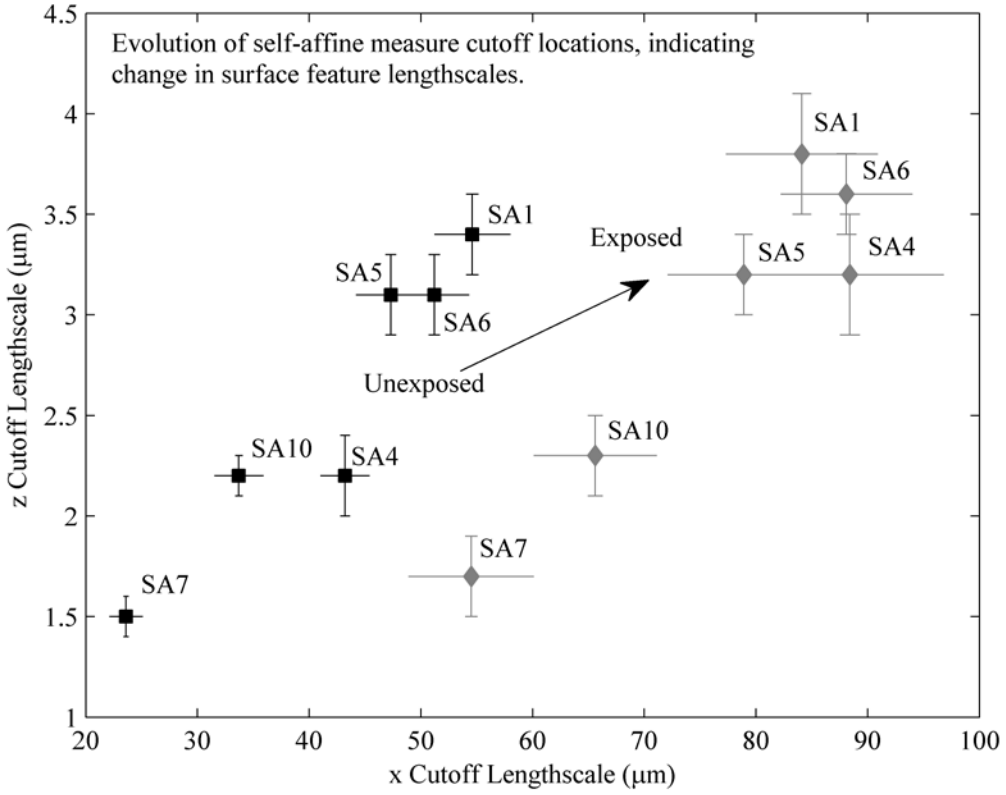

Figure 7.5: Pre-test versus post-test cutoff length-scales.

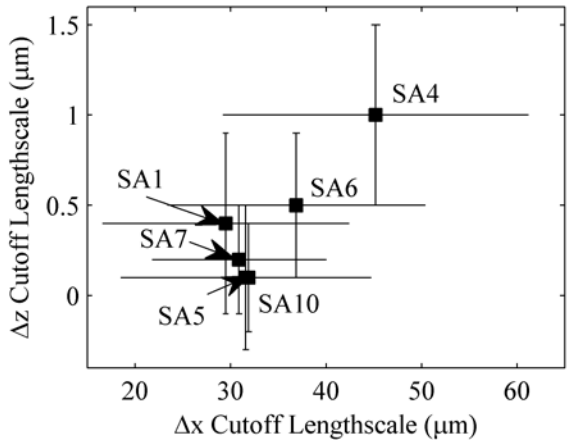

Figure 7.6: Change in pre versus post-exposure cutoff length-scales.

Figure 7.6 shows that for most of the sample pairs, the change in horizontal length-scale and depth of profile is approximately the same. The only outlier is SA4, but even for this sample, the standard deviation of cutoff statistics places it in the same neighborhood as the others. The final surface features are on average 30-40 μm larger in horizontal length-scale, and 0 to 0.5 μm deeper in terms of profile depth.

7.1.3 Surface Crystallography

X-ray diffraction crystallography (XRD) is conducted for four of the samples. The XRD is conducted on samples SA4 and SA7 after plasma exposure, and on sample SA6 and SA10 before exposure. Sample SA6 is pre-roughened, and sample SA10 is as manufactured (smooth) during the crystallography. XRD will reveal the presence of any crystalline grains in a material as a series of sharp peaks much greater than the noise floor. Figure 7.7 shows the XRD traces on the exposed surface of each sample. All traces, for both exposed and unexposed samples, smooth and pre-roughened, show the same amorphous curve without significant peaks. This demonstrates that no crystalline grains are present in or on the surface. The fused silica material is amorphous prior to exposure, and after exposure no crystallization takes place.

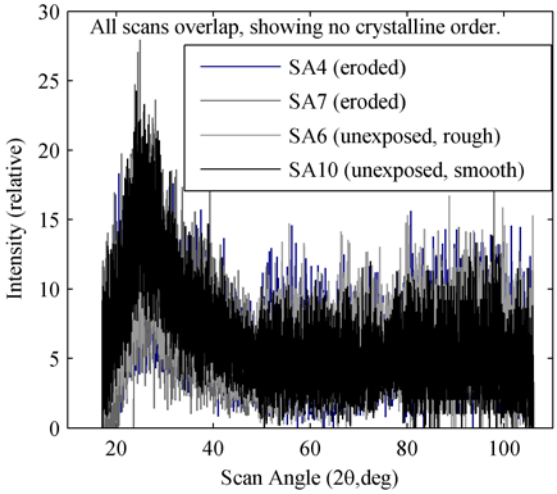

Figure 7.7: XRD intensity as a function of scan angle for exposed and unexposed samples.

The XRD analysis confirms that the material is amorphous, and remains amorphous after exposure to the plasma. The temperature reached by the samples during exposure are not more than 500 ºC, which is 200-300 ºC greater than the temperatures reached by the test fixture during the exposures. This information is from additional testing with thermocouples attached to the sample as well as the test fixture. The sample temperatures are well below the annealing temperature of SiO_2, which is 1215 ºC [57].

7.1.4 Pre and Post-Test Surface Microscopy

Microscopy was conducted to produce three-dimensional surface height maps, and images of the features developed by the plasma erosion process. Figure 7.8 shows the development of a cellular pattern produced by the erosion process acting on the pre-roughened sample surfaces. Figure 7.8 shows a height profile (a and c) taken using the Olympus LEXT laser microscope, and a laser profile image (b and d). The images are taken near the center of the sample, at the same locations before and afterwards. The

acquisition of the same location is done by measuring from the lower left corner of each sample with the motion stage encoder of the microscope.

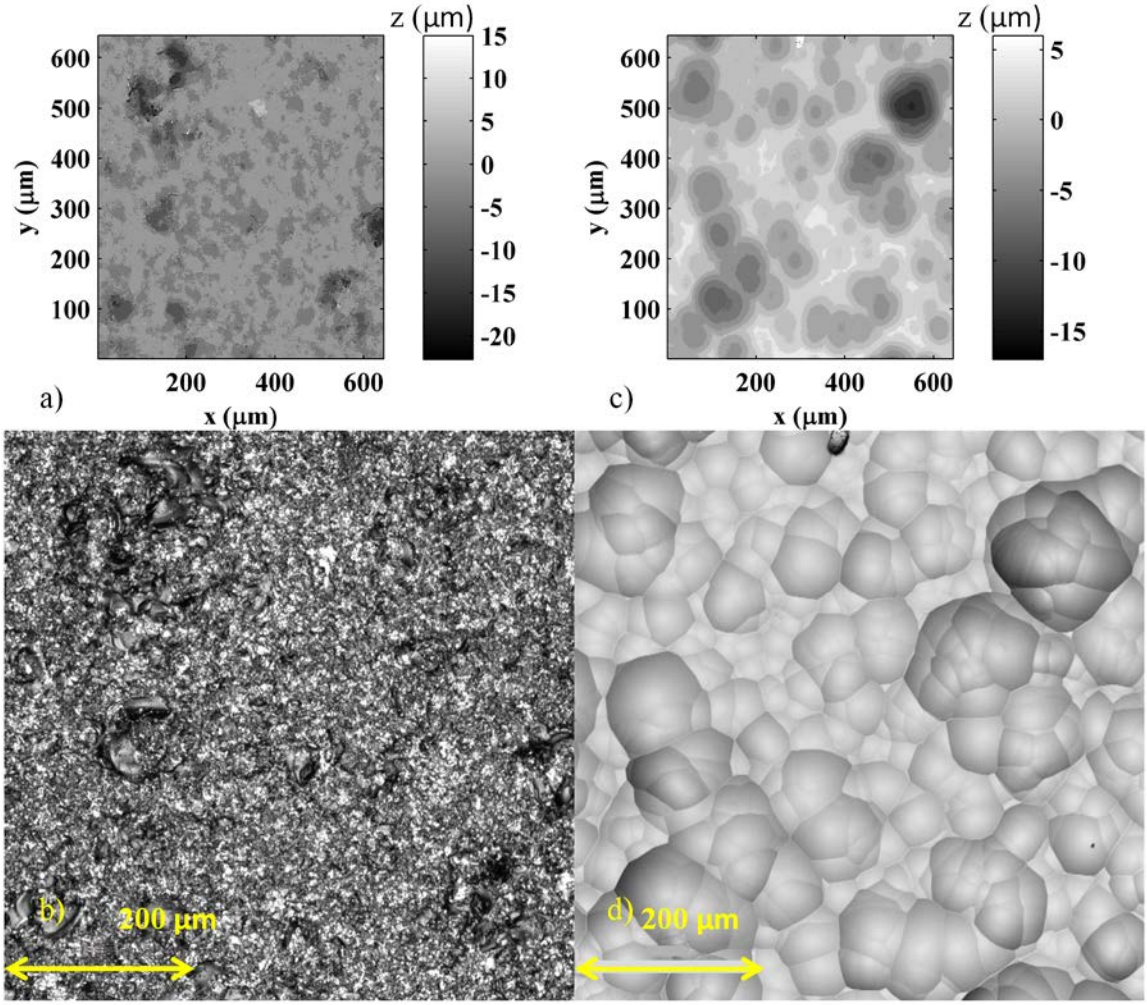

Figure 7.8: Pre and post-test sample microscopy: Fused silica sample SA6 (loaded), 20x, center of exposed surface, a, b) pretest height and laser image, c, d) post-test height and laser image.

On all the pre-roughened samples, a cell-pattern developed from the random white-noise initial roughness pattern. Figure 7.9 shows some representative line-scan profiles that reveal that each of these cells is a smooth mostly parabolic depression bounded by sharp-edged cusps. The surface has the overall appearance of a plane divided into Voronoi-like cells. Each cell is a cup (concave), not a bubble (convex). The distance

between the pre and post-test line-scan in Figure 7.9 is not to scale. It is intended to show each line-scan side-by-side.

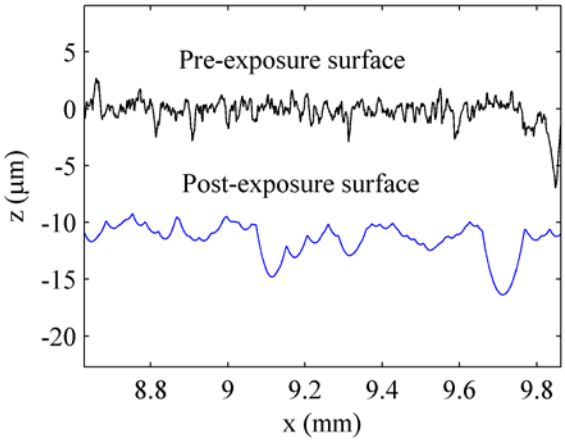

Figure 7.9: SA7 surface line-scan (surface height as a function of position) pre-exposure and post-exposure. 11-hr exposure, 120 V bias voltage, 2.5 mA/cm^2 argon plasma.

For exposure 3, two samples, SA8, and SA9 are exposed under the same load conditions as exposure 2 (14.9 MPa). The surfaces of these samples are left smooth (± 0.05 μm), as manufactured, except for a small area of sample SA9. This area is scored with the tip of 1/16 in. fine-pointed screwdriver to create a limited region where initial surface roughness is present.

Figure 7.10 shows the comparison of the scored region before and after exposure. Post-exposure, the unmarked regions of the smooth samples remain smooth in the microscope images taken with the LEXT. No apparent surface features resulting from a growth process appear to be present, as expected, because there are no surface features to grow from. However, the marked region shows the beginning of the same cell structure seen on the pre-roughened samples.

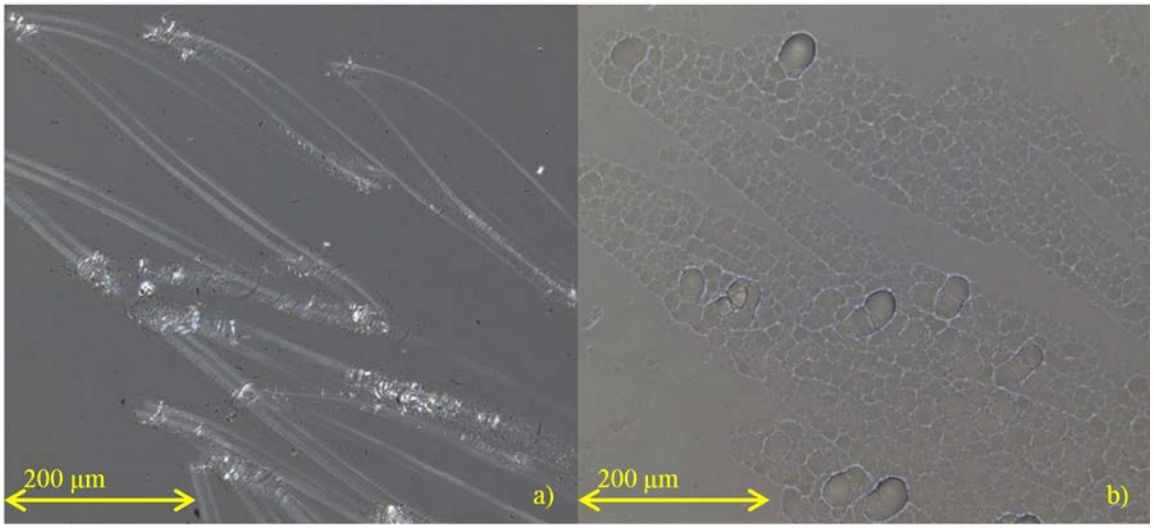

Figure 7.10: Sample SA9 laser microscopy, scored region, a) pre and b) post-exposure.

The results for the fused silica samples demonstrate that the surfaces develop according to a growth amplification process. In the absence of initial surface roughness, the surfaces remain flat. If there is initial surface roughness, a cell pattern develops. The growth process that is observed for fused silica seems to depend only on the initial surface geometry. In the discussion of the results given in Chapter 8, a plausible mechanism for the development and growth of the cell patterns is developed.

7.3 M26 Borosil Exposures

Four 3x1x0.25 in boron nitride samples have been exposed. Each sample was machined, then the surface was prepared with SiC polishing grit, as with the fused silica samples. Unlike the fused silica samples, each sample was polished first with rough 320-grit SiC, then with 500-grit SiC to produce a smooth surface. Pre-test surface roughnesses of 1.55 ± 0.10 μm are present due to the polishing.

Prior to exposing the M26 samples, one of the 3x1x0.25 in. samples, SC2, is tested to destruction in the clamp.. The sample failed at a strain of 1350 microstrain, or a stress of 30.8 ± 4.2 MPa. Future test loads were chosen to fall under this threshold to avoid prematurely cracking the samples. Table 7.2 presents the conditions under which each test was conducted, and the calculated relaxed loads applied to the experiment samples during the test. After each exposure, average erosion depths of 12.5 ± 2.5 μm are developed in each surface. These erosion depths are about two to four times less than those developed in the pure fused silica samples over the same exposure period, as expected due to the lower average sputtering yield of M26.

Table 7.2: M26 Borosil exposure conditions

Exposure	Exp. 1C	Exp. 2C
Loaded Sample	SC1	SC4
Control Sample	SC3	SC5
Initial Stress State (MPa)	23.4 ± 3.1	27.2 ± 3.7
Equilibrium Temp (°C)	241.3 ± 15.6	258.6 ± 2.4
Relaxed Stress State (MPa)	20.6 ± 3.3	24.1 ± 3.4
Relaxed Stress State (% orig.)	77.6 ± 12.3	77.8 ± 1.1
Duration (hrs)	12	12
Pre-Roughened	Yes	Yes
Altitude (cm)	32	32

7.3.1 Pre and Post-test Microscopy

As with the fused silica samples, pre-test and post-test images and height profiles are taken with the Olympus LEXT microscope. The same locations are visited pre and post-test using the motion stage.

Pre-test, the surfaces are whitish in color, without visible differentiation between silica and boron nitride grains. Post-test, all surfaces have evolved into shapes defined by the nature of the underlying grains. M26 is a composite of boron nitride flakes in a silica

matrix. Cross sectional SEM images of M26 are shown in Figure 3.3. In the post-test images shown in Figure 7.11, flat flake-like regions (the BN flakes) protrude at random angles from a background of silica. Regions with lots of silica erode slightly faster to form depressions. The nature of the surface appears to be determined almost entirely by the atomic sputtering properties of the grains. All samples have surfaces with similar appearances. The RMS roughness is greater post exposure: 4.26 ± 0.66 μm. In the post-exposure visible light images, the BN flake/protrusion regions appear darker in color. Figure 7.11 shows a measured location on sample SC3 before and after exposure. Prior to exposure, the surface is smooth. After exposure, the randomly oriented dark flakes are seen in both the visible light image, and as raised areas on the height map.

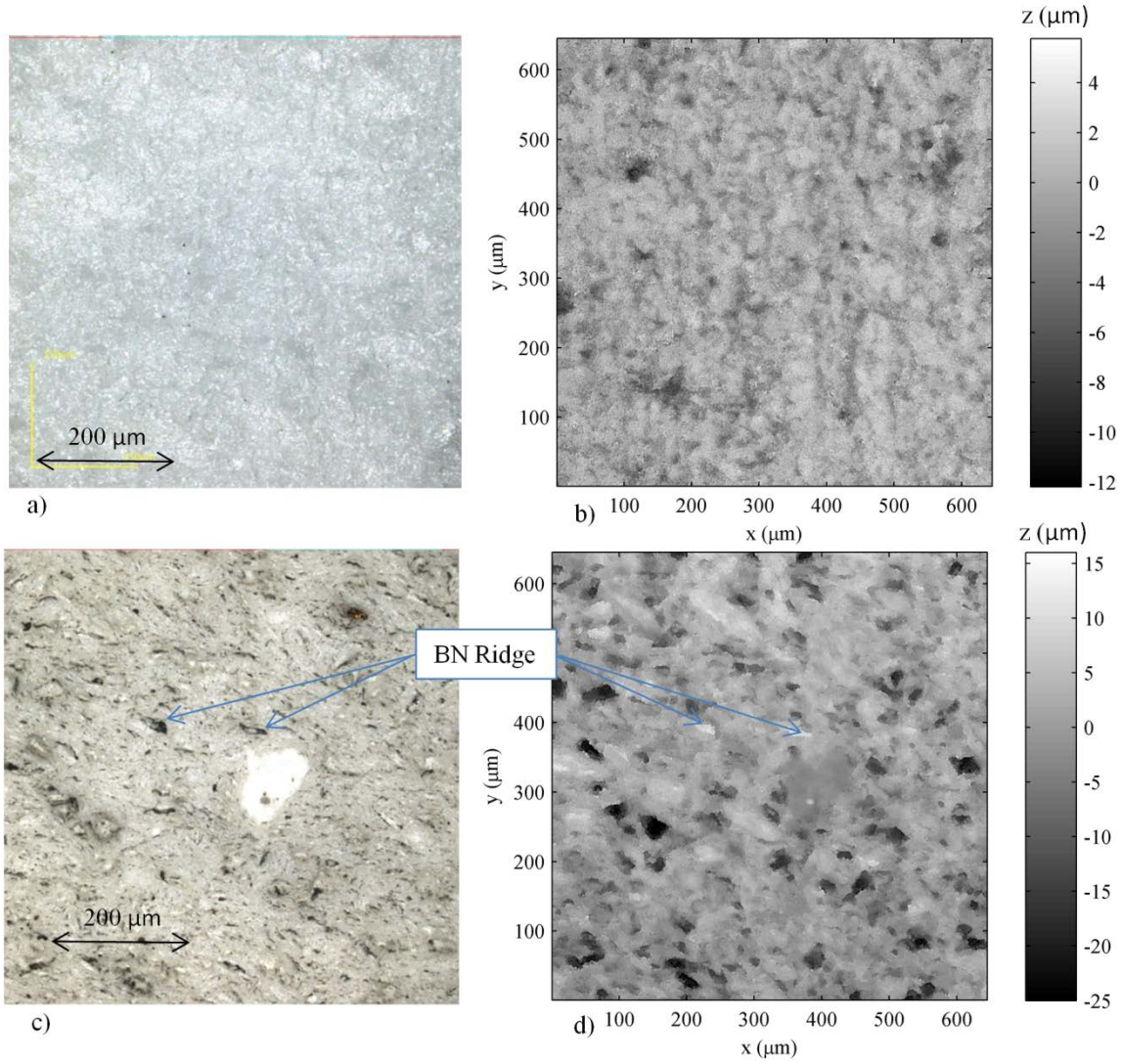

Figure 7.11: SC3 Pre-exposure surfaces a) visual image, b) laser height map, Post-test surfaces c) visual image, and d) height map.

Higher magnification images have a finer vertical resolution, and show the BN ridge phenomenon clearly. Figure 7.12 shows a high-magnification image of a BN rich region in the dark lower-left corner, protruding from the surrounding material. Figure 7.13 shows a 3D image, constructed by the LEXT, of the same region. In this image, the visible light image is superimposed over the height-map.

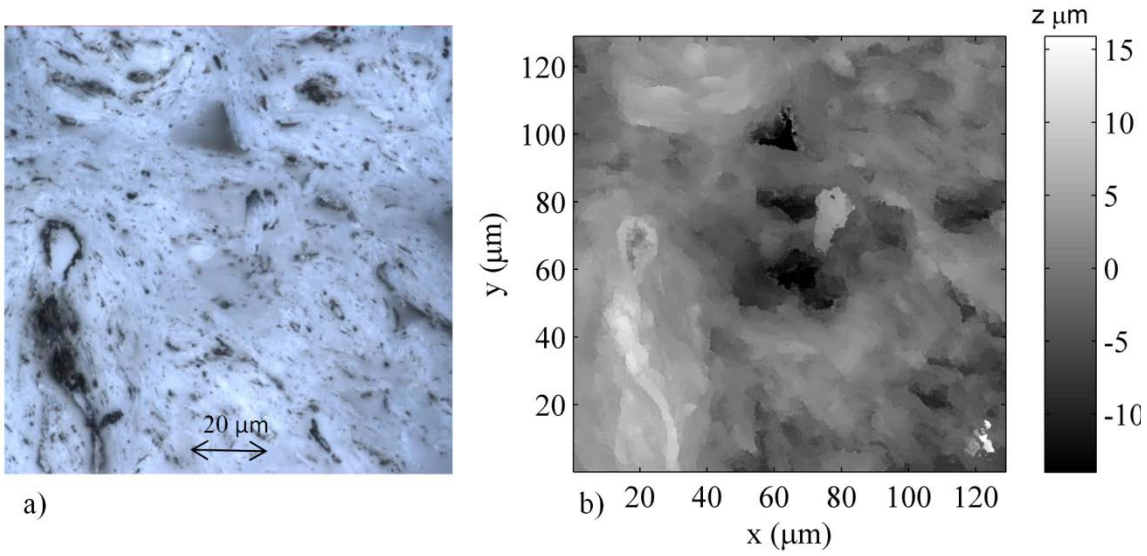

Figure 7.12: SC1 100x magnification post-exposure a) visible light image, b) laser height map.

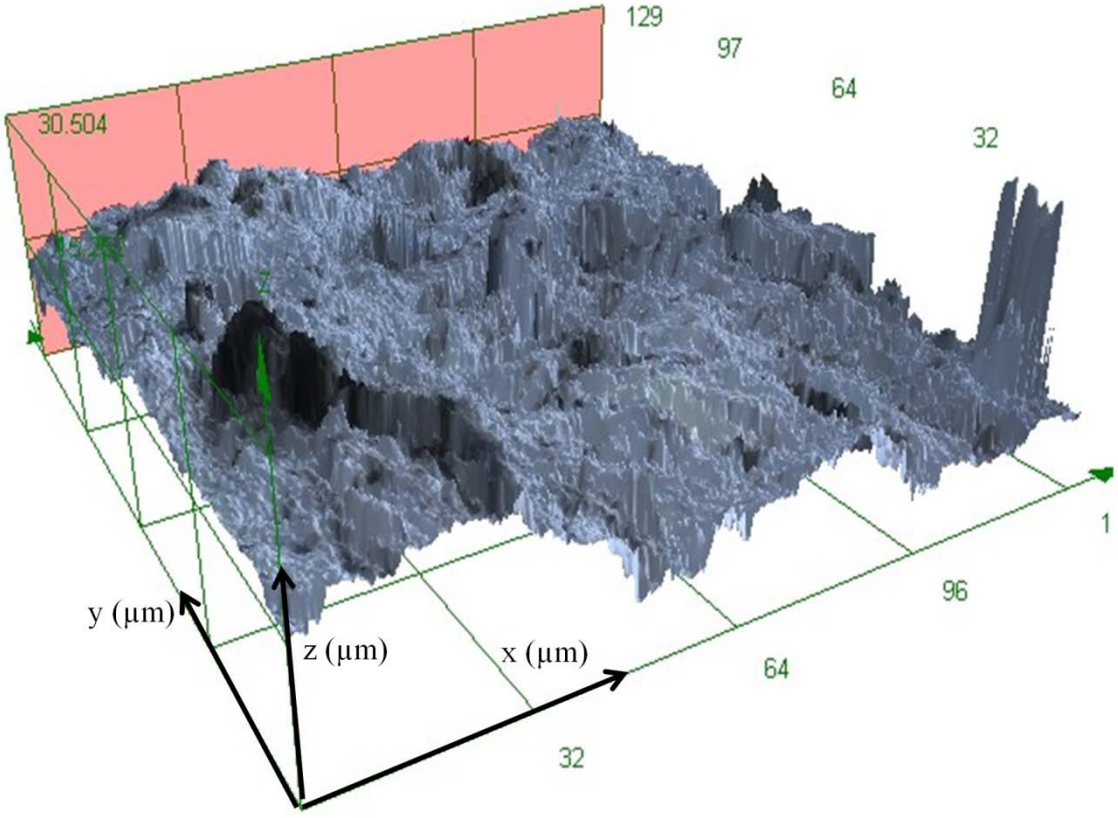

Figure 7.13: LEXT 3D visible image overlaid on height-map.

Regions in the upper-right corner of each sample, out of the way of the profilometer scans, were scratched with a 1/16 in. steel stylus, as with sample SA9 of the fused silica samples. Unlike the fused silica samples, surface structure appears across the M26 samples in more or less the same way. The largest scale features of the scratches appear to still be present post-exposure, but any smaller scale features appear to be governed by the underlying microstructure of the material, not the presence of the scratch.

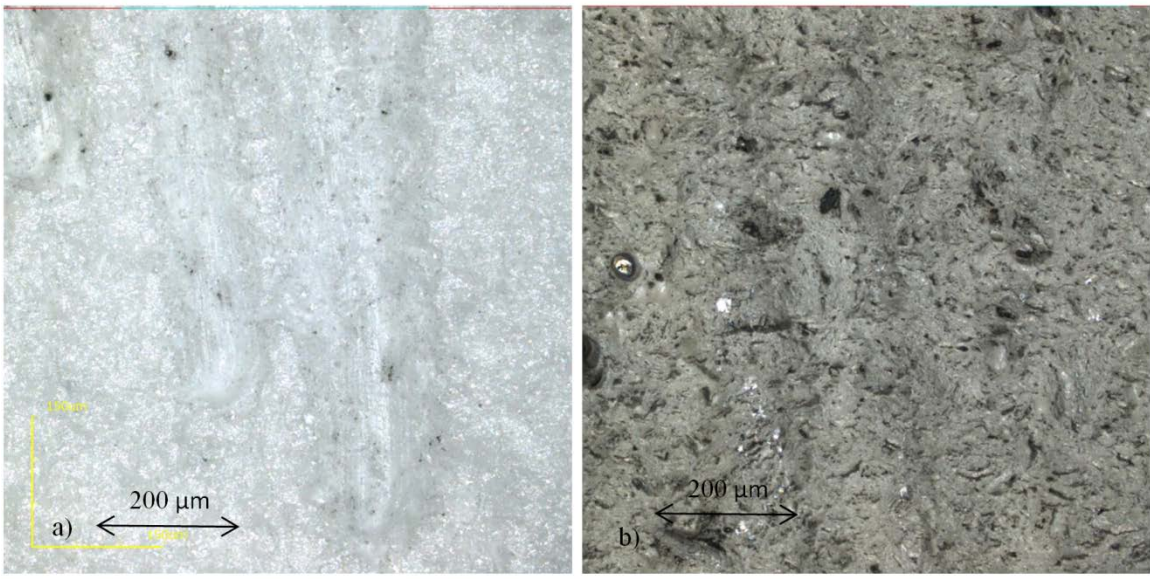

Figure 7.14: Pre-exposure visible image of scratch, b) Post-exposure visible image of scratch.

7.3.2 Amplification Functions and Surface Statistics

As with the fused silica samples, 50 line scans are collected from each M26 sample, before and after each exposure. The amplification functions derived from the pre and post-exposure line-scans show more variability than in the fused silica case. Unlike the fused silica case, there is no apparent cut-off length-scale below which features are being smoothed out (above 10 μm). Each curve can be distinguished for wave-numbers

less than 30/mm (corresponding to wavelengths longer than 33 μm). There is no systematic bias with respect to the loaded versus control samples, however. In the first exposure pair, the loaded sample has a larger value for Ψ. In the second exposure pair, the unloaded sample has a larger value for Ψ. Figure 7.15 shows the amplification function as a function of wavenumber for the M26 samples. Figure 7.16 shows the same figure with 7-point spatial frequency averages to more clearly distinguish each series.

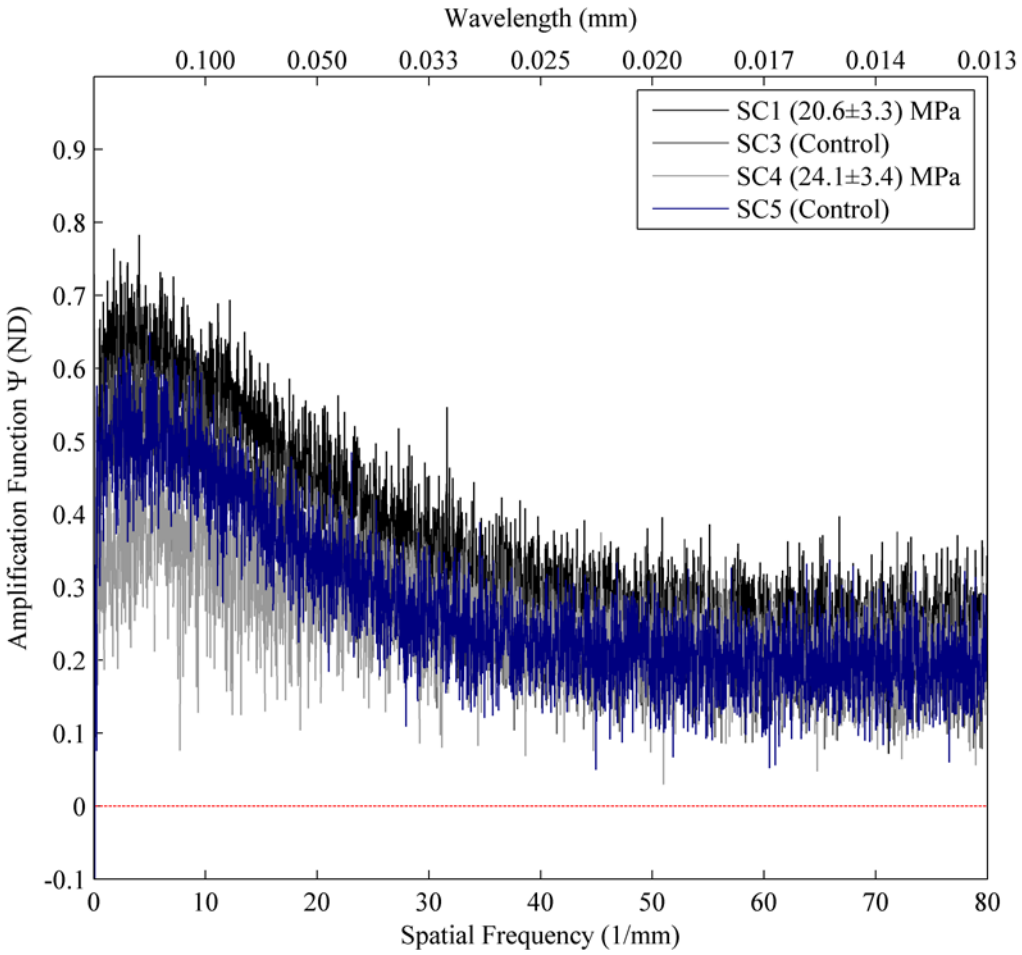

Figure 7.15: Amplification function, Ψ, as a function of spatial frequency for M26 exposure 1 and 2. Growth in features between pre and post-exposure occurs at all spatial frequencies.

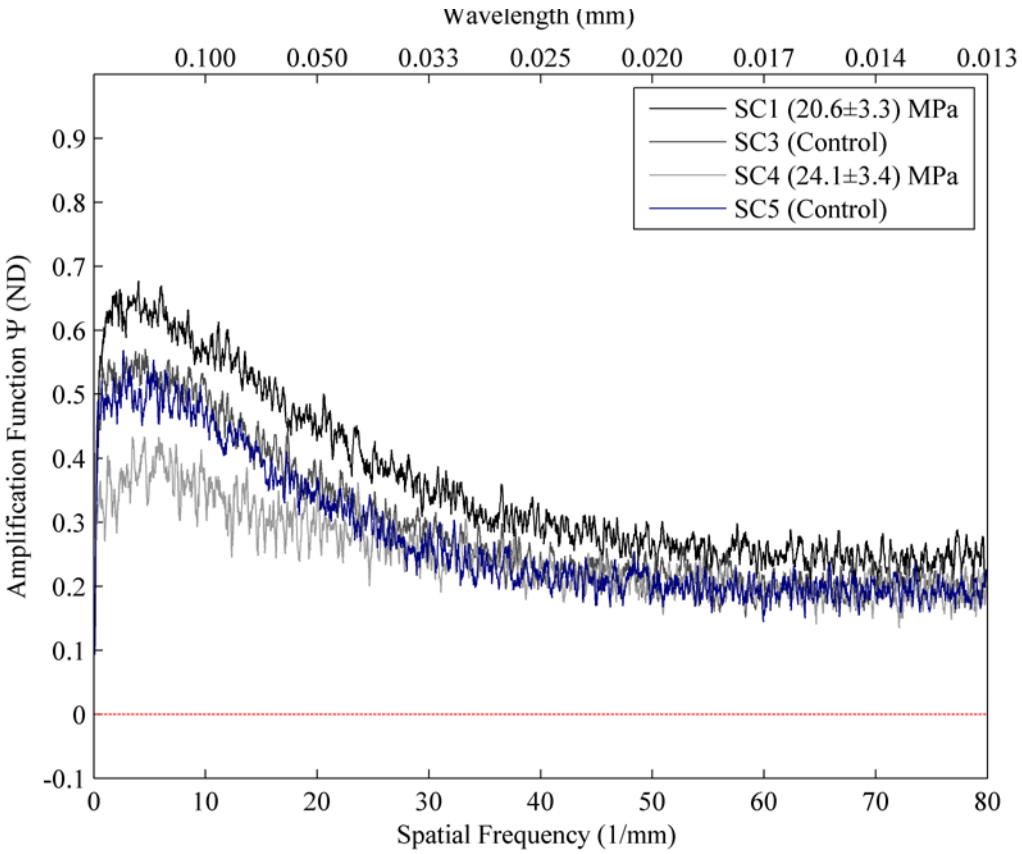

Figure 7.16: Amplification function, Ψ, as a function of spatial frequency for M26 exposures, with 7-pt spatial frequency averaging.

Figure 7.17 displays an overlay of the post-exposure versus pre-exposure surface roughness statistics. This figure shows that, while there are slight differences to the pre-test surface roughness statistics (due to the low initial surface roughness, and the sensitivity of the profilometer), there are almost no differences to the post-test surface roughness statistics. Post-test surface roughness statistics are the same to within 0.01 μm/wave mode.

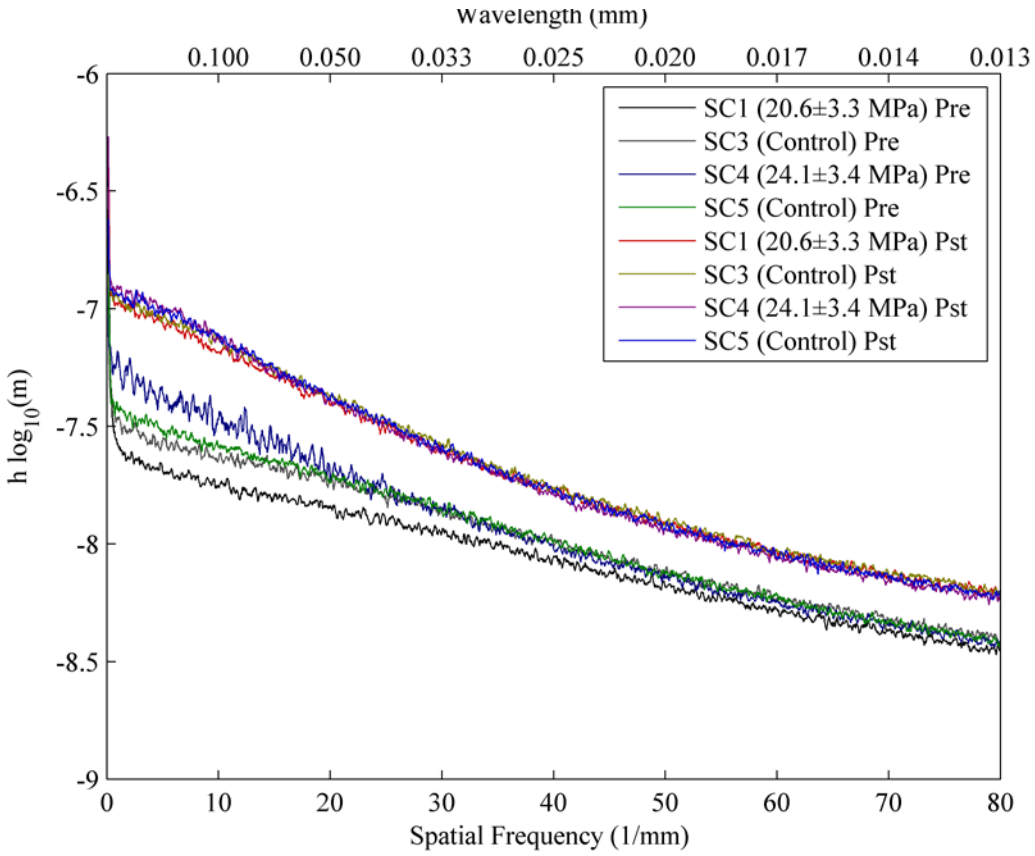

Figure 7.17: Pre and post-test surface roughness statistics. Averaged Fourier-transformed line-scan amplitude as a function of spatial frequency.

Post-test statistics overlap to within 0.01 µm/wave mode.

Contrast Figure 7.17 with Figure 7.3 for the fused silica samples: In the case of the fused silica, the difference between the log of pre and post-test roughness statistics was the same for each case, even though the initial and final roughness statistics differed. The final roughness statistics are *proportional* to the initial roughness statistics for fused silica. For the M26, the final surface statistics are *insensitive* to the initial surface statistics.

What this demonstrates is that for the amorphous fused silica samples the development of the post-exposure surfaces appears to be entirely determined by the pre-

exposure surface structure. For the M26 samples, the presence of the microstructure is the stronger influence on the evolution of the surfaces. As outlined in Chapter 3, the final surface structure is instead governed by the difference in sputtering yield of each component material. For both M26 and fused silica samples, no dependence of the evolution of either surface on mechanical stress has been observed, for mechanical loads of up to 24.99 ± 1.10 MPa for fused silica, and up to 24.1 ± 3.4 MPa for borosil. In order for dependence on mechanical stress to be detected, a difference greater than the noise floor (0.01 μm/wave mode, or 0.1 (nondimensional) for Ψ) must be detected, varying in a systematic way, between the loaded and control samples. No such dependence has been found.

CHAPTER 8

DISCUSSION OF STRESSED EROSION EXPERIMENT RESULTS

8.1 Overview

The results from the stressed erosion experiment show two different primary mechanisms for the surface evolution of the simple amorphous fused silica samples, and for the evolution of surface structure on the M26 samples. For fused silica, the final surface profile is shown to be a function only of the initial surface profile. Surface roughness statistics are proportional to initial surface roughness statistics in a highly consistent way across all exposed samples. For M26, the final surface statistics are insensitive to the initial surface roughness statistics. All of the samples attain the same final surface roughness statistics regardless of the initial surface roughness statistics. As stated in the last chapter, the main difference between the fused silica samples and the M26 samples is the absence (in the case of fused silica) or presence (in the case of the composite microstructure of M26) of microstructural detail in the material.

As described in the next section, the evolution of the surface profile of fused silica depends only on the initial surface profile. There is no differentiation or details in the material with which to interact. The development of the cell pattern in the fused silica samples is explained as the result of the angle dependence of the atomic sputtering yield causing local changes to the sputtering rate of the surface profile. For the M26 samples, differences in sputtering yield between the BN flakes and silica matrix is the primary

mechanism governing the development of surface features. This mechanism is investigated in detail in Chapter 3.

The stressed erosion experiment applied stresses of up to 24.99 ± 1.10 MPa for fused silica, and up to 24.1 ± 3.4 MPa for the M26 samples. These stresses are just under the maximum loads that can be reliably applied to the samples before they crack. In addition, referring to Figure 5.4, these loads are large enough that unstable wave-modes on the order of mm in wavelength should result, if the hypothesized strain relief mechanism controlled the formation of surface features. However, under all load conditions, no differences between the surface evolution behavior due to the presence versus absence of mechanical stress has been detected. In order to claim that a systematic difference in surface evolution as a function of mechanical stress is present, a difference in the amplification function or the roughness statistics must be observed. The amplification function must show a difference with the control sample of greater than the uncertainty of 0.15 (nondimensional). The roughness statistics must show a difference greater than the uncertainty of 0.05 μm/wave mode. Even with 7-point spatial frequency averaging, the amplification functions for the fused silica are remarkably similar between all samples, especially sample pairs of a given exposure. They show similarities in Ψ across all spatial frequencies to within 0.05. For the M26, final roughness statistics are the same between loaded and control samples to within 0.01 μm/wave mode across all spatial frequencies. No variation in the evolution of the surface profiles due to mechanical stress has been detected. It is proposed that this insensitivity is due to the large difference in strain energy densities relative to the energy cost of the atomic sputtering process, as outlined in Section 5.5. Similar reasons are used to explain the

insensitivity of the atomic sputtering process to material temperature in Lagried and Sigmund's work [51] [52].

8.2 Proposed Mechanism for the Development of the Cell Pattern

The simplest hypothesis that plausibly explains the growth of the cell patterns in the exposed fused silica surfaces is that these patterns result from the angle dependence of the sputtering yield of the material. Under normal ion bombardment, the local angle that the surface makes to the incoming ions modifies the local sputtering yield, and speed of erosion. In sputtering yield theory and experiment, the yield tends to peak at ion incidences of 50º to 80º from the surface normal of the target. In a semi-infinite medium, there will be an angle at which the repulsive action of the surface atoms prevents the ions from penetrating into the target (and hence a reduction in yield from the maximum). At moderate ion incidence angles to the surface normal, ion impacts produce a region of energized atoms below the surface at an angle to the surface. At these angles the proportion of this region that lies close enough to the surface to allow atoms to escape the target scales as $1/\cos(\theta)$. θ is the ion angle relative to the surface normal If the ion mass is greater than the atomic mass in the target, as is the case for argon and xenon with a SiO_2 target, then $1/\cos(\theta)$ is a good model. If the masses are more nearly equal, the angle dependence scales as $1/\cos(\theta)^{5/3}$ [52] [60].

For the following analysis, a curve fit of the modified Yamamura form is made to empirical angle dependent yield data collected by Yalin *et. al.* for xenon sputtering of fused quartz [35]. The form of the model is given in Equation (8-1), while the coefficients of the model are given in Table 8.1. The angle dependence of the yield is

shown in Figure 8.1. Figure 8.1 shows that a 3rd-degree polynomial fit to the data peaks at 55º ion incidence to the surface normal.

$$Y(E,\theta) = f(\theta)g(E) = (B_0 + B_1\theta + B_2\theta^2 + B_3\theta^3)k\sqrt{E}\left(1 - \sqrt{\frac{E_{th}}{E}}\right)^{2.5} \quad (8\text{-}1)$$

Table 8.1: Yield model fitting coefficients.

Variable	Value	Unit
k	5.0×10^{-3}	$mm^3/C\text{-}eV^{0.5}$
E_{th}	15.0	eV
B_0	1	1
B_1	0	1/deg
B_2	1.11×10^{-3}	$1/deg^2$
B_3	-1.37×10^{-5}	$1/deg^3$

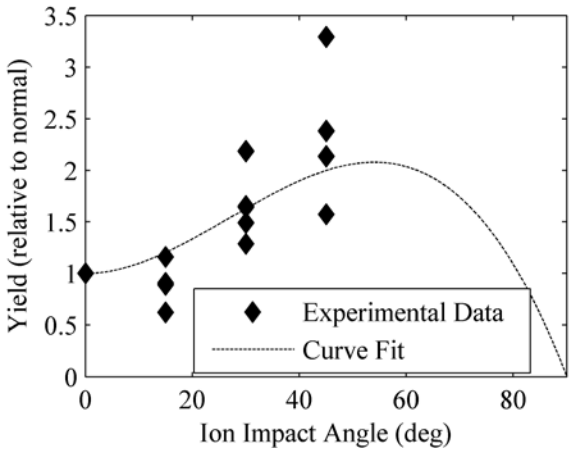

Figure 8.1: Sputtering yield of fused quartz as a function of ion incidence angle. Data from [35], for xenon ions, 250, 350, and 500 eV ion energies.

Townsend noted that due to the higher sputtering yield of surfaces at an angle to an ion beam, certain initial surface profiles, such as spheres or sinusoidal surfaces would

develop, over time, into cones or cusps as erosion proceeds [60]. A one-dimensional simulation of the evolution of a surface profile by atomic sputtering is constructed which demonstrates this behavior. The simulation calculates the rate of erosion at each point along a surface profile as a function of the surface normal of the neighboring area elements. The simulation evolves the surface profile in time, producing eroded surface profiles from un-eroded surface profiles. Timesteps of 5 s are used to simulate the evolution of surface profiles with a 0.4 nm horizontal spacing between nodes. Ion current densities of 10 mA/cm^2 and ion energies of 100 eV are used, similar to conditions in the IAD chamber experiment. Figure 8.2 shows relative error as a function of timestep between simulations. This demonstrates that the simulation is well converged for 5-s timesteps. The reference solution is one run at 2.5-s timesteps, to which the other solutions are compared.

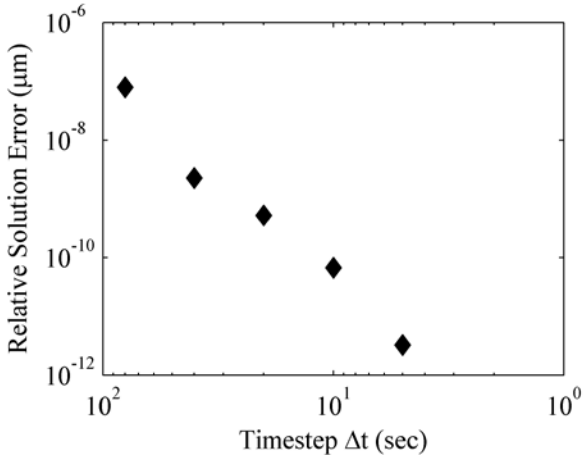

Figure 8.2: Convergence: Error relative to 2.5-s timestep solution as a function of timestep.

Figure 8.3 shows the evolution of a sinusoidal profile, showing the development of cusp shapes. The sloped edges erode faster than the land at the top and bottom of the profile, leading to a widening of the base and narrowing of the peak of the profile.

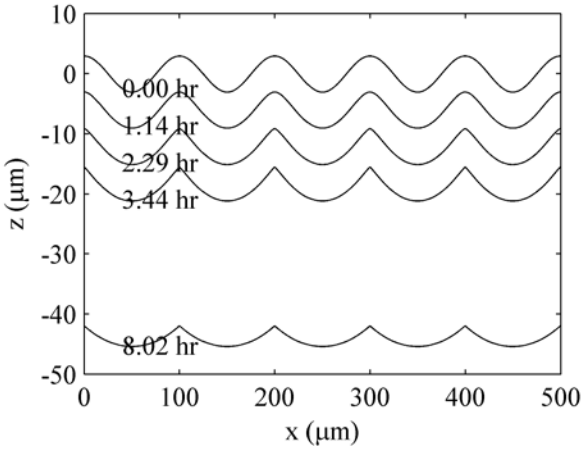

Figure 8.3: Surface profile as a function of time. Note the development of cusps from initial sinusoidal features.

A 500-μm section is taken from the pre and post-test line-scans from sample SA6. A simulation of the erosion of the top surface is propagated forward in time for 11 hours. At erosion depths similar to the ones reached during the 11-hour experimental exposure, a profile with features similar to the experimental post-test surface is observed. Figure 8.4 shows the pre and post-test line-scans in blue and several time-steps of the simulated evolution of the top profile in black. The actual surface is two-dimensional, and so there is an extra dimension for the profile to be off-normal to the ion beam. However, even with a one-dimensional simulation, features of a similar depth and profile to the post-test surface develop.

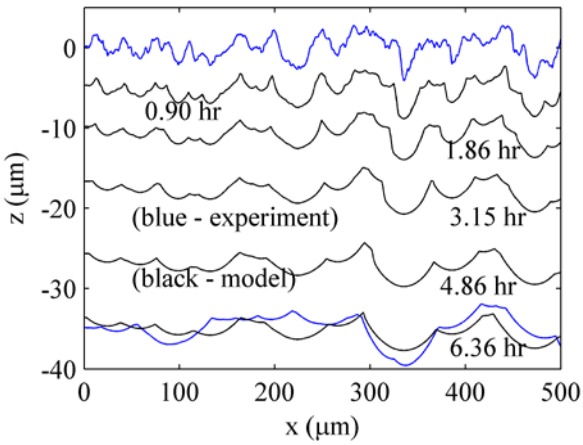

Figure 8.4: Measured and simulated surface profiles as a function of time.

Because of the similarity in features between the simulated and measured surface profiles, it is believed that pure local atomic sputtering is sufficient to explain the development of the cusps and cellular pattern on the post-test fused silica surfaces. This mechanism is purely local, therefore the only length-scales present in the problem physics are the length-scale involved in the initial surface roughness, and the average depth of the erosion.

Fifty 1-mm long subsets are taken from the 50-mm long line-scans recorded by the Tencor. The pre-exposure line-scans are propagated using the model to the average erosion depth attained during exposure. From the simulated post-exposure line-scans, Fourier statistics similar to the experimental statistics in Figure 7.1are derived. Figure 8.5 shows a comparison of the amplification function for the experimental and modeled profiles for sample SA6. These amplification functions have less spatial frequency resolution than the ones shown in Chapter 7, due to the smaller length of the simulated domain, but show the same general trend. Both the simulated and experimental amplification profile show growth of features with a longer wavelength than 0.1 mm, and

damping of smaller wavelengths. The amplification statistics agree well until approximately 30 mm^{-1}, and after that, the simulation shows less damping of higher frequency features than the physical process. This might point to the existence of a smaller order diffusive process not captured in the model. Arguably, high spatial frequency information, due to the smaller order of magnitude initial and final amplitudes, is more noisy and less important in defining the pre and post-test surfaces. The agreement at spatial frequencies below 30 mm^{-1} corresponds to the qualitative similarity between the modeled and experimental post-test surfaces.

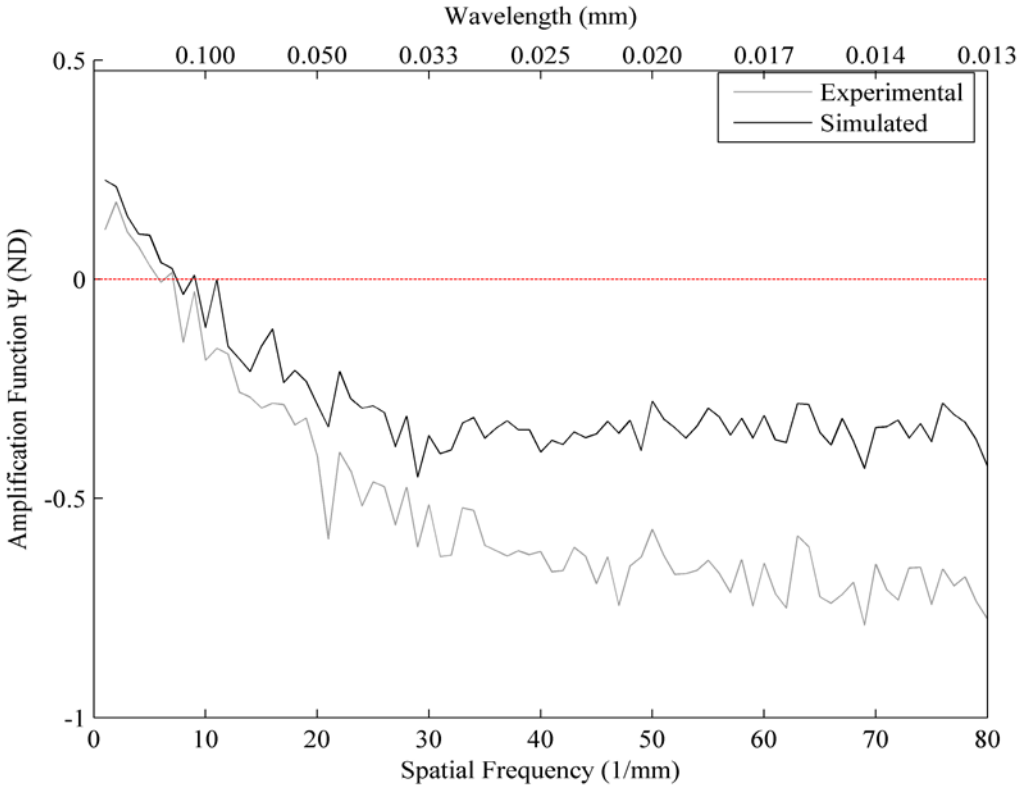

Figure 8.5: Amplification function Ψ as a function of spatial frequency for experimental and simulated profiles.

It may be the case that the cell pattern observed during the fused silica experiments will not persist for arbitrary erosion depths: The top and bottom of the

profile, with the exception of any cusps that develop, are normal to the ion beam, and therefore must erode at the same rate, according to the model. The cusps erode faster than this, and may vanish given enough time. Therefore in the absence of surface features inclined at more than 55º to the normal, the range of the profile predicted by this mechanism is bounded above by the initial profile range. The average curvature and profile depth of the modeled sin-waves show this behavior. After the development of the cusps at 20-μm average erosion depth, the average curvature peaks. The depth of the profile begins to decrease with further erosion. Figure 8.6 shows the envelope height and average curvature as a function of the average erosion depth for the sinusoidal profiles.

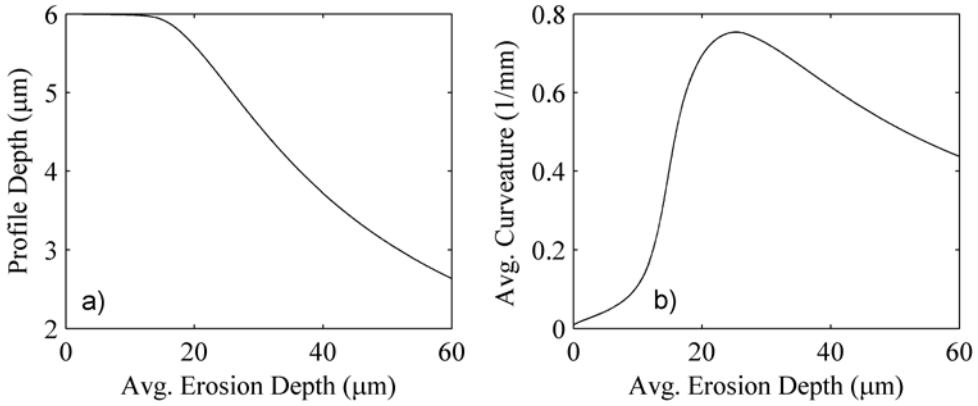

Figure 8.6: a) Profile depth b) average curvature for the modeled evolution of the sinusoidal profile.

8.3 Discussion of M26 Erosion

The features developed on the M26 samples are best explained as resulting from the differences in sputtering yield between the BN and silica components of the composite. BN has a lower sputtering yield in general than silica [35]. Chapter 3 provides

details of a 3D model of the erosion of M26 borosil. In this model, independent sputtering yield models are used for exposed BN and exposed silica to model the evolution of a 3D surface profile. The surface geometry is updated as it propagates into a simulated 3D model of the material domain.

In the paper [30], and in Chapter 3, the model is used to successfully reproduce some surface features that are observed in SEM microscopy of the eroded channel wall of the AFRL/UM P5. The AFRLUM P5 is a 5-kW HET tested for several thousand hours at the University of Michigan [32]. Figure 3.4 shows incoming ions at an angle to a complex surface structure affecting a surface composed of low-yield BN and high-yield silica. At an angle to the surface, a cliff and valley structure develops as the BN shields the higher yield fused silica material from incoming ions. Figure 3.17 shows the surface profiles produced by the model, in comparison with the cliff-and-valley structures observed in the eroded channel wall of the AFRL/UM P5.

The stressed erosion experiment exposed the M26 samples to a normally incident ion beam. In this case, the shadowing effect is less important, but the long, thin BN grains still protrude from the surface, creating surface profiles observed in the experiment. Even if the initial surface were completely flat, surface features of a certain character and equilibrium roughness would eventually develop from erosion into the material due to the material microstructure. The erosion depth developed in the experiment is only 12.5 ± 2.5 μm. The simulation of the evolution of the P5 channel wall did not reach steady state in rms roughness until an erosion depth of 100 μm. In order to observe the sort of features that develop in steady state, or to confirm that the material will reach the steady state that the raytracing model predicts, larger erosion depths must be achieved in

future work. In addition, if long duration or high intensity exposure experiments are to be conducted in future work, it would be useful to impinge ions at an angle to the surface, to reproduce the shallow ion impact angles in a HET.

The model described in Chapter 3 successfully reproduces the cliff-and-valley structure seen in the P5 channel wall, but cannot reproduce the composition change observed in XPS spectroscopy. To explain this phenomenon, a new model, such as the one described in Section 3.5, and depicted in Figure 3.21 and Figure 3.22 may be needed.

8.4 Time Constant Analysis of Growth Process

Long duration HET life testing takes place over the course of thousands of hours. This experiment is limited to plasma exposures shorter than 12 hrs because of the length of time the plasma source will operate in a uniform discharge. To verify that something useful can be said about the development of the anomalous ridges with this experiment, which is far shorter in duration, an analysis of the statistics provided by the line-scan profilometry is made in this section. The spatial frequency resolution afforded by the line-scans and vertical resolution (0.5 Å) of the Tencor P-15 profilometer allow statements to be made about the minimum possible time constant for an autonomous stress-dependent growth process.

If the anomalous ridges result from a process driving the growth of initial surface features into a final ridge-pattern, then this implies an upper bound on the time constant of the growth process. The growth process must be capable of growing features from the micrometer scale of initial surface roughness to the millimeter scale of the depth of the erosion ridges over the course of long-duration life testing or long-duration operation of

the thruster. Equation (8-2) shows how a given wave-component would grow autonomously in time. In this equation a is the amplitude of a surface wave or variation to the average profile, t is the elapsed exposure time, and τ is the time constant of the growth process.

$$a(t;\omega) = a(0;\omega)\exp(t/\tau(\omega)) \tag{8-2}$$

Garner's life testing of the SPT-100 includes figures that show the presence of the anomalous ridges after 1795 hrs of operating the thruster [6], implying a maximum time-constant of growth of about 260 hrs. Mazouffre *et. al*'s work with the PPS-1350G show the presence of the ridges after a 3500-hr life-test, implying a maximum time 500-hr time constant [20].

The sensitivity and spatial frequency resolution of the contact profilometry allows a very accurate measurement of a lower bound for the time-constant of a hypothetically stress-dependent growth process acting on the initial surfaces of the samples. A Euclidean functional distance between the amplification functions for the stressed and control sample can be defined according to Equation (6-2). This provides the average RMS distance between the amplification functions. The integration and comparison of several spatial frequencies, with averaging across spatial frequencies, allows the variability in the line-scan statistics to be suppressed.

$$< \Delta\Psi > = \sqrt{\frac{\int_0^{\omega_f} |\Psi_1(\omega) - \Psi_2(\omega)|^2 d\omega}{|\omega_f - 0|}} \tag{8-3}$$

Using this functional to measure the difference in amplification function between the loaded and control sample of exposure 4, a value of 0.018 was found for $<\Delta\Psi>$. In this calculation, a cutoff of 40 mm^{-1} and 100-pt spatial frequency averaging were used.

This implies that if a stress dependent growth process were present, it must have a time-constant of more than 280 hrs or a stronger difference between the loaded and control amplification functions would be observed. Equation (8-4) relates $<\Delta\Psi>$ to the time-constant of the growth process.

$$\tau = \frac{t}{\ln(10) < \Delta\Psi >} \tag{8-4}$$

A similar argument can be made comparing the difference for the post-test statistics for the M26 samples. Using a similar RMS functional distance, given in Equation (8-5), a bound on the time constant for M26 exposure 2 can be made. For the post-test statistics for exposure 2, $< \Delta\hat{h} >$ evaluates to 0.0024 μm using 150-pt spatial frequency averaging. This value leads to a minimum bound on the time constant of a hypothetical autonomous growth process of 490 hrs. 50 mm^{-1} was used as a cutoff spatial frequency for the integration. The reference magnitude for initial surface structure was 0.1 μm.

$$< \Delta\hat{h} > = \sqrt{\frac{\int_0^{\omega_f} \left|\hat{\mathrm{h}}_1(\omega) - \hat{\mathrm{h}}_2(\omega)\right|^2 d\omega}{\left|\omega_f - 0\right|}} \tag{8-5}$$

$$\tau = \frac{t_{test}}{\frac{\Delta\hat{h}}{\widehat{h_0}}} \tag{8-6}$$

These time-constant measures state that if an autonomous growth process that is a function of the stresses under 25 MPa were present, and fast enough to possibly explain the development of millimeter waves after thousands of hours, then a more significant

difference between the loaded and control amplification functions (for fused silica) or post-test statistics (for M26) should be observed. This analysis assumes that what is being detected is an autonomous growth process that develops exponentially in time from initial surface roughness. It also assumes that the evolution of all wave-modes and structure in the surface proceeds independently, that all surface features are infinitesimal and all evolution can be linearized.

This analysis makes many assumptions to derive a thousand hour comparison from a 12 hour experiment. However, the observed stress-independent amplification process that governs the growth of fused silica has a time constant of 26 hours. For M26, effects from the microstructure of the material dominate any hypothetical stress dependent effect. There are much faster processes than a stress dependent process that is too weak or slow to be detected in the observed data.

8.5 Summary

The stressed erosion experiment, designed to test the dependence of plasma erosion on the presence of mechanical stress in materials, is conducted. The experiment investigates fused silica and M26 borosil. Pairs of samples, one compressively loaded, and the other free to expand, are exposed to argon plasma for 11-12 hrs. Detailed statistics from surface profilometry and microscope images are collected from each sample before and after exposure to the plasma. Compressive stresses of up to 25 MPa are applied to the loaded sample of a pair, while an unstressed control sample is also exposed. Contact profilometry conducted before and after each exposure provide detailed Fourier statistics of the initial and final surfaces of each sample. The surface statistics

reveal that, for the stress ranges tested in this experiment, no difference is discernible between the evolution of the stressed samples and the control samples. For loads of up to 25 MPa, no evidence for the dependence of plasma erosion on mechanical stress is found. While evidence for an effect dependent on mechanical stress is not found, models are found that successfully reproduce the development of both fused silica and M26 surfaces.

CHAPTER 9

CONCLUSIONS AND FUTURE WORK

9.1 Research Contributions

This work investigates the erosion of insulating materials by an incident plasma. In particular, the work looks to understand the impact of the material microstructure and mechanical stress on the erosion mechanisms. The results of this work provide five distinct contributions to the understanding of plasma-induced erosion.

The first contribution of this work is the creation of a 3D raytracing model of plasma erosion of a heterogeneous composite material. The eroded channel wall of the AFRL/UM P5 is studied via SEM microscopy and XPS spectrometry. The details of the composition of the M26 borosil composite are explored with detailed SEM images. Borosil composites, such as M26 have a complex heterogeneous microstructure. The differences in sputtering yield between the fused silica matrix and boron nitride grains lead to the development of complex surface features. A raytracing model is created, which simulates the evolution of a surface profile exposing each material from a 3D material domain to ion bombardment. The model managed to reproduce the cliff-and-valley features observed in microscope images of the surface of the P5. The evolution of observed surface structures can be explained in terms of the model. However, observed changes in the composition of the eroded channel wall surface are not reproduced in the model. Chapter 3 discusses the details of this contribution.

The second contribution of this work, discussed in Chapter 4, is the creation of a thermo-mechanical model that predicts thermo-mechanical stresses for reasonable estimates of plasma heat-flux to the walls and experimentally measured temperature ranges for multi-kW HETs. The thermo-mechanical modeling provides estimates of the range of thermo-mechanical stresses it is reasonable to expect in kW-class HETs. Thermo mechanical stresses in the T-140 are estimated based on experimental temperature measurements and mechanical and thermal boundary conditions to be between 0.1 and 6 MPa. The stress of a borosil composite is not likely to be greater than 30 MPa, as that is the flexural strength limit of the material.

The third contribution of this work is the development of a hypothesis, called the Strain Relief Hypothesis (SRH), that is proposed to potentially explain the development of the anomalous erosion ridges in HETs. The theory behind the hypothesis is explained in Chapter 5, and the governing equations are derived. The ranges of unstable wavelengths expected as a function of applied stress is predicted in Figure 5.4. An attempt is made to estimate the speed at which the hypothetical mechanism will autonomously develop surface features. One potential problem with the SRH is explained in section 5.5: Mechanical strain energy, like thermal energy in a material is orders of magnitude smaller than the energy density of the atomic sputtering process. This suggests that the presence of mechanical strain energy may not perturb the sputtering process enough to yield significant growth of surface features in the timescale of HET operational life. However, an instability is present, and wavelength scales, governed by strain energy density and free surface energy, are within the ranges of interest to explain the anomalous ridges.

The fourth contribution of this work, described in Chapters 6 and 7, is the design and execution of an experiment to test the effect of mechanical stress on the surface features developed during plasma erosion. The experiment is also designed specifically to test the SRH. A test fixture is constructed to apply even compressive mechanical loads to material samples as they are exposed to plasma in a vacuum chamber. Two materials are tested in the experiment: Fused silica and M26 borosil.

Samples are machined to 3x1x0.25 inches, and their surfaces are pre-roughened to produce an even surface finish. Fused silica and M26 borosil samples are exposed to argon plasma for 12 hours, producing eroded surfaces. Mechanical stresses of between 6 MPa and 25 MPa are applied to experiment samples. Before and after exposure, samples are imaged with an Olympus LEXT 3D confocal microscope to produce pre and post-exposure images. A contact profilometer provides detailed statistics derived from line-scans taken on the pre and post-exposure surfaces. Cell patterns are observed to develop on the fused silica samples. The evolution of the M26 samples shows the protrusion of low-yield boron nitride grains from the silica matrix, and the development of a roughness pattern that is independent of initial surface statistics. For both materials, no dependence of the development of the surfaces on the applied mechanical stress has been observed.

The fifth contribution of this work, given in Chapter 8, is the development of two models that explain the observed development of surfaces for each material in the stressed erosion experiment. A distinctive cell pattern develops on the post-exposure fused silica surfaces. A one-dimensional model successfully reproduces the development of the cell pattern using the angle-dependence of the sputtering yield of fused silica. Qualitative and quantitative features of the cell pattern are reproduced with the model.

The patterns observed to develop on the M26 borosil samples are explained in terms of the heterogeneous erosion model described in Chapter 3. The evolution of fused silica is explained by the angle-dependence of the sputtering yield of the material. The evolution of M26 is explained in terms of the difference in sputtering yield between the BN grains and silica matrix within the composite material.

9.2 Suggestions for Future Work.

Because theoretical problems with the energy scale of mechanical strain energy in a material are present in the SRH, and because no dependence of the plasma erosion of materials on the presence of mechanical stress has been found, another explanation will have to be found for the development of the anomalous erosion ridges. Some suggested avenues for future research are given below.

It is possible that the structure of the anomalous erosion ridges may form due to being grown from microstructural features over large erosion depths, at shallow ion incidence angles to the wall surface. Studying the growth of surface features at shallow ion incidence angles could provide insight into the sort of structures that develop towards the exit plane of a HET. In the 3D raytracing modeling of the erosion of borosil materials, the cases with shallow incidence angles with the wall developed very long "streak-mark" features, which have been observed in certain sections of the highly eroded P-5 thruster. It is expected that shallow incidence angles will produce long length scale features from protruding grains or small surface protrusions. It is also possible that these features may join or grow into larger length scales over very large erosion depths (mm or more).

Another possibility is that the structure of the anomalous erosion ridges reflects a periodic structure in the plasma itself: In the ion impact energy (which the sputtering rate depends on super-linearly above a sputtering threshold energy), or the ion number density (which the sputtering rate depends on linearly). If this is the case, then observing the azimuthal variation in electron temperature, ion density, and ion energy in a heavily eroded HET that has developed the erosion ridges may reveal variations that are self-consistent with the presence of the ridges. Alternatively, if a channel wall is created with ridges pre-machined into the wall, and plasma electron temperature, ion energy, and ion density variations are observed to adjust (relative to a smooth walled HET) in a way that would tend to amplify these features, then this would suggest an instability that could explain the ridges.

Evidence that the magnetic field may be producing an effect on the formation of the anomalous ridges is given in Mazouffre *et. al*. [20]. In this paper it is reported that the anomalous erosion ridge phenomenon exhibits a slight tilt in the direction opposite the electron drift direction, or parallel to the ion flow which is slightly twisted by the magnetic field. In addition, the length scale of the anomalous ridges is on the order of the electron Larmor radius, which is a function of the magnetic field strength [20] [17]. One potential future test is to operate HETs, or other devices producing a magnetized discharge, under conditions with greater or lesser magnetic field strengths and gyro-radii, and observe the beginnings of erosion patterns on the channel with CMM.

Research conducted by Langendorf [61] in section 10.5.4 of his dissertation on plasma sheaths suggests another potential mechanism to describe the formation of the erosion ridges. The plasma sheaths surrounding samples with grooves on the same order

or larger than the plasma Debye length have an increase in sheath potential drop over the grooves which would tend to increase ion impact energy in grooves. This mechanism may provide the basis for an instability that would grow surface features, governed by surface curvature, and the Debye length.

APPENDIX A

E-mails granting permission to reprint Figure 1.3, Figure 1.4, and Figure 1.5:

Hi Aaron,

Yes, you may use the image of the PPS®1350. In return, I would love to get a copy of your dissertation when it is available.

I have found it frustrating that the so-called “anomalous erosion” has received comparatively so little attention over the past years, when it reality it is a true life limiter. Apart from the discussion by Pr Morozov, there isn’t much in the literature, at least that I know of, and the observations that can be made at different thruster scales or different operating conditions fuel even more questions about the detailed mechanisms behind this erosion process.

Otherwise the short answer as to measurements of the depth of the short-scale erosion pattern is unfortunately no – we were not successful at the time to obtain usable profilometer measurements at this scale and on this kind of roughness. We only measured the large-scale (average) erosion profile. However I can tell you that after 10,540 hrs there are sometimes really deep pits or crevasses, sometimes drilling all the way through the remaining ceramic material.

Best regards,

Olivier.

Olivier Duchemin, Ph.D.
Senior Electric Propulsion Engineer
PPS®5000 Project Manager

Snecma, SAFRAN Group
Space Propulsion Division
Forêt de Vernon - BP 802
27208 Vernon, France
Tel. +33 (0)2 32 21 76 19
Fax +33 (0)2 32 21 75 05

Dear Aaron,

Thank you for your inquiry. AIAA grants permission for you to reprint Figure 17 from the article described below, in your dissertation. Appropriate credit must be given in the figure caption (e.g., “From [paper title and authors]; reprinted by permission of the American Institute of Aeronautics and Astronautics, Inc.”). Note that the original source should be cited in full in the reference list.
For future reference, you may find the information on our Rights and Permissions page helpful. Most permission requests are easily processed through Copyright Clearance Center:
http://www.aiaa.org/rightsandpermissions/
If you have any further questions, please let me know.

Sincerely,

Heather A. Brennan
Director, Publications
American Institute of Aeronautics and Astronautics www.aiaa.org
12700 Sunrise Valley Drive, Suite 200
Reston, VA 20191-5807
800-639-AIAA (2422)
heatherb@aiaa.org 703.264.7568 (direct)

Aaron,

I received approval to send you the original photograph. Please do not include any size references (but I appreciate your gumption).

Best regards,

Mr. Welander J
Benjamin Welander
Electric Propulsion Systems
Aerojet Rocketdyne
Desk: 425.936.6787
welander@rocket.com

REFERENCES

[1] R. Jahn, Physics of Electric Propulsion, New York: McGraw-Hill, 1968.

[2] M. Dudeck, F. Doveil, N. Arcis and S. Zurbach, "Plasma Propulsion for Geostationary Satellites and Interplanetary Spacecraft," *Romanian Journal of Physics*, vol. 56, pp. 3-14, Jan 2011.

[3] C. Clauss, M. Day, V. Kim, Y. Kondakov and T. Randolph, "Preliminary study of possibility to ensure large enough lifetime of SPT operating under increased powers," in *33rd Joint Propulsion Conference and Exhibit*, Seattle, WA, 1997.

[4] K. H. De Grys, A. Mathers, B. Welander and V. Khayms, "Demonstration of 10,400 Hours of Operation on 4.5 kW Qualification Model Hall Thruster," in *46th AIAA/ASME/SAE/ASEE Joint Propulsion Conference & Exhibit*, Nashville, TN, 2010.

[5] R. R. Hofer, I. G. Mikellides, I. Katz and D. M. Goebel, "Wall sheath and electron mobility modeling in hybrid-PIC Hall thruster simulations," *AIAA Paper*, vol. 5267, p. 2007, 2007.

[6] C. Garner, J. Brophy, J. Polk and L. Pless, "A 5,730-hr cyclic endurance test of the SPT-100," in *31st Joint Propulsion Conference and Exhibit*, San Diego, CA, 1995.

[7] S. Zurbach, O. B. Duchemin, V. Vial, F. Marchandise, N. Cornu and N. Arcis, "Qualification of the PPS-1350 Hall Thruster at 2.5 kW," in *49th AIAA/ASME/SAE/ASEE Joint Propulsion Conference*, San Jose, CA, 2013.

[8] S. Langendorf and M. L. R. Walker, "Effects of Wall Temperature and Surface Roughness on the Plasma Sheath," in *50th AIAA/ASME/SAE/ASEE Joint Propulsion Conference*, Cleveland, OH, 2014.

[9] R. R. Hofer, I. G. Mikellides, I. Katz and D. M. Goebel, "BPT-4000 Hall thruster discharge chamber erosion model comparison with qualification life test data," in *30th International Electric Propulsion Conference*, Florence Italy, 2007.

[10] S. Y.-M. Cheng, "Modeling of Hall thruster lifetime and erosion mechanisms," 2007.

[11] J. T. Yim, Computational modeling of Hall thruster channel wall erosion, ProQuest, 2008.

[12] P. Peterson, D. Manzella and D. Jacobson, "Investigation of the Erosion Characteristics of a Laboratory Hall Thruster," in *39th AIAA/ASME/SAE/ASEE Joint Propulsion Conference and Exhibit*, Huntsville, AL, 2003.

[13] *Boron Nitride Downloadable Datasheets*, Precision Ceramics.

[14] M. Gamero-Castano and I. Katz, "Estimation of Hall thruster erosion using HPHall," Princeton University, 2005.

[15] Y. Garnier, V. Viel, J. F. Roussel, D. Pagnon, L. Mange and M. Touzeau, "Investigation of xenon ion sputtering of one ceramic material used in SPT discharge chamber," in *26th International Electric Propulsion Conference*, Kitakyushu, Japan, 1999.

[16] Y. Garnier, V. Viel, J. F. Roussel and J. Bernard, "Low-Energy Xenon Ion Sputtering of Ceramics Investigated for Stationary Plasma Thrusters," *Journal of Vacuum Science and Technology,* vol. 17, no. 6, pp. 3246-3254, 1999.

[17] A. I. Morozov, "The conceptual development of stationary plasma thrusters," *Plasma Physics Reports,* vol. 29, no. 3, pp. 235-250, 2003.

[18] S. Mazouffre, P. Echegut and M. Dudeck, "A calibrated infrared imaging study on the steady state thermal behaviour of Hall effect thrusters," *Plasma Sources Science and Technology,* vol. 16, no. 1, p. 13, 2007.

[19] C. Marrese, J. Polk, L. King, C. Garner and A. Gallimore, "Analysis of Anode Layer Thruster Guard Ring Erosion," in *Proceedings of the 1995 International Electric Propulsion Conference,* Columbus, OH, 1995.

[20] S. Mazouffre, "Plasma Induced Erosion Phenomena in a Hall Thruster," in *Recent Advances in Space Technologies, 2003,* Istanbul, Turkey, 2003.

[21] V. V. Zhurin, H. R. Kaufman and R. S. Robinson, "Physics of closed drift thrusters," *Plasma Sources Science and Technology,* vol. 8, no. 1, p. R1, 1999.

[22] V. Gavryshin, V. Kim, V. Kozlov and N. Maslennikov, "Physical and Technical Bases of the Modern SPT Development," in *Proceedings of the 1995 International Electric Propulsion Conference,* Cleveland, OH, 1995.

[23] K. de Grys, N. Meckel, G. Callis, D. Greisen, A. Hoskins, D. King, F. Wilson, L. Werthman and V. Khayms, "Development and Testing of a 4500 Watt Flight Type

Hall Thruster and Cathode," in *Proceedings of the 27th International Electric Propulsion Conference*, Pasadena, CA, 2001.

[24] H. E. Wilhelm, "Quantum Statistical Analysis of Surface Sputtering," *Journal of Spacecraft and Rockets*, vol. 13, no. 2, pp. 116-118, 1976.

[25] H. E. Wilhelm, "Quantum-statistical analysis of low energy sputtering," *Australian Journal of Physics*, vol. 38, no. 2, pp. 125-134, 1985.

[26] L. Zhang and Z. L. Zhang, "Anisotropic energy distribution of sputtered atoms induced by low energy heavy ion bombardment," *Radiation Effects and Defects in Solids*, vol. 160, no. 8, pp. 337-347, 2005.

[27] Z. L. Zhang and L. Zhang, "Anisotropic angular distribution of sputtered atoms," *Radiation Effects and Defects in Solids*, vol. 159, no. 5, pp. 301-307, 2004.

[28] J. Bohdansky, "A universal relation for the sputtering yield of monatomic solids at normal ion incidence," *Nuclear Instruments and Methods in Physics Research Section B: Beam Interactions with Materials and Atoms*, vol. 2, no. 1, pp. 587-591, 1984.

[29] I. G. Mikellides, R. R. Hofer, I. Katz and D. M. Goebel, "The Effectiveness of Magnetic Shielding in High-Isp Hall Thrusters," in *49th AIAA/ASME/SAE/ASEE Joint Propulsion Conference*, San Jose, CA, 2013.

[30] A. M. Schinder, M. L. Walker and J. Rimoli, "3D Model for Atomic Sputtering of Heterogeneous Ceramic Compounds," in *49th AIAA/ASME/SAE/ASEE Joint Propulsion Conference*, San Jose, CA, 2013.

[31] A. J. Satonik and J. L. Rovey, "Modification of Boron Nitride Ceramic to Replicate Hall Effect Thruster Surface Wear," in *50th Aerospace Sciences Meeting*, Nashville, TN, 2012.

[32] J. M. Haas, "Low-perturbation interrogation of the internal and near-field plasma structure of a Hall thruster using a high-speed probe positioning system," 2001.

[33] F. S. Gulczinski III, "Examination of the structure and evolution of ion energy properties of a 5 kw class laboratory Hall effect thruster at various operational conditions," University of Michigan, 1999.

[34] T. B. Smith, "Deconvolution of ion velocity distributions from laser-induced fluorescence spectra of xenon electrostatic thruster plumes," NASA Glenn Research Center, 2003.

[35] A. P. Yalin, B. Rubin, S. R. Domingue, Z. Glueckert and J. D. Williams, "Differential Sputter Yields of Boron Nitride, Quartz, and Kapton Due to Low Energy Xe+ Bombardment," *AIAA Paper*, Vols. 5314-2007, 2007.

[36] J. F. Ziegler, *SRIM, Stopping Range of Ions in Matter Software Package*, 2008.

[37] D. G. Zidar and J. L. Rovey, "Hall-Effect Thruster Channel Surface Properties Investigation," *Journal of Propulsion and Power*, vol. 28, no. 2, pp. 334-343, Mar 2012.

[38] D. M. Goebel and I. Katz, Fundamentals of Electric Propulsion: Ion and Hall Thrusters, vol. 1, Wiley. com, 2008.

[39] G. D. Hobbs and J. A. Wesson, "Heat flow through a Langmuir sheath in the presence of electron emission," *Plasma Physics*, vol. 9, no. 1, p. 85, 1967.

[40] S. Mazouffre, J. P. Luna, D. Gawron, M. Dudeck and P. Echegut, "An infrared thermography study on the thermal load experienced by a high power Hall thruster," in *29th International Electric Propulsion Conference*, Princeton, NJ, 2005.

[41] R. A. Martinez, H. Dao and M. L. R. Walker, "Power Deposition into the Discharge Channel of a Hall Effect Thruster," *Journal of Propulsion and Power*, vol. 30, no. 1, pp. 209-220, 2013.

[42] W. C. Michels and S. Wilford, "The physical properties of titanium. i. emissivity and resistivity of the commercial metal," *Journal of Applied Physics*, vol. 20, no. 12, pp. 1223-1226, 1949.

[43] J. H. Cairns, "Apparatus for investigating total hemispherical emissivity," *Journal of Scientific Instruments*, vol. 37, no. 3, p. 84, 1960.

[44] I. Katz, I. G. Mikellides and R. Hofer, "Channel Wall Plasma Thermal Loads in Hall Thrusters with Magnetic Shielding," in *47th AIAA/ASME/SAE/ASEE Joint Propulsion Conference & Exhibit*, San Diego, CA, 2011.

[45] *COMBAT Boron Nitride Solids Product Datasheet*, St. Gobain Ceramic Materials, 2011.

[46] *Boron Nitride Downloadable Datasheets*, Precision Ceramics.

[47] K.-S. Kim, J. A. Hurtado and H. Tan, "Evolution of a surface-roughness spectrum caused by stress in nanometer-scale chemical etching," *Physical Review Letters,* vol. 83, no. 19, pp. 3872-3875, 1999.

[48] S. M. Wiederhorn, "Fracture surface energy of glass," *Journal of the American Ceramic Society,* vol. 52, no. 2, pp. 99-105, 1969.

[49] R. W. Trice and J. W. Halloran, "Influence of microstructure and temperature on the interfacial fracture energy of silicon nitride/boron nitride fibrous monolithic ceramics," *Journal of the American Ceramic Society,* vol. 82, no. 9, pp. 2502-2508, 1999.

[50] G. Leroy, M. Sana and C. Wilante, "Evaluation of the bond energy terms for the various types of boron-nitrogen bonds," *Theoretica chimica acta,* vol. 85, no. 1-3, pp. 155-166, 1993.

[51] N. Laegreid and G. K. Wehner, "Sputtering yields of metals for Ar+ and Ne+ ions with energies from 50 to 600 eV," *Journal of Applied Physics,* vol. 32, no. 3, pp. 365-369, 1961.

[52] P. Sigmund, "Theory of Sputtering I. Sputtering Yield of Amorphous and Polycrystalline Targets," *Physical Review,* vol. 184, no. 2, pp. 383-416, 1969.

[53] M. L. Walker, R. R. Hofer and A. D. Gallimore, "The effects of nude Faraday probe design and vacuum facility backpressure on the measured ion current density profile of Hall thruster plumes," in *38th AIAA/ASME/SAE/ASEE Joint Propulsion Conference & Exhibit,* Indianapolis, Indiana, 2002.

[54] L. Williams, Ion acceleration mechanisms of helicon thrusters, Georgia Institute of Technology, 2013.

[55] "IONIVAC Transmitter ITR 200 S," Oerlikon Leybold.

[56] D. Rosenberg and G. Wehner, "Sputtering Yields for Low Energy He+-, Kr+-, and Xe+-Ion Bombardment," *Journal of Applied Physics,* vol. 33, no. 5, pp. 1842-1845, 1962.

[57] *Properties of Fused Quartz,* Technical Glass Products.

[58] High-Temperature Characteristics of Stainless Steels, vol. 9004, American Iron and Steel Institute, 1979.

[59] L. Ponson, D. Bonamy, H. Auradou, G. Mourot, S. Morel, E. Bouchaud, C. Guillot and J.-P. Hulin, "Anisotropic self-affine properties of experimental fracture surfaces," *International Journal of Fracture,* vol. 140, no. 1-4, pp. 27-37, 2006.

[60] P. Townsend, J. Kelley and N. Hartley, "Chapter 6: Sputtering," in *Ion implantation, sputtering, and their applications,* Academic Press, 1976, pp. 111 - 147.

[61] S. Langendorf, Effects of Electron Emission on Plasma Sheaths, Georgia Institute of Technology, 2015.

[62] D. G. Zidar and J. L. Rovey, "Boron Nitride Hall-effect Thruster Channel Surface Properties Investigation," in *47th AIAA/ASME/SAE/ASEE Joint Propulsion Conference & Exhibit,* San Diego, CA, 2011.

[63] M. Walker, J. Ready, G. Thompson, J. Rimoli and M. Keidar, "Comprehensive Study of Plasma-Wall Sheath Transport Phenomena Annual Report 2014-2015," AFOSR, 2015.

[64] I. G. Mikellides, I. Katz, R. R. Hofer and D. M. Goebel, "Magnetic shielding of a laboratory Hall thruster. I. Theory and validation," *Journal of Applied Physics*, vol. 115, no. 4, p. 043303, 2014.

[65] A. Kieckhafer and L. B. King, "Energetics of Propellant Options for High-Power Hall Thrusters," *Journal of Propulsion and Power,* vol. 23, no. 1, pp. 21-26, 1 Jan 2007.

[66] I. Katz, I. Mikellides, B. Jorns and L. Ortega, "Hall2De Simulations with an Anomalous Transport Model Based on the Electron Cyclotron Drift Instability," in *34th International Electric Propulsion Conference and 6th Nano-satellite Symposium*, Hyogo-Kobe, Japan, 2015.

[67] R. R. Hofer, I. G. Mikellides, I. Katz and D. M. Goebel, "BPT-4000 Hall thruster discharge chamber erosion model comparison with qualification life test data," in *30th International Electric Propulsion Conference*, Florence Italy, 2007.

[68] J. M. Haas, "Low-perturbation interrogation of the internal and near-field plasma structure of a Hall thruster using a high-speed probe positioning system," University of Michigan, 2001.

[69] Y. Garnier, V. Viel, J.-F. Roussel and J. Bernard, "Low-energy xenon ion sputtering of ceramics investigated for stationary plasma thrusters," *Journal of Vacuum Science and Technology*, vol. 17, no. 6, pp. 3246-3254, 1999.

[70] Y. Garnier, V. Viel, J. F. Roussel, D. Pagnon, L. Mange and M. Touzeau, "Investigation of xenon ion sputtering of one ceramic material used in SPT discharge chamber," in *26th International Electric Propulsion Conference*, Kitakyushu, Japan, 1999.

[71] M. Gamero-Castano and I. Katz, "Estimation of Hall thruster erosion using HPHall," in *29th International Electric Propulsion Conference*, Princeton University, 2005.

[72] F. Chen, An introduction to plasma physics and controlled fusion, 2 ed., vol. 1, Springer Science and Business Media LLC, 2006.

[73] M. Britton, D. Waters, R. Messer, E. Sechkar and B. Banks, Sputtering erosion measurement on boron nitride as a Hall thruster material, National Aeronautics and Space Administration, Glenn Research Center, 2002.

[74] A. M. Schinder, J. J. Rimoli and M. L. R. Walker, "Investigation of Plasma Material Erosion under Mechanical Stress," *AIAA Journal of Propulsion and Power*, (Accepted).

[75] D. Kim and D. Economou, "Plasma Molding Over Surface Topography: Simulation of Ion Flow, and Energy and Angular Distributions Over Steps in RF High-Density Plasmas," *IEEE Transactions on Plasma Science*, vol. 30, no. 5, pp. 2048-2058, Oct 2002.

VITA

AARON M. SCHINDER

Aaron Schinder was born in Athens, OH. He received a BS in astronautical engineering with a minor in economics from Purdue University in West Lafayette, IN in Dec 2006. He then served from 2007 through 2011 in the United States Air Force. Aaron worked as a laser effects research engineer for Air Force Research Lab at Kirtland AFB, Albuquerque, NM. Aaron then returned to school at Georgia Tech to pursue a doctorate in aerospace engineering. He earned a MS in aerospace engineering in 2013.